

ABSTRACT

Title of dissertation: MODEL-BASED ANALYSIS OF ATOMIC LAYER DEPOSITION GROWTH KINETICS AND MULTISCALE PROCESS DYNAMICS

Curtisha D. Travis, Doctor of Philosophy, 2014

Dissertation directed by: Professor Raymond A. Adomaitis
Department of Chemical and Biomolecular
Engineering

A first principles model describing the reaction kinetics and surface species dynamics for the trimethylaluminum (TMA) and water half-reactions of alumina atomic layer deposition (ALD) is coupled with a dynamic film growth model and reactor-scale species transport model. The reaction kinetics model is based on reported enthalpies and transition state structures from published quantum-chemical computational studies; these data are used to determine kinetic parameters using statistical thermodynamics and absolute reaction rate theory. Several TMA half-reactions were modeled to account for TMA adsorption and subsequent reaction on a range of growth surfaces spanning bare to fully hydroxylated states. Several water reactions were also considered. By coupling the reaction rate models with surface species conservation equations, a dynamic model is created which is useful for examining the relative rates of competing surface reactions. To describe the continuous cyclic operation of the deposition reaction system, a numerical procedure to discretize limit-cycle solutions is developed and used to distinguish saturating

growth per cycle from non-saturating conditions. The transition between the two regimes is studied as a function of precursor partial pressure, exposure times, and temperature. Finally, a cross-flow tubular ALD reactor system model is derived with components describing the precursor thermophysical properties, precursor delivery system, reactor-scale gas-phase dynamics, and surface reaction kinetics derived from absolute reaction rate theory. These model components are integrated to simulate the complete multiscale ALD process. Limit-cycle solutions defining continuous cyclic ALD reactor operation are computed with a fixed point algorithm based on temporal and spatial discretization within the reactor, resulting in an unambiguous definition of film growth per cycle. The use of the simulator for assisting in process design decisions and optimization frameworks is presented.

MODEL-BASED ANALYSIS OF ATOMIC LAYER DEPOSITION
GROWTH KINETICS AND MULTISCALE PROCESS
DYNAMICS

by

Curtisha D. Travis

Dissertation submitted to the Faculty of the Graduate School of the
University of Maryland, College Park in partial fulfillment
of the requirements for the degree of
Doctor of Philosophy
2014

Advisory Committee:

Professor Raymond A. Adomaitis, Chair
Doctor Maria K. Burka
Professor Panagiotis Dimitrakopoulos
Professor Sheryl E. Ehrman
Professor Oden Rabin
Professor Michael R. Zachariah

© Copyright by
Curtisha D. Travis
2014

DEDICATIONS

I dedicate this thesis to my adoring mother and to my dearest angel, Granny.

Your love has sustained me more than you will ever know.

ACKNOWLEDGMENTS

Wow! Where do I start?! I'll attempt to get through this without getting overly mushy and drown my laptop in tears, but this has been quite the journey for me. Before I continue, allow me to clarify what I mean by the word "journey." Yes, I am in a way referring to the typical "Woe is me! I'm a grad student... and I do research... and sometimes I like it... but sometimes I don't... blah blah blah..." I think you can assume that much. So I'll leave that stuff out.

When I say "journey," I'm not just referring to the last 5 years of my life. I'm referring to... well, my life. Those who truly know me know that I've come such a very long way to get here; and I certainly didn't do it alone. There have been some very instrumental people in my life who have helped me in some way, whether big or small, and while I'm sure my words won't come even close to describing how much I appreciate all of you, please know that I am deeply grateful.

First and foremost, I have to thank God. Through Him, I know, without a doubt, that all things are possible. This experience has strengthened my faith on so many levels, and I am forever grateful that my Heavenly Father has been here to hold my hand every step of the way. As I said, this journey started many years ago, perhaps even back in 80's when I was blessed with a beautiful and wonderfully loving mommy to be here every step of the way, too!

Mama, there are so many things that I can say about you and the selfless support that you have given me throughout all the years of my life. I am truly blessed to have you in my corner! When I say that you are my biggest inspiration,

I really mean it. I don't know where I'd be without you. I would have never gotten this far without the sacrifices you made for me, without your undying love, without your confidence in me, and without your motivation. No matter what I was going through, you gave me perspective; and talking to you somehow always made things better. No one has been here for me the way you have, right by my side every single step of the way; and so I dedicate this to you. You are the reason for so many of the successes I've achieved in my life, and I truly love, adore, and appreciate you!

I am also so very thankful for my Granny and her unwavering support. While she is no longer here, I always remember our conversations and the great confidence she had in me. Granny always believed in me, always advocated for me, and always encouraged me to "Go all the way!" Although she wasn't physically here these last years, those simple words were enough to give me that little extra push when I needed it. So, here we are, Granny—all the way! I hope I have made you proud.

To my Grandma, thank you for also believing in me and encouraging me. While I didn't always have time to respond, all of the random emails with the cute little inspirational messages helped to brighten my days, just knowing that you were thinking of me and praying for me. When I've expressed aggravation with being in school for seemingly all my life or explained how annoyed I was that I couldn't do all the fun things I want to do, you always found a way to make me feel better about it. You always told me not to worry about where things are headed, but just to find joy in each part of the journey as I experience it. So, that's what I did, and it certainly made me a much happier graduate student. Thanks for your love and your advice.

I've been so lucky to have a wonderfully huge family of supporters! I won't be able to name all of you here, but just know that I appreciate each and every one of you. Thank you for always trusting in me. Even when I had my doubts, your support never wavered, never failed. You don't know how much that meant to me. To my aunties Ann, Peg, Berd, Leah, Mae, Sivi, and Netta, my uncles Willie, Alfred, Rance, Jerry, and Perry, and all of my cousins (I would name you all, but that would take forever!), I love you all to pieces!

Through the years, I've also developed one heck of an extended family. Part of the reason why I wanted to attend graduate school in the Washington, DC area is because of the great support network that I have here; and a huge part of that is P.R.I.V.Y., my phenomenal line sisters. I am forever grateful for being joined with such a dynamic group of ladies. You all have been my family away from home. Thank you for the random nights out, the dinners, the girl talk sessions, and just for being a staple in my life. You all have been such a huge support to me during this time, even when you didn't know it. Sometimes I needed to talk and sometimes I just needed a silly, giggly, fun time. Whatever it was, you were there. You've motivated me, you've encouraged me, and you will always inspire me. I love you all!

Another hugely important factor in the happiness and success of one's graduate school experience (perhaps the absolute biggest factor of all) is the advisor. Trust me, I've heard so many horror stories from people about experiences with their advisors. It can get really, really bad. But, thankfully I haven't had any of those experiences. I always say I feel like I really lucked up. Cheers to you, Ray! Thank you for being such a great partner; I couldn't have asked for anyone better! I've

learned so much from you during this time, and I'm so thankful for all of your guidance and support. You've been patient with me as I've learned to shift my thinking from chemistry to chemical engineering, and I really like the way we were able to mesh our two thought processes. You've been immensely helpful, supportive, positive, and you've been a superb example of what a professional chemical engineer should be. I hope that someday I can be as brilliant an engineer as you.

To my college advisor, Dr. Hosten, thank you for being such a great resource for me while at Howard and even now. You encouraged me to do the NRL internship, and that's when I was first introduced to chemical engineering research. You took an interest in my success a very long time ago, and I'm so very glad that we have developed the relationship we have today. You've always been an honest and unbiased person, and you made me feel comfortable to share my ideas with you, always knowing that you'd try your best to steer me in the right direction. Your professional advice has been immensely helpful, and I am forever grateful.

I can't go without acknowledging financial support from my "Uncle Bill" or more formally, the Bill and Melinda Gates Foundation. Some 11 years ago, a committee of individuals decided that I'd make a worthy recipient of the Gates Millennium Scholarship, and they've been committed to my academic success ever since. Your support has definitely been instrumental throughout this process, and I know just how privileged I am to have received it. Thank you, thank you, and thank you!

Lastly, to those I may have inadvertently left out, please accept my sincerest apology. Charge it to my head and not my heart. Thank you all, and let the next journey begin!

TABLE OF CONTENTS

List of Tables	x
List of Figures	xiii
1 Introduction	1
1.1 The ALD Cycle	3
1.2 Principles of ALD	5
1.2.1 Self-limiting Growth	6
1.2.2 Growth Rate Limitations	7
1.3 Motivation	9
1.4 Review of ALD Kinetics Modeling	10
1.4.1 Empirical Methods	12
1.4.1.1 Reactor-scale Models	13
1.4.2 First Principles Methods	15
1.5 Selection of a Kinetics Model	16
1.5.1 Modeling Objectives	17
1.6 Outline of Dissertation	19
2 Surface Reaction Mechanisms and Kinetics	23
2.1 General Mechanism of Oxide ALD	24
2.2 Review of Oxide ALD Processes	27
2.3 Transition State Theory	30
2.3.1 Statistical Mechanics	32
2.3.2 Molecular Chemisorption	35
2.3.3 Ligand Exchange	36
2.3.4 Precursor Dissociation	37
2.3.5 Hydrogen Association	38
2.3.6 Densification	39
2.4 Concluding Remarks	40
3 Alumina Case Study	41
3.1 Modeling Objective	45
3.1.1 Formulation of Underlying Model Assumptions	46
3.2 Chemical Reaction Mechanism	47
3.2.1 The Surface State	48
3.2.2 Surface State Dynamics	52
3.3 Surface Reaction Equilibria and Reaction Rates	53

3.4	Computation of Species Partition Functions	57
3.4.1	Half-cycle A	59
3.4.1.1	R ₁	59
3.4.1.2	R ₂	60
3.4.2	Half-cycle B	61
3.4.2.1	R ₆ and R ₉	61
3.4.2.2	R ₇ and R ₁₀	62
3.5	Representative Surface Coverages and Reaction Rates	63
3.6	Limit-cycle Solutions	65
3.6.1	A Collocation Procedure	66
3.7	<i>GPC</i> and Film Composition for Self-limiting Growth	69
3.7.1	<i>GPC</i> and <i>gpc</i>	69
3.8	A map of <i>gpc</i> (δ_A, δ_B)	70
3.8.1	Comparison to Measured Exposures	72
3.8.2	Effect of Deposition Temperature	74
3.9	Concluding Remarks	76
4	Kinetic Mechanism Analysis	78
4.1	Surface Reaction Mechanism	80
4.1.1	TMA Reactions on Hydroxylated Alumina	95
4.1.2	TMA Reactions on Bare Alumina	96
4.1.3	Water Reactions on Methylated Alumina	97
4.1.4	Water Reactions on Bare Alumina	98
4.1.5	Gas-phase Side Reactions	99
4.2	Analysis of Reaction Mechanism	100
4.2.1	Comparative Analysis of TMA Kinetics	101
4.2.1.1	Resolution of Thermodynamics	103
4.2.2	Comparative Analysis of Water Kinetics	105
4.2.2.1	Resolution of Thermodynamics	107
4.2.3	Gas-phase Side Reaction Mechanism Analysis	108
4.3	Thermodynamic Sensitivity	109
4.4	Growth Surface State Dynamics	110
4.4.1	Dynamic Simulation Results	112
4.4.2	Growth per cycle	115
4.5	Concluding Remarks	118
5	Dynamic ALD Reactor Design	121
5.1	ALD Reactor Designs	122
5.1.1	Precursor Delivery	123
5.1.2	Reaction Chamber	125
5.1.2.1	Batch Reactors	126
5.2	A Continuous Cross-flow ALD Reactor	126
5.2.1	Process Recipe	130
5.3	Precursor Characteristics	131
5.4	Precursor Delivery System Model	134

5.4.1	Universal Gas Sizing Flow Equation for Control Valves	137
5.4.2	Development of a Continuous Flow Equation	139
5.5	Reactor Model	145
5.6	Limit-Cycle Computations	147
5.6.1	Time Discretization for Forced-periodic Systems	148
5.6.2	Newton-Raphson Procedure	150
5.7	Representative Results	151
5.7.1	TMA Ballast Chamber Dynamics	152
5.7.2	Reactor-scale Dynamics	153
5.7.3	Growth Surface Dynamics	154
5.8	Mapping the <i>gpc</i> Behavior	155
5.8.1	The V_{bc} - τ_B Plane	157
5.9	Concluding Remarks	159
6	Distributed Reactor Model	162
6.1	Continuous Cross-flow ALD Reactor Model	163
6.1.1	Formulation of Underlying Model Assumptions	164
6.1.2	Model Description	167
6.1.3	Chemical Species Conservation	169
6.1.3.1	Boundary Conditions	170
6.1.4	ALD Film Growth	171
6.2	Discretization Procedure	172
6.3	Representative Limit-Cycle Results	173
6.4	Concluding Remarks	178
7	Concluding Remarks	180
7.1	Suggestions for Future Work	182
7.1.1	Surface Reaction Mechanism and Kinetics	183
7.1.2	Reactor-scale Model Optimization	183
7.1.3	Reactor Model	184
7.1.4	Extension to Additional ALD Chemistries	184
A	Throughput Optimization	185
	Bibliography	187
	Publications & Presentations	203

LIST OF TABLES

2.1	<i>Elementary reactions for the ALD of $MO_{x/2}$ by metal precursor ML_x and H_2O as in reaction (2.1). Surface species are denoted with double bars (\parallel) and $y \in [1, x]$. Gas-phase reactions are non-ideal in ALD and are thus excluded. Based on a similar table in [36].</i>	26
3.1	<i>A subset of elementary surface reactions taking place during TMA exposure as identified in [156]. $Me = CH_3$. d and m subscripts denote DMA and MMA surface species.</i>	49
3.2	<i>A subset of elementary surface reactions taking place during water exposure as identified in [156]. $Me = CH_3$. d and m subscripts denote DMA and MMA surface species.</i>	50
3.3	<i>Surface reaction model parameters.</i>	52
3.4	<i>Reaction rate energetics data.</i>	54
3.5	<i>Statistical mechanical formulation of equilibrium constants and rate expressions for elementary surface reactions taking place during TMA exposure as identified in [156]. $Me = CH_3$. d and m subscripts denote DMA and MMA surface species.</i>	55
3.6	<i>Statistical mechanical formulation of equilibrium constants and rate expressions for elementary surface reactions taking place during water exposure as identified in [156]. $Me = CH_3$. d and m subscripts denote DMA and MMA surface species.</i>	56
3.7	<i>Molecular partition function contributions for a nonlinear polyatomic ideal gas. DOF, degrees of freedom. n, number of atoms in the molecule. ZPE, zero point energy.</i>	58
4.1	<i>A subset of elementary surface reactions taking place during TMA exposure, beginning with molecular adsorption. $Me = CH_3$.</i>	83
4.2	<i>continued from Table 4.1. A subset of elementary surface reactions taking place during TMA exposure, beginning with molecular adsorption. $Me = CH_3$.</i>	84
4.3	<i>A subset of elementary surface reactions taking place during TMA exposure, beginning with dissociative adsorption as described in [40]. $Me = CH_3$.</i>	84
4.4	<i>A subset of elementary surface reactions taking place during water exposure, beginning with molecular adsorption. $Me = CH_3$.</i>	85
4.5	<i>A subset of elementary surface reactions taking place during water exposure as described in [23]. $Me = CH_3$.</i>	86

4.6	<i>A subset of elementary surface reactions taking place during water exposure, beginning with dissociative adsorption as posed in [60, 61]. Me = CH₃.</i>	86
4.7	<i>A set of elementary gas-phase reactions taking place when both TMA and water are present [111]. Me = CH₃.</i>	87
4.8	<i>Reaction rate energetics. Plot estimate values noted with an asterisk (*). In the instance of multiple values for a parameter, the value used in the dynamic growth model is noted with a dagger (†). Alumina homodeposition studies are noted with a plus sign (+), otherwise all other studies correspond to alumina heterodeposition onto Si-OH substrates.</i>	88
4.9	<i>(continued from Table 4.8) Reaction rate energetics. Plot estimate values noted with an asterisk (*). In the instance of multiple values for a parameter, the value used in the dynamic growth model is noted with a dagger (†). Alumina homodeposition studies are noted with a plus sign (+), otherwise all other studies correspond to alumina heterodeposition onto Si-OH substrates.</i>	89
4.10	<i>Partition function ratios and underlying assumptions. Parenthetical terms in the ΔZ columns designate degrees of freedom assumed to be lost due to the forward reaction. Terms in the ΔZ columns which are not in parentheses designate degrees of freedom assumed to be gained.</i>	90
4.11	<i>(continued from Table 4.10) Partition function ratios and underlying assumptions. Parenthetical terms in the ΔZ columns designate degrees of freedom assumed to be lost due to the forward reaction. Terms in the ΔZ columns which are not in parentheses designate degrees of freedom assumed to be gained.</i>	91
4.12	<i>(continued from Table 4.11) Partition function ratios and underlying assumptions. Parenthetical terms in the ΔZ columns designate degrees of freedom assumed to be lost due to the forward reaction. Terms in the ΔZ columns which are not in parentheses designate degrees of freedom assumed to be gained.</i>	92
4.13	<i>(continued from Table 4.12) Partition function ratios and underlying assumptions. Parenthetical terms in the ΔZ columns designate degrees of freedom assumed to be lost due to the forward reaction. Terms in the ΔZ columns which are not in parentheses designate degrees of freedom assumed to be gained.</i>	93
4.14	<i>(continued from Table 4.13) Partition function ratios and underlying assumptions. Parenthetical terms in the ΔZ columns designate degrees of freedom assumed to be lost due to the forward reaction. Terms in the ΔZ columns which are not in parentheses designate degrees of freedom assumed to be gained.</i>	94
5.1	<i>Reactor dimensions and primary system component design parameters of the ALD reactor system shown in Fig. 5.1. TMA, trimethylaluminum.</i>	128

5.2	<i>Nominal ALD reactor conditions. d-TMA, dimer of TMA.</i>	133
5.3	<i>Parameters for precursor delivery model. Valve flow equations yield flow rates in units of mol/s with pressure in bar and temperature in K.</i>	139
5.4	<i>Selection of data for comparison of water molar flow rate predictions (mol/s) from randomized pressure differentials. Eqns. (5.13) and (5.14) are standard flow equations based on ANSI/ISA guidelines [9]. Eqns. (5.16) and (5.18) are asymptotic and linear approximations, respectively, to the standard equations.</i>	141

LIST OF FIGURES

1.1	<i>Number of ALD publications per year from between 1981 and 2013. Search made with Google Scholar search terms “atomic layer deposition” and “atomic layer epitaxy” [49].</i>	2
1.2	<i>Schematic illustration of one ALD reaction cycle.</i>	4
1.3	<i>Self-limiting ALD and non-ideal growth rate behavior with possible factors causing the observed non-ideality. (left) Growth per cycle as a function of growth temperature. (right) Growth per cycle as a function of precursor exposure time. Reproduced from [140].</i>	6
1.4	<i>Elements of a complete ALD reactor system mathematical model. Chapters 2-4 of this thesis will specifically address the surface reaction kinetics and growth surface state dynamics model components. Chapters 5 and 6 will introduce model components describing the precursor source thermodynamics, precursor delivery system dynamics, and reactor-scale transport dynamics. Chapters 5 and 6 will also incorporate the model components of Chapters 2-4 to make up the complete multiscale ALD model.</i>	20
2.1	<i>An idealized view of the $MO_{x/2}$ ALD process cycle with metal precursor \dot{M} and oxygen precursor \dot{O}.</i>	25
2.2	<i>Schematic reaction path profiles for generic elementary ALD reaction steps. Gas-phase and surface species are noted with Latin and Greek alphabet, respectively. a) Adsorption/ligand-exchange reaction. b) Association reaction.</i>	35
3.1	<i>A snapshot of a 35 nm^2 portion of the ALD growth surface corresponding to $\theta_O = 0.6$ and $\theta_{Me} = 0.5$.</i>	51
3.2	<i>Predictions of the maximum adduct and transition state species surface coverages for $T = 500 \text{ K}$ and a range of precursor partial pressures.</i>	63
3.3	<i>Predictions of the reaction rates for $T = 500 \text{ K}$ and a range of precursor partial pressures. Gas-phase precursor wall collision frequencies, w_A and w_B, are shown for reference.</i>	64
3.4	<i>Surface CH_3 and OH limit-cycle coverage dynamics for $P_A = P_B = 1 \text{ Torr}$ and $T = 500 \text{ K}$. The red and blue curves denote surface Me and OH group coverage, respectively. Dots indicate collocation point locations.</i>	67
3.5	<i>Surface CH_3 and OH limit-cycle coverage dynamics for $P_A = P_B = 1 \text{ Torr}$ and $T = 500 \text{ K}$. The red and blue curves denote the TMA and water doses, respectively. Dots indicate collocation point locations.</i>	68

3.6	<i>A map of gpc as a function of precursor exposure level for $P_A = P_B = 1$ Torr. The point marked $\boxed{2}$ corresponds to $\delta_A = \delta_B = 5 \times 10^5$ and to the conditions of Figs. 3.4 and 3.5.</i>	71
3.7	<i>Effect of temperature on gpc for $P_A = P_B = 1$ Torr. Blue curve corresponds to $\delta_A = \delta_B = 2 \times 10^5$ L, green to $\delta_A = \delta_B = 5 \times 10^5$ L, and red to $\delta_A = \delta_B = 9 \times 10^5$ L. Dashed curve segments indicate the temperature range where TMA decomposes [129].</i>	74
4.1	<i>Representative reaction rates of irreversible TMA half-cycle reactions corresponding to pressure-dependent reactions at $T = 450$ K and maximum surface concentration values for $[X]$, $[X']$, $[O]$, $[S]$, $[Me_1]$, and $[Me_2]$. For reference, the TMA wall collision rate w_A also is shown. Data labels denote the source of energetic information used in the rate computation; e.g. EG04 corresponds to ElliottGreer2004 (first author, last author, and year of publication).</i>	102
4.2	<i>Representative reaction rates of irreversible TMA half-cycle reactions corresponding to pressure-independent reactions at $T = 450$ K and maximum surface concentration values for $[X]$, $[X']$, $[O]$, $[S]$, $[Me_1]$, and $[Me_2]$. Data labels denote the source of energetic information used in the rate computation; e.g. EG04 corresponds to ElliottGreer2004 (first author, last author, and year of publication).</i>	103
4.3	<i>Representative reaction rates of irreversible water half-cycle reactions corresponding to pressure-dependent reactions at $T = 450$ K and maximum surface concentration values for $[X]$, $[X']$, $[O]$, $[S]$, $[Me_1]$, and $[Me_2]$. For reference, the water wall collision rate w_B also is shown. Data labels denote the source of energetic information used in the rate computation; e.g. WM02 corresponds to WidjajaMusgrave2002 (first author, last author, and year of publication).</i>	106
4.4	<i>Representative reaction rate of the gas-phase side reaction. (top) Rate computed with one precursor at constant partial pressure of 0.01 Torr. (bottom) Rate computed with one precursor at constant partial pressure of 0.001 Torr. All rates correspond to reactions at $T = 450$ K. For reference, the gas-phase TMA-water collision frequency z_{AB} also is shown.</i>	109
4.5	<i>Surface species dynamics for $\theta'_X(0) = 1$ (top), $\theta'_X(0) = 0.75$ (middle), and $\theta'_X(0) = 0$ (bottom) at $T=450$ K and $P = 2$ Pa. The initial 0.02 s of the TMA half-cycle have been emphasized to capture the fast surface reactions.</i>	113
4.6	<i>Relative film growth rate contributions of (R_3) and (R_{13}) as a function of initial surface OH group concentration.</i>	116
5.1	<i>Process and instrumentation schematic of the continuous cross-flow ALD reactor.</i>	129
5.2	<i>TMA vapor pressure and degree of dissociation, α, as a function of temperature; data presented in [92] are shown as filled red circles. . .</i>	135

5.3	<i>Water molar flow rate predictions for a randomized set of pressures using the non-choked (NC) and choked (C) flow Eqns. (5.13) and (5.14). The asymptotic approximations (AA) of Eqn. (5.16) and linear approximations (LA) of Eqn. (5.18) for the same random set of pressures are overlaid, illustrating the approximation boundaries with respect to the standard flow rate formulations.</i>	143
5.4	<i>Water molar flow rate predictions for a randomized set of pressures using the non-choked (NC) and choked (C) flow Eqns. (5.13) and (5.14). The asymptotic approximations (AA) of Eqn. (5.16) and linear approximations (LA) of Eqn. (5.18) for the same random set of pressures are overlaid, illustrating the approximation boundaries with respect to the standard flow rate formulations. Non-choked and choked flow regions are shaded blue and red, respectively.</i>	144
5.5	<i>Representative reactor limit-cycle solution with $gpc = 0.806 \text{ \AA}/\text{cycle}$. Reactor nominal conditions consist of $\tau_A = 0.1 \text{ s}$, $\tau_{AP} = \tau_{BP} = 4 \text{ s}$, $\tau_B = 0.1 \text{ s}$ and $V_{bc}/V = 0.02\%$.</i>	152
5.6	<i>Growth per cycle (gpc) as a function of τ_B (left) and V_{bc}/V (right).</i>	156
5.7	<i>Growth per cycle (gpc) as a function of τ_B and V_{bc}/V. The black curves correspond to moles of TMA/cycle supplied to the reactor.</i>	158
6.1	<i>Central time and central space finite differences mesh and solution points.</i>	173
6.2	<i>Representative gas-phase dynamics for $T=450\text{K}$, and $\tau_A = 0.5 \text{ sec}$, $\tau_B = 0.1 \text{ sec}$, and $\tau_{AP} = \tau_{BP} = 2 \text{ sec}$. Curves show spatial reactor position, with inlet marked by -x- and outlet by -o-. In order from top to bottom, the ALD cycle step for each plot is as follows: pulse A, purge A, pulse B, purge B.</i>	174
6.3	<i>Representative gas-phase and surface dynamics for $T=450\text{K}$, and $\tau_A = 0.5 \text{ sec}$, $\tau_B = 0.1 \text{ sec}$, and $\tau_{AP} = \tau_{BP} = 2 \text{ sec}$. Curves show spatial reactor position, with inlet marked by -x- and outlet by -o-.</i>	175
6.4	<i>Exposure and growth per cycle predictions as a function of spatial position in the ALD reactor.</i>	177
A.1	<i>Preliminary results for alumina ALD throughput as a function of precursor exposure times.</i>	186

1

Introduction

Atomic layer deposition (ALD), formerly known as atomic layer epitaxy (ALE), is a thin film manufacturing process based on continuous cycling of an alternating sequence of self-terminating heterogeneous chemical reactions. Under ideal growth, ALD has the capability to produce highly conformal ultrathin films on a variety of materials and complex substrate geometries all while allowing for precise control of film thickness and composition down to a fraction of a monolayer [44].

It is indisputable the tremendous impact that the semiconductor industry has had on ALD interest and the direction of research. ALD was developed nearly 40 years ago by T. Suntola [151], but it wasn't until the last decade that it gained significant research interest. The seemingly sudden growth in ALD literature coincides directly with the end of the classical Moore's Law scaling era [73, 77] which happened around the turn of the 21st century. Dielectrics and metal electrodes for dynamic random-access memory (DRAM) capacitors are now routinely produced via ALD [50]. With 3D tri-gate transistors requiring conformal coatings over complex geometry and metal circuitry pushing scaling limits, ALD emerges as an indispens-

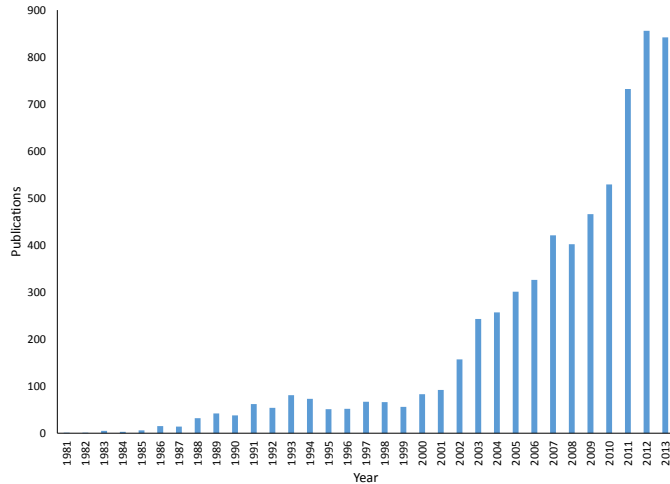


Figure 1.1: *Number of ALD publications per year from between 1981 and 2013. Search made with Google Scholar search terms “atomic layer deposition” and “atomic layer epitaxy” [49].*

able manufacturing tool. Indeed, Intel announced in 2007 that ALD is involved in “the biggest change to computer chips in 40 years” [15].

ALD has received particular attention in depositing high-permittivity (high- κ or “high- k ”) dielectrics, with recent interest in nanostructures, allowing for very controlled modification of nanopores by fine-tuning the deposition parameters [3, 32, 34]. These nanoporous materials have various industrial applications such as catalysts, sensors, membranes, filters, nanotemplates, capacitors, and transistors. Metal oxides such as alumina (Al_2O_3), zirconia (ZrO_2), and hafnia (HfO_2) have thus been the subject of considerable investigation.

Although the ALD industry is not yet fully matured, it has already been applied to sizable material and deposition tool industries as well as huge semiconductor chip fabrication lines. In modern logic chips, thicknesses of 2-3 nm are often desired, meaning that variations in thickness of merely 0.2-0.3 nm already corresponds to

10 % of the total film thickness [73]. A technique which can controllably deposit one monolayer of material would be an optimal method for these applications. Hence with the accelerating advancement of micro- and nanotechnology, ALD continues to emerge as an ideal candidate for producing ultrathin and conformal films across different industries with applications in photovoltaics [160], energy devices [78,101,106], nanofabrication [81], biological systems [149], and the environment [101].

These new thin-film application areas and the ability to deposit an increasing range of new materials have rekindled interest in thin film deposition process modeling as current development activities have pushed traditional fabrication technologies to their limits, further encouraging the use of new deposition techniques such as ALD. In integrated circuit manufacturing, the simultaneously decreasing feature sizes, increasing aspect ratios, complicated designs, and adaptation of new materials call for new methods that enable highly controlled deposition of very thin and conformal films, requirements perfectly matched with ALD [140].

1.1 The ALD Cycle

An ALD cycle typically involves a controlled sequence of self-limiting reaction steps and purge steps as schematically illustrated in Fig. 1.2. While more steps can be incorporated, for instance in the deposition of hafnium aluminates [113], the ALD cycle generally comprises four separate and sequential steps involving two gaseous precursor species introduced in an alternating fashion. The four steps of the ALD cycle can be described as follows:

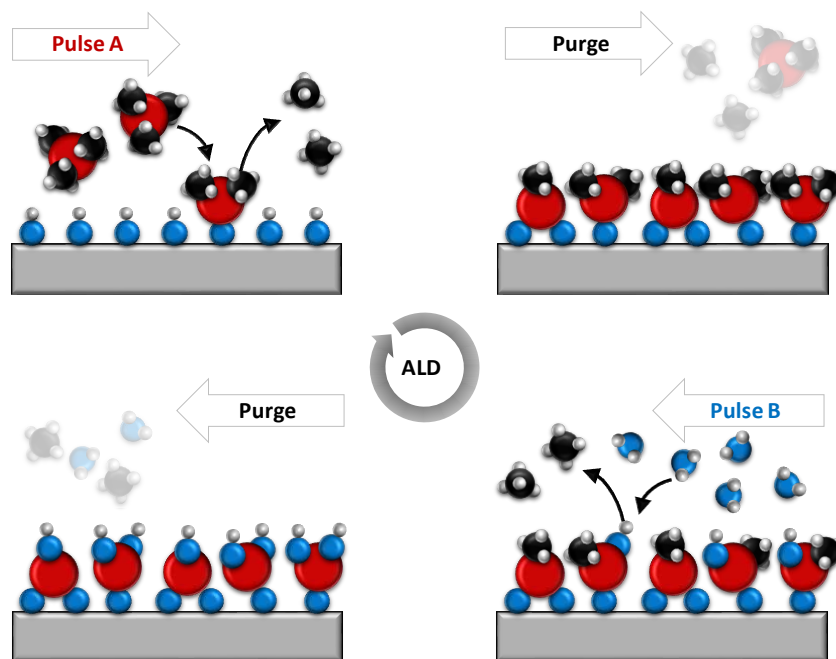


Figure 1.2: *Schematic illustration of one ALD reaction cycle.*

- (i) Pulse A. The first reactant (precursor A) is introduced and proceeds to react with surface species until self-terminating.
- (ii) Purge. Gas-phase by-products and unreacted precursor gas are removed.
- (iii) Pulse B. The second reactant (precursor B) is introduced and proceeds to react in an analogous fashion with the surface species until self-terminating.
- (iv) Purge. Gas-phase by-products and unreacted precursor gas are removed.

Each pulsing step is often referred to as a “half-cycle” or “half-reaction” in the process. Constituting one complete ALD cycle, these four steps are repeated potentially hundreds or thousands of times until the desired film thickness is achieved. Thus the term “growth per cycle” (*gpc*) corresponds to the growth observed for the above sequence of steps. Note that the lower-case abbreviation *gpc* will be used to denote

undersaturating growth and the capitalized *GPC* will be used to denote saturating growth rates observed during self-limiting growth.

1.2 Principles of ALD

ALD and the more widely understood chemical vapor deposition (CVD) systems share a number of common characteristics: they are inherently nonlinear and time-dependent, and model elements describing the deposition surface reaction and gas-phase precursor transport are strongly coupled. In particular, the transport/reaction models must describe phenomena over multiple time and length scales. Because of this phenomenological overlap, some modeling concepts and computational tools developed by the CVD community can be directly put to use in the analysis of ALD systems. However, ALD processes are typically run in a lower temperature regime when compared to CVD, making it a more desirable method for the low thermal budget [73].

Another important distinction can be made between the two deposition processes: the notion of the steady-state deposition rate in CVD does not exist for ALD. The rate of ALD depends strongly on the instantaneous state of the growth surface and this state changes continuously through each pulse and purge interval. The completely dynamic nature of the ALD process adds considerably to the difficulty of developing simulators because the entire process cycle must be modeled and careful chemical and mathematical analysis is required to resolve the multiple time scales present in this process and to identify the rate-limiting steps.

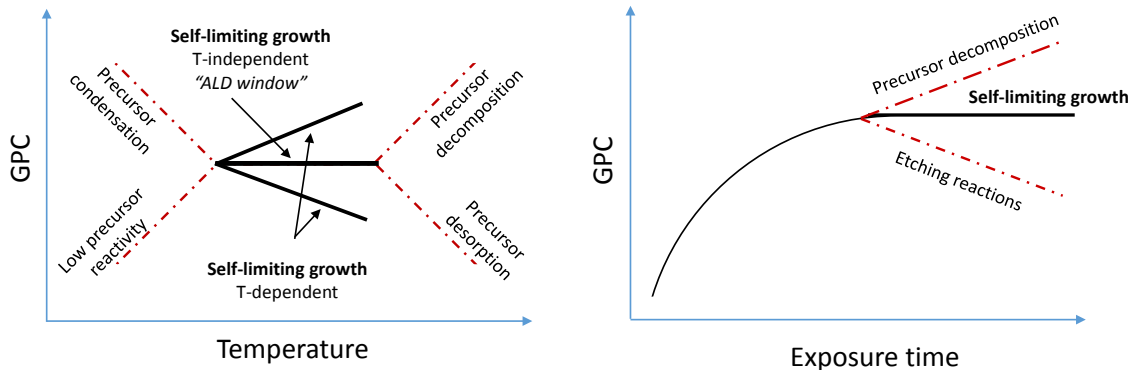


Figure 1.3: *Self-limiting ALD and non-ideal growth rate behavior with possible factors causing the observed non-ideality. (left) Growth per cycle as a function of growth temperature. (right) Growth per cycle as a function of precursor exposure time. Reproduced from [140].*

1.2.1 Self-limiting Growth

What also distinguishes ALD from CVD and other deposition methods is the self-limiting nature of the precursor chemisorption during each exposure period, giving rise to an operation region where the GPC (saturating growth per cycle) is insensitive to perturbations in precursor partial pressure and exposure time. For some ALD systems (*i.e.* different materials to be deposited), an “ALD window” is observed where self-limiting growth also is insensitive to deposition temperature. The net result is highly conformal surface coverage and atomic-level control of film thickness, with equipment-independent GPC for fixed precursor chemistry [44, 131].

The classic picture of self-limiting growth consists of a plot of GPC versus temperature, where the ideal ALD region is bounded at one end by high-temperature precursor decomposition reactions or loss of surface species, and at the other by a non-saturating dose resulting from incomplete surface reactions or precursor condensation [140]. Likewise, plotting GPC versus total precursor exposure (roughly

defined as the product of precursor pressure and exposure time) reveals a constant *GPC* for sufficiently high exposures with a lower bound defined by under-saturating conditions. While certainly desired, the notion of an ALD-window is not a requirement for self-limiting ALD growth and indeed many recently studied processes for oxide films exhibit self-limiting growth which does not conform to an ALD window [119].

1.2.2 Growth Rate Limitations

Perhaps one of the most significant limitations of ALD in high-volume manufacturing is the relatively low growth rate when compared to other processes such as CVD. This can be partially attributed simply to the nature of the process, *i.e.* only a monolayer of growth is to be expected per cycle. But ALD usually produces only a fraction of a monolayer per cycle and this can be attributed to precursor chemistry [140]. This highlights the need to understand reaction mechanisms such that optimal chemical reaction mechanisms can be pursued by manipulating the appropriate process parameters. Note that the low growth rate of ALD processes becomes less of a disadvantage when depositing films of only a few nanometers, as is required in many semiconductor applications [73]. Yet and still, low throughput is widely considered as the main problem of ALD [140].

Throughput is directly related to the ALD growth per cycle and inversely related to the cycle time length. Thus, to optimize the effective growth rate, the *GPC* should be maximized while minimizing the cycle time. However, there are limitations to each approach. Precursor pulsing intervals are limited by chemistry and

cannot be shortened beyond a certain point, or else the surface will not fully saturate and the self-limiting ALD growth regime will not be attained. Purge periods also cannot be arbitrarily shortened due to the necessary isolation of precursor gases in ALD processes. Shortened purge times could result in coexistence of both precursors in the reactor and consequently lead to CVD-like gas-phase reactions. This is non-ideal as the uniformity and film thickness will no longer be controlled. Therefore, careful consideration must be given to understand the process chemistry in order to locate self-limiting growth regions for ideal uniformity and also to optimize the throughput.

In efforts to improve throughput, deviations from ideal ALD growth are occasionally created, *e.g.* operating the ALD process under non-saturating conditions. Often times, total self-limiting surface saturation is limited by kinetics (as opposed to mass transport) and can only be achieved by allowing the surface reactions time to occur. In this instance, increasing the partial pressure of the precursor will not cause a significant increase in growth rate. Further, increasing saturation from 90 % to 100 % may take more time than reaching the first 90 %. It may thus be beneficial to accept the 90 % saturation because then the exposure time can be substantially shortened and the subsequent purge will likewise be shortened due to a lower volume of precursor in the reaction chamber [140]. Use of this limited optimized reactions ALD (LORA) approach has yielded a reported ten-fold increase in throughput [145], although it may cause additional non-uniformity issues depending on the reactor design, *e.g.* it may not be applicable for cross-flow reactors.

1.3 Motivation

With all of this, the need for physically-based dynamic ALD models has never been greater. Consider, for example, the explosion of growth in developing high-throughput spatial ALD systems, now under development for roll-to-roll and other large-substrate applications. The processing speed objectives of these systems can only be fully achieved by model-based process and design optimization methods. While throughput is the primary objective, the level of precursor utilization also plays a significant role in the process operating costs. An important tool for maximizing tool productivity and precursor conversion are ALD deposition kinetics models that are equipment-independent.

Consider, also, the manufacturing environment where minimization of the individual doses of each precursor is necessary to optimize the operation of commercial, multiwafer reactor systems [52]. Precursor dose minimization becomes even more critical in high-throughput spatial ALD systems. The intense interest in this technology can be gauged by the recent ALD 2011 and 2012 conferences where at least six independent designs were presented at each meeting [5, 6]. Maximum substrate throughput in all of these designs is dictated by a lower bound of the self-limiting growth region. Model-based analysis of the self-limiting growth boundary also is motivated by the need to elucidate the chemical reaction mechanisms that result in unusually slow saturation rates in some ALD systems [42]. Understanding the kinetics of the deposition process is critical to distinguishing between competing surface reactions [23] and determining which constitute the self-limiting reaction steps.

Considering all of these known process interactions from atomic-scale chemistry to reactor-scale throughput, study of the ALD process intrinsically necessitates a multiscale problem formulation. Consider, for instance, the intrinsic time scales of the ALD process. While precursor pulsing and purge times scale on the order of seconds to tens of seconds, surface reaction rates which ultimately determine film growth rates scale from fast (ps-ns) to slow (μ s-ms). Moreover film growth scales at Å or nm while reactor sizes are on orders of meters [38]. While it is impossible to describe explicitly all of these length and time scales in a single multiscale simulation, effort should be made to couple these time and length scales in such a way to resolve ALD process interactions across the multiscale domain.

1.4 Review of ALD Kinetics Modeling

Simulation tools are important for understanding the multiscale reaction phenomena at work in ALD processes and for the design, optimization, and control of deposition reactors to reach desired film property specifications [36]. A range of ALD models has been developed at various levels of detail and theory to accommodate specific modeling objectives. Of these, atomic-scale models have produced insightful results by employing *ab initio* methods, such as density functional theory (DFT), to investigate energetically-favored reaction mechanisms, proton transfer pathways, structures of intermediate reaction species, and reaction energetics corresponding to elementary reactions along each stage of ALD growth. Results of such studies have been combined with kinetic Monte Carlo (kMC) simulations to quantify

nucleation [28] and growth [27, 104] kinetics.

Empirical growth models have also been developed to describe ALD kinetics during the initial stages of nucleation [4, 172] and island growth [112, 136, 137]. Additionally, surface reaction models have been developed to predict growth kinetics and the effects of operating parameters (*e.g.*, temperature, pressure, precursor exposure time) during undersaturating conditions and leading to self-limiting ALD growth [96–98, 121, 156].

With increased interest in nanostructured materials (*e.g.* for energy and environmental applications [11]), ALD has emerged as the method of choice for producing conformal coatings in nanoporous structures [33], employed for instance for construction of multilayer nanocapacitors [12], fine-tuning surface properties of nanopores to capture DNA [19], control of pore wall size and composition of catalytic membranes [123], and fabrication of spatially-controlled coatings within nanopores for multi-step catalysis [34]. Because of these and other promising nanoscale ALD applications [81, 101], researchers have developed models for transport and reaction in high-aspect-ratio structures.

There are two general methodologies currently used for predicting ALD reaction kinetics: empirical methods and *ab initio* methods. These two methods utilize vastly different levels of detail in regard to the underlying ALD chemistry and consequently provide varying levels of detail in resolution to the intrinsic kinetic mechanism. Both approaches are reviewed in the subsections to following.

1.4.1 *Empirical Methods*

Because much of the ALD reaction mechanism relies either directly or indirectly on heterogeneous surface processes, it is overwhelmingly common to describe the kinetics in terms of Langmuir adsorption in the form of a reactive sticking coefficient $s(\theta) = s_o(1 - \theta)$ where θ denotes surface coverage of adsorbed species and the initial sticking probability for zero coverage s_o is treated as an adjustable parameter [150]. In these approaches, the detailed surface chemistry is often “lumped” into this parameter, which can be estimated, fitted to computed energetics, or derived from film growth experiments.

In the context of ALD, the reactive sticking coefficient is loosely defined as the probability that a precursor molecule will react upon colliding with the surface and contribute to film growth [85], combining in one parameter the total growth probability as a result of all surface reaction steps. For this reason, some authors also refer to the reactive sticking coefficient as the ALD “reaction probability,” *i.e.* the reactivity of a single precursor molecule with a reactive site on the surface.

Such a kinetics modeling approach is exemplified in [25] which expands on the classic model of ALD step coverage [51] to develop a Langmuir-type surface coverage model relating surface dynamics to precursor impingement fluxes computed using the kinetic theory of gases with an adjustable sticking coefficient. Variations of this reaction kinetics method have been applied to simple array [85], differential equation-based [3, 46–48, 93, 150, 169] and Monte Carlo [32, 84] descriptions of temporal surface coverage evolution.

1.4.1.1 *Reactor-scale Models*

A number of detailed ALD reactor simulations have been reported in the literature, generally comprised of transport equations coupled with a surface reaction model to describe the evolution of the growth surface. The elementary surface reaction kinetics model has also been successfully employed in many of these simulations, beginning perhaps two decades ago with a convection-diffusion transport model coupled to a general surface dynamics model in a flow-type reactor [1]. Precursor concentration profiles and surface coverage were found to be strongly dependent on the chosen sticking coefficient. This work was thereafter extended to investigate temperature effects [147] and ALD growth rates for TiO_2 films, again yielding coverage and growth predictions with strong dependence on the reactive sticking coefficient [148].

Another early transport/reaction coupling is seen in a plug-flow reactor model where the sticking coefficient is assumed to combine condensation and activation energy effects to yield estimates of film growth rate and uniformity [171]. More recently, a simple plug-flow model, based largely on empirical sticking and recombination probabilities, was developed to study film conformality as a function of aspect ratio, but the details of the mathematical model were omitted [85].

Following interest in feature-scale investigations, a dynamic reactor model for Al_2O_3 ALD processing combined precursor flow modeling through the reactor and a ballistic flux model for precursor transport and reaction in substrate trenches, attributing the reactive sticking coefficient to quantum-chemical simulations of surface

reactions, although the connection between the two was not made clear [125]. A similar model was later developed for a multi-wafer batch reactor where the sticking coefficient for the HfO_2 process was deduced from experiments in a single-wafer reactor [86].

In more recent work, a transport/reaction model for a tubular ALD reactor was developed [170] where the reactive sticking coefficient is based on an earlier Monte Carlo simulation in high-aspect-ratio nanopores [32]. The Monte Carlo simulation therein utilizes ALD surface reaction rates assumed proportional to a reactive sticking coefficient based on an empirically-determined, first-order reaction rate coefficient from [26]. The Monte Carlo simulation work in [84] gives an excellent overview of this modeling approach, listing a range of sticking coefficients for high-aspect-ratio systems.

As an empirical alternative to the reactive sticking coefficient, a rigorous dynamic parameter estimation problem was formulated to resolve Arrhenius rate expressions based on *ex situ* film thickness measurements for ZnO ALD as part of a fluid dynamics model [68–72]. Characteristic of the ALD reaction mechanism, high correlations were found between Arrhenius parameter estimations for the reactions considered. Improvement in precision of individual parameter estimates was achieved after reparameterization of the Arrhenius equation to effectively decrease these correlations.

1.4.2 *First Principles Methods*

An accurate and arguably more flexible alternative to the empirical kinetics approach exists: reaction kinetics formulations for each elementary ALD reaction step based on first principles (FP). First principles (or *ab initio*) methods are distinguished by requiring no empirical fitting parameters, allowing for genuinely novel situations to be investigated. Such methodologies may involve deriving rate constants from quantum-chemical and/or quantum-statistical computations coupled with a theory of reaction rate expressions. While these theories have been long established [41, 45, 88, 89], few results have been reported in direct computation of ALD reaction rates using *ab initio* methods, perhaps due to the perceived costly computation of necessary input parameters [36].

Perhaps the earliest reported formulation of *ab initio* ALD kinetics is seen in a transient plug-flow reactor model developed using the Rice-Ramsperger-Kassel-Marcus (RRKM) theory to derive rate constants for elementary ZrO_2 and HfO_2 reactions [24]. Because of the chemical detail contained in the model, empirical observations of temperature-induced growth rate reduction was able to be explained: an effect of surface dehydroxylation with increased temperature.

Later mechanistic studies which use kinetic parameters derived from transition state theory have been able to predict reaction temperature and pressure dependencies of Al_2O_3 ALD reactions to selectively decorate and passivate the zigzag and armchair edges of graphene nanoribbons [168]. A similar approach was also used in the theoretical study of hafnium aluminates [113]. Through the use of an *ab initio*

kinetics model, enhanced and inhibited chemisorption was found to be due to the dehydroxylation behavior of the chemical precursor species.

Physically-based surface reaction models using statistical mechanics and transition state theory were also developed for Al_2O_3 in [156, 158, 167] and applied to a dynamic reactor-scale model [157], allowing for the analysis of substrate effects, identification of self-saturating growth regions in temperature and pressure, kinetic comparison of growth mechanisms, and discernment of reactor design limits.

1.5 Selection of a Kinetics Model

All things considered, the detailed surface chemistry of ALD reactions is indeed ignored in most feature-scale and multiscale model formulations [38]. Yet interestingly, despite wide use of kinetics models based on the reactive sticking coefficient, there still remains little consistency in reported values and no general agreement as to the effects lumped into this parameter which is typically restricted $s \in [0, 1]$, but may vary by orders of magnitude, even when precursor systems are identical [84]. Moreover, the experimental and computational manner in which it is determined varies, such that absolute values are rarely reported in the literature [142]. Thus, from the existing body of work, one can see that use of the sticking coefficients approach for ALD kinetics modeling remains problematic.

To avoid the ambiguity of empirical modeling approaches, a more consistent reaction kinetics model is desired. Selection of an appropriate model must be made with the understanding that, by essence, a model is an imitation of reality at a given

level of theory and a balance must be found between system size and computational cost, particularly in multiscale systems such as those intrinsically necessitated by ALD processes. Specifically, one must choose appropriate levels of theory for atomic-scale surface reaction dynamics, nano- to micro-scale film growth dynamics, and macro-scale chemical species transport.

Selection of model hierarchy (*e.g.* levels of detail and theory, characteristic sizes, and characteristic times) for a process system should be guided by the pre-determined modeling objectives and application [58]. Because of their proven accuracy, *ab initio* methods (*e.g.* density functional theory) are currently the methods of choice for predicting atomic structures and reaction energetics for ALD processes of today and the future [38]. Thus it naturally follows to consider an *ab initio* method to model reaction kinetics, provided it aligns with the overall modeling objectives.

1.5.1 Modeling Objectives

Because the rate of deposition for ALD processes clearly depends on the saturating coverage, it is appealing to develop an analytical model of surface coverage and film growth. Early transport/reaction studies reveal that growth is not usually limited by precursor transport, but rather by surface reaction kinetics, confirming the importance of ALD chemistry [46–48]. Indeed, surface reactions may remain short of saturation and fall short of self-limiting growth because of slow kinetics [140]. An early kinetic Monte Carlo simulation, likewise, affirms that appropriate ALD model descriptions should involve atomistic concepts and a more detailed formulation of the mechanism in terms of surface coverage and elementary reactions [24].

Thus, a fundamental understanding of the chemistry and kinetics of film growth is of primary interest and importance in order to find the best conditions for obtaining high-quality films. Such knowledge drives ALD process development, through quantitative predictions of growth rate, temperature dependence and pulse/purge durations, and assists in precursor selection and design of processes for new materials. This leads to the first modeling objective:

*First principles understanding of ALD reaction
mechanisms and growth kinetics*

In typical ALD processes, many factors come into play that can lead to incomplete surface saturation and consequently non-ideal film growth. Therefore, determining the set of operating conditions corresponding to self-saturating growth has practical consequences because of the potentially desirable reactor operating conditions found at these limits [140]. A detailed reaction kinetics model should be able capture these effects. Thus, the second modeling objective naturally follows:

*Identification of ALD operating limits
for self-saturating growth*

Many properties of interest in experiment (*e.g.* film growth, conformality, and uniformity) are only accessible in theory via multiscale simulation. A multiscale model that successfully combines chemical species transport with *ab initio* derived reaction kinetics yields insights that would simplify the design of new precursors and the optimization of ALD processes. First principles results have turned out to be most powerful when they can add atomic-scale explanation to experimental data,

predict outcomes, and contribute to innovations in ALD processing [36, 38]. This leads to the third and final modeling objective:

Explanation and prediction of multiscale

ALD reaction phenomena

Returning to the model selection criteria suggested at the beginning of this section, it is now possible to state that a multiscale model consisting of an *ab initio* surface reaction kinetics and film growth model coupled with a distributed reactor-scale model would be appropriate in meeting the above stated objectives. Such a predictive model has the potential to add significantly to the understanding and development of ALD processes.

1.6 Outline of Dissertation

Despite the recent increase in ALD research, there still remains much to be resolved in determining the conditions for the desired self-limiting ALD growth, a condition ultimately dependent on ALD chemistry. Therefore, the motivation of this thesis is to develop a generally applicable modeling procedure that makes use of the adsorption and reaction energetics and transition-state configuration data from *ab initio* studies in computing surface reaction rate coefficients.

Using these rate coefficients in the context of Al₂O₃ ALD, a surface reaction kinetics model will be developed to predict the dynamic changes in surface species concentration as a function of time during each exposure period, introducing the concept of using limit-cycle solutions to examine film growth as a function of process

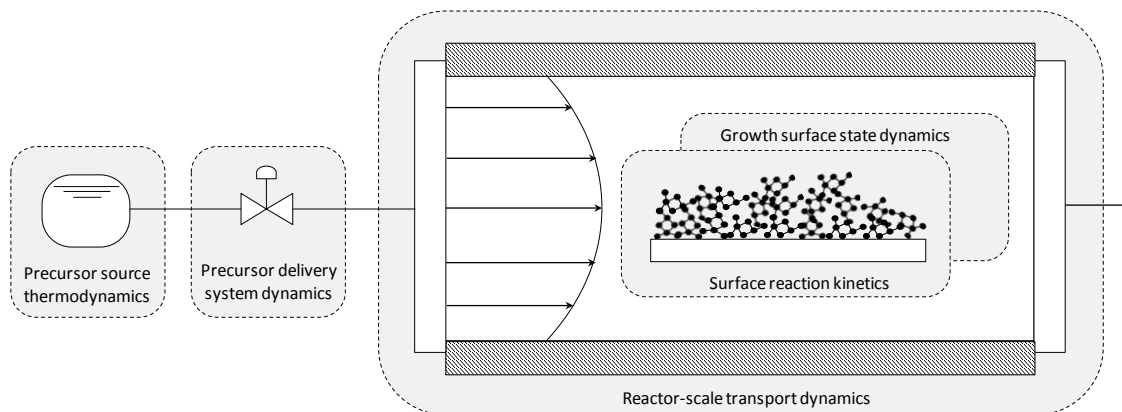


Figure 1.4: *Elements of a complete ALD reactor system mathematical model. Chapters 2-4 of this thesis will specifically address the surface reaction kinetics and growth surface state dynamics model components. Chapters 5 and 6 will introduce model components describing the precursor source thermodynamics, precursor delivery system dynamics, and reactor-scale transport dynamics. Chapters 5 and 6 will also incorporate the model components of Chapters 2-4 to make up the complete multiscale ALD model.*

operating conditions. Finally, this model will be coupled to a dynamic reactor-scale species transport model (Figure 1.4) based on a laboratory-scale reactor system currently under testing. The primary contributions of this thesis are its use of physically-based reaction kinetics models derived from transition state theory [156, 158] and limit-cycle computations describing the steady operation of these reactor systems across the multiscale domain [157].

In Chapter 2, a review of the surface reaction mechanism suggested for oxide ALD processes is given in the context of transition state theory. The majority of ALD kinetics studies are based on empirical parameters and thus are limited in novel ALD chemistries and reactor designs. An alternative surface reaction kinetics methodology is suggested whereby statistical formulations of thermodynamic quantities are used to make *ab initio* rate predictions for ALD processes.

In Chapter 3, principles of the surface kinetics model are applied to the Al_2O_3

ALD system using trimethylaluminum and water precursor gases. Molecular partition functions are derived for chemically reacting species, the rates of each elementary reaction step are computed, and a limit-cycle film growth model is presented for the homodeposition ALD phase. Based on the surface reactions and film growth model, an ALD growth per cycle is predicted for under-saturating conditions leading to the identification of process parameters (namely temperature and exposure level) corresponding to the ideal self-limiting growth regime.

In Chapter 4, the surface reaction kinetics model is further developed to analyze a network of elementary surface reactions which are probable in the context of Al_2O_3 ALD. Representative rates are determined based on the reported energetics of several quantum-chemical computational studies and a kinetic ALD mechanism is proposed. A dynamic growth model is presented, giving insight into the relative contributions of competing ALD surface reactions as well as dissociative adsorption reactions as a function of varying surface hydroxyl group and methyl group concentrations.

In Chapter 5, the surface reaction kinetics model is coupled to a dynamic lumped parameter reactor model for diagnostic design of a laboratory-scale cross-flow ALD reactor. Based on the reactor design, a precursor delivery model is presented to effectively model the precursor dosing sequences throughout the ALD cycle. Again, limit-cycle model computations are employed to investigate the steady operation phase of the ALD process and optimization of film growth rate is assessed in the context of the reactor design.

In Chapter 6, the surface reaction kinetics model is coupled to a distributed

reactor model to investigate the spatial distribution of film growth and provide insight into the effects of the spatially and temporally distributed exposure profile in the tubular reactor. These effects are evaluated in the context of distributed ALD film rate growth predictions and film uniformity.

Chapter 7 provides the conclusion to this thesis.

2

Surface Reaction Mechanisms and Kinetics

The success of ALD ultimately rests on chemistry. As such, ALD process development undeniably depends on a progressive knowledge of the underlying mechanisms of reaction, with the aim to identify elementary chemical reactions that promote ideal film growth as well as those that lead to undesired by-products or impurities [38, 140].

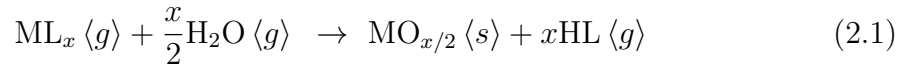
This fundamental knowledge of ALD process chemistry should enable us to answer critical questions about a particular system, namely, *What are the mechanisms responsible for self-saturating surface coverage during a precursor pulse?* and *By what mechanisms are these surface species consumed during the subsequent precursor pulse?* Quantitative answers to these questions can provide vital information to be used for process optimization models and for the design of new ALD processes and reactor systems [38].

To date, much of ALD research has been motivated by the semiconductor processing industry [73]. As such, in terms of subject matter and popularity, ALD

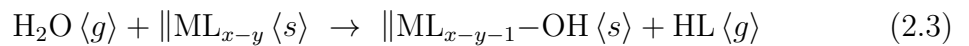
simulations follow the same trend as ALD experiments, with most recent work devoted to the study of depositing oxides and nitrides, particularly high-permittivity (high- κ) dielectrics such as Al_2O_3 , HfO_2 , and ZrO_2 [37]. A predominant topic of published atomic-scale simulations is the study of chemical reaction mechanisms, specifically the elementary reaction steps of the ALD process which lead to film growth.

2.1 General Mechanism of Oxide ALD

The overall reaction to deposit metal oxide film $\text{MO}_{x/2}$ (*e.g.* $\text{M} = \text{Al}, \text{Hf}, \text{Zr}, \text{Ti}$) using water as an oxygen source can be described by its stoichiometrically equivalent CVD reaction



where the number of ligands (*e.g.* $\text{L} = \text{CH}_3, \text{Cl}$) x on metal precursor ML_x determines the molar ratio of the precursor gases and by-product HL [36,136]. In the case of ALD, this reaction is generally separated into two half-reactions corresponding to the sequential precursor pulse periods and may therefore be written as



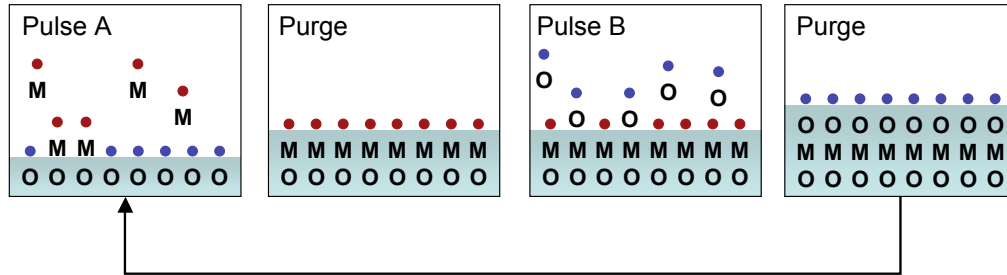


Figure 2.1: *An idealized view of the $MO_{x/2}$ ALD process cycle with metal precursor \dot{M} and oxygen precursor \dot{O} .*

where the double bars (\parallel) are used to denote a surface-bound species and ligands eliminated during the metal adsorption reaction impact the succeeding oxygen adsorption reaction such that $y \in [1, x)$.

A simplified view of this ALD binary reaction sequence is schematically illustrated in Fig. 2.1. Generally, during pulse A, the metal precursor adsorbs onto a hydroxylated substrate, undergoing a ligand-exchange reaction with the surface-bound oxygen species and, thereby, becoming permanently bound to the growth surface. After a sufficient purge period leaving no reactive species in the gas phase, the oxygen precursor is introduced during pulse B. This initiates a subsequent reaction, which proceeds analogously to the reaction in pulse A, whereby the oxygen precursor adsorbs onto the surface, undergoes a ligand-exchange reaction with the surface-bound metal species and, consequently, becomes permanently bound to the film. This step is also followed by a purge [152].

Half-reactions (2.2) and (2.3) may be decomposed into a number of elementary reaction steps: molecular adsorption of the precursor, dissociation of the molecule onto neighboring surface sites, surface diffusion of hydrogen [50] and association into a by-product molecule which subsequently desorbs [36]. These corresponding

Table 2.1: *Elementary reactions for the ALD of $MO_{x/2}$ by metal precursor ML_x and H_2O as in reaction (2.1). Surface species are denoted with double bars (\parallel) and $y \in [1, x]$. Gas-phase reactions are non-ideal in ALD and are thus excluded. Based on a similar table in [36].*

	Molecular desorption	Molecular adsorption
A.	$ML_x + \parallel OH \rightleftharpoons$	$\parallel OH - ML_x$
	$ML_x + \parallel O \rightleftharpoons$	$\parallel O - ML_x$
B.	$H_2O + \parallel ML_y \rightleftharpoons$	$\parallel ML_y - OH_2$
	$H_2O + \parallel M \rightleftharpoons$	$\parallel M - OH_2$
C.	$HL \rightleftharpoons$	$\parallel HL$
	Diffusion of hydrogen and association into molecule	Dissociation of molecule and diffusion of hydrogen
D.	$\parallel O - ML_x + \parallel M \rightleftharpoons$	$\parallel O - ML_{x-1} + \parallel ML$
	$\parallel O - ML_y + \parallel M \rightleftharpoons$	$\parallel O - ML_{y-1} + \parallel ML$
E.	$\parallel M - OH_2 + \parallel O \rightleftharpoons$	$\parallel M - OH + \parallel OH$
	$\parallel OH + \parallel O \rightleftharpoons$	$\parallel O + \parallel OH$
F.	$\parallel OH - ML_{y-1} + \parallel HL \rightleftharpoons$	$\parallel OH_2 + \parallel ML_y$
	$\parallel O - ML_{x-1} + \parallel HL \rightleftharpoons$	$\parallel OH + \parallel ML_x$
	$\parallel O - ML_{y-1} + \parallel HL \rightleftharpoons$	$\parallel OH + \parallel ML_y$
	Porosification	Densification
G.	$\parallel ML_y + \parallel OH \rightleftharpoons$	$\parallel ML_y - OH$
	$\parallel MO_{x/2} \langle surf \rangle \rightleftharpoons$	$\parallel MO_{x/2} \langle bulk \rangle$

elementary steps for reaction (2.1) are summarized in Table 2.1. Based on the results of experimental data and quantum-chemical computations, this complex scheme of chemical reactions leads to the formation of a stoichiometric $MO_{x/2}$ submonolayer.

Adsorption/desorption (reactions A-C) is subject to variability due to dependence on surface coverage and partial pressures which, for precursors, are strategically controlled by pulsing sequences throughout the ALD cycle. These reactions are thus not restricted to a particular ALD period, although ideally precursor partial pressures and pulse/purge lengths would be controlled such that reaction A occurs during the metal precursor pulse which is followed by a sufficiently long purge so

as to completely remove any unreacted precursor, thereby impeding further heterogeneous reactions. Likewise, reaction B would ideally occur during the water pulse which is followed by a sufficiently long purge so as to completely remove any unreacted water. By contrast, dissociation/association (reactions D-F) and densification/porosification (reaction G) are independent of pressure, but instead dependent on surface coverage and kinetics. Therefore, theoretically these reactions are also not restricted to a particular ALD period and may contribute to growth throughout the ALD cycle, subject of course to the availability of necessary surface species.

For most oxides, the individual reaction steps may be classified as either Lewis acid-base (reactions A, B, D, F) by transfer of electrons or Brønsted acid-base (reactions E, F, G) by transfer of hydrogen. These elementary steps may also be grouped into reaction sequences, such as dissociative adsorption ($A_{fwd}+D_{fwd}$) or what is commonly referred to in literature as “ligand exchange” ($A_{fwd}+F_{rev}+C_{rev}$) during metal precursor exposure and similarly dissociative adsorption ($B_{fwd}+E_{fwd}$) or ligand exchange ($B_{fwd}+F_{rev}+C_{rev}$) during water exposure. Indeed, most oxide ALD reaction sequences commonly suggested may be expressed as some combination of these elementary reaction steps [36].

2.2 Review of Oxide ALD Processes

Chemistry is a fundamental key to the success of ALD processes. The unique characteristics of ALD can be achieved and benefited from only when precursors provide self-limiting growth through saturative surface reactions while minimizing

competing non-growth side reactions. Numerous studies have attempted to explain the ALD mechanism using an array of *in situ* and *ex situ* surface characterization techniques (*e.g.* spectroscopy and microscopy methods), but there is yet much to be understood [44]. To examine mechanisms in more detail, many researchers now turn to quantum-chemical computational tools based on DFT [38].

Together, empirical and simulation studies provide evidence that oxide ALD processes generally follow a similar reaction path [37]. Molecular chemisorption of the precursor is the first stage in the chemical reactions. Upon adsorption, a stable Lewis acid-base adduct is formed through a covalent interaction between an empty orbital of the metal atom and a lone pair on the oxygen atom. After adduct formation, the precursor may either desorb or undergo a ligand exchange (also termed “ligand elimination”) reaction, in which case it becomes incorporated into the bulk film. Al_2O_3 [23, 37, 39, 40, 65, 100, 129, 130, 130, 162, 167], HfO_2 [24, 107–109, 164], and ZrO_2 [24, 59, 163, 165] are common examples of ALD systems known to follow this adsorption/reaction path.

One of the earliest mechanisms to be computed with DFT was that of the prototypical Al_2O_3 system grown by $\text{Al}(\text{CH}_3)_3$ and H_2O . Computations yield similar energy profiles for both precursors [162, 167] and dissociative adsorption of $\text{Al}(\text{CH}_3)_3$ onto bridged oxygen sites for low surface hydroxylation [40]. For the various pathways investigated, hydrogen transfer was found to occur most readily from a neighboring hydroxyl group during water half-reactions, increasing the Al–O coordination number and local density of the growing film [23].

Similar DFT study of the HfO_2 mechanism (HfCl_4 and H_2O precursors) yields a

comparable energy profile for molecular adsorption and metal precursor dissociative adsorption onto bridged oxygen sites [164]. In this study, large entropic differences between the reactants and adduct were found to cause high desorption rates which only increased with temperature. Since precursor desorption inhibits film growth, this temperature effect is of obvious importance. It was reasoned that a higher temperature causes loss of surface hydroxyl groups which in turn decreases precursor reactivity on the surface, a finding which has been corroborated [108]. ZrO_2 (ZrCl_4 and H_2O precursors) has been found to follow a nearly identical ALD reaction path with the same competitive desorption effects [59, 163, 165].

Collectively, these studies outline a critical role for ligand exchange in the mechanism of oxide deposition. Because ALD depends on self-limiting reactions in the metal precursor pulse, it can be shown that the growth rate depends linearly on the degree to which ligands are eliminated during this phase [35]. Also important to film growth are densification reactions in which oxygen and hydroxyl groups facilitate incorporation of highly-coordinated metal atoms into the bulk film [116]. Considering that the ALD product is a dense solid film, precursor adsorption and film growth must involve coordination increase of the constituent atoms. While many of the studies cited herein suggest reaction mechanisms consistent with increases in coordination number, the importance of densification as an element of ALD is not yet widely recognized [37].

All things considered, there exists a relatively decent library of thermodynamic data for oxide ALD processes. Several DFT studies have produced estimates of reaction energetics, and indeed much of what is understood about the detailed oxide

reaction mechanism is based on these data. Yet, it is commonly stated that ALD is driven by kinetics, rather than thermodynamics [37]. While one could argue that certain reaction steps are reversible and thermodynamically controlled, the competition between slower side reactions and faster growth reactions is crucial for successful ALD. Kinetic rates determine the competition between reactions and hence the time needed for the surface to become saturated and its chemical makeup. However, far too little attention has been paid to rigorously predicting kinetics for such reactions.

2.3 Transition State Theory

Transition state theory (TST)¹ has been previously applied in only a few ALD studies [24,113,167,168]. It has been applied more recently as a first principles kinetics approach in complete ALD surface reaction models [156,158] and incorporated into a reactor-scale model for deposition of Al₂O₃ films [157]. Latest model developments incorporate the explicit chemical kinetics derived from TST into a distributed transport/reaction model for process optimization and analysis of multiscale process interactions [159].

Recall that the overall ALD reaction of Eqn. (2.1) may be decomposed into a series of elementary reaction steps as outlined in Table 2.1. In each elementary reaction, TST asserts the existence of an activated complex, or transition state, which prevails as an intermediate species along the path from reactants to products.

¹Transition state theory is also referred to as “absolute rate theory,” “absolute reaction rate theory,” “the theory of absolute reaction rates,” and “activated complex theory.”

Formed by the union of two or more reactant molecules, this transition state is assumed to be in equilibrium with the reactants [88,89]; *e.g.* in the generic reaction $A + B \rightarrow P$, the theory states



In order for the products P to be formed, the transition state species $(AB)^\ddagger$ must cross a potential energy barrier; the height of this barrier gives the reaction activation energy. The rate of the forward reaction is thus governed by the concentration of the activated complex and the frequency of its decomposition along the reaction coordinate. While the concentration of the activated complex cannot be readily measured, the chemical equilibrium relationship based on molecular concentration can be stated as

$$K^\ddagger = \frac{\mathcal{C}_{(AB)^\ddagger}}{\mathcal{C}_A \mathcal{C}_B} = V \exp\left(\frac{-\Delta G^\ddagger}{k_B T}\right) \quad (2.5)$$

where the concentrations are expressed in units of molecules per volume for gas-phase species and V is the volume of the gas phase. For surface-bound species, the concentrations would be per unit area and the equilibrium constant for purely surface reactions (*i.e.* not adsorption or desorption) would have units of area per molecule.

As described by TST, the reaction rate v may therefore be stated as

$$v = \nu \mathcal{C}_{(AB)^\ddagger} \quad (2.6)$$

$$= \nu K^\ddagger \mathcal{C}_A \mathcal{C}_B \quad (2.7)$$

$$= \nu \exp\left(\frac{-\Delta G^\ddagger}{k_B T}\right) V \mathcal{C}_A \mathcal{C}_B \quad (2.8)$$

$$= \nu \exp\left(\frac{\Delta S^\ddagger}{k_B}\right) \exp\left(\frac{-\Delta H^\ddagger}{k_B T}\right) V \mathcal{C}_A \mathcal{C}_B \quad (2.9)$$

where $\nu = k_B T/h$ is the standard decomposition frequency, ΔG^\ddagger is the Gibbs free-energy difference between the transition state and reactants, ΔS^\ddagger is the entropy difference, ΔH^\ddagger is the enthalpy difference, k_B is Boltzmann's constant, T is absolute temperature, and h is Planck's constant [45].

2.3.1 *Statistical Mechanics*

The chemical equilibrium constant can also be derived from the interrelationship between statistical and classical thermodynamics in the form of a system partition function $\tilde{\mathcal{Z}}$ which is comprised of molecular partition functions \mathcal{Z} [143]. The molecular partition function gives a measure of how molecules are distributed (partitioned) among energy states. It gives an indication of the average number of states that are accessible at a particular temperature for noninteracting molecules. These molecular partition functions typically include translational, rotational, vibrational, and electronic energy contributions which collectively define the chemical species.

The statistical formulation of Helmholtz free energy for a system of nonin-

teracting molecules $A = -k_B T \ln \tilde{\mathcal{Z}}$ is related to the classical description of Gibbs free energy by $G = A + PV$ where P and V are the system pressure and volume, respectively. For a gas of N independent molecules, PV can be replaced by $Nk_B T$ and thus

$$G = -k_B T \ln \tilde{\mathcal{Z}} + Nk_B T \quad (2.10)$$

where $\tilde{\mathcal{Z}} = \mathcal{Z}^N / N!$ corresponds to the total system partition function (all molecules) and \mathcal{Z} is the molecular partition function for each individual molecule. Substituting this into Eqn. (2.10) and applying Stirling's approximation ($\ln N! = N \ln N - N$),

$$G = -Nk_B T \ln \left(\frac{\mathcal{Z}}{N} \right) \quad (2.11)$$

which of course reduces to $G = -k_B T \ln \mathcal{Z}$ for a single particle. Thus for the TST reaction (2.4),

$$-\frac{\Delta G^\ddagger}{k_B T} = \ln \frac{\mathcal{Z}_{(AB)^\ddagger}}{\mathcal{Z}_A \mathcal{Z}_B} \quad (2.12)$$

Applying this to the rate equation for reaction (2.4) and extracting the zero-point energy contribution from the molecular partition functions, we have

$$v = \frac{k_B T}{h} \frac{z_{(AB)^\ddagger}}{z_A z_B} \exp \left(\frac{-E^\ddagger}{k_B T} \right) \mathcal{C}_A \mathcal{C}_B \quad (2.13)$$

where E^\ddagger is the activation energy for the reaction and z is the molecular partition function per unit volume of the gas undergoing adsorption or per unit area of the adsorption site, *i.e.* $z = \mathcal{Z}/(\text{area or volume})$. Note that the activation energy is the

zero-point vibrational energy difference between the reactants and the transition state.

It is reasonable to assume that $E^\ddagger \cong \Delta H^\ddagger$ [41], and so comparison of Eqn. (2.9) with Eqn. (2.13) implies that the partition function ratio in the rate expression is essentially a quantitative description of the entropy difference between the transition state and reactants [45]. Hence, consideration of the translational, rotational, and vibrational degrees of freedom associated with the atoms of each reactant and intermediate species allows for computation of the molecular partition functions and consequently reaction rate constants from first principles.

In theory, statistical thermodynamics may be used in computation of any reaction rate, provided the availability of reaction energetics and relative molecular structures of the participating species. When the activation energies are also derived from first principles, a complete *ab initio* rate expression emerges. In the context of ALD, rates for a series of heterogeneous (adsorption) and homogeneous (surface) elementary reaction steps must be resolved. Drawing upon the existing body of *ab initio* modeling work for reaction energetics and molecular structures, *ab initio* reaction rate expressions are possible when statistical mechanics are applied with TST principles. This reaction kinetics modeling approach and its implication on the characteristic interdependence of ALD reactions will be demonstrated with a general reaction scheme typical to ALD growth. An adsorption/ligand-exchange reaction scheme is demonstrated in Fig. 2.2a with an association reaction scheme in Fig. 2.2b, both of which result in bulk film production and a gas-phase by-product.

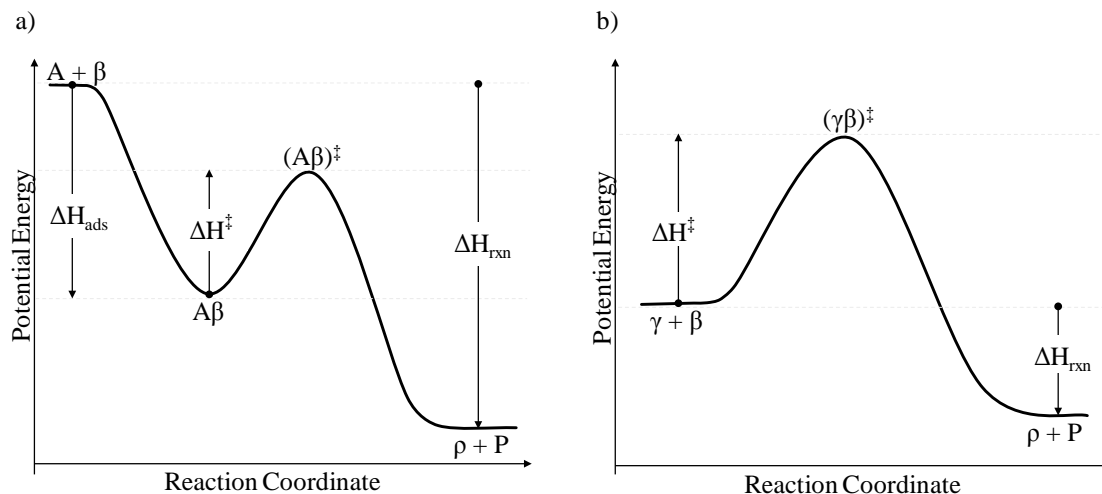
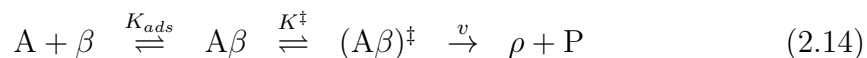


Figure 2.2: Schematic reaction path profiles for generic elementary ALD reaction steps. Gas-phase and surface species are noted with Latin and Greek alphabet, respectively. a) Adsorption/ligand-exchange reaction. b) Association reaction.

2.3.2 Molecular Chemisorption

Table 2.1, A_{fwd} or B_{fwd}

Before application of TST, the adsorption/ligand-exchange ALD reaction of Fig. 2.2a



must be separated into elementary steps where A and β represent a gas-phase precursor and adsorption site, respectively. Consider first the barrierless adsorption of gas-phase species A onto surface site β and formation of stable surface adduct $A\beta$



This equilibrium relationship can be expressed as

$$K_{ads} = \frac{\mathcal{C}_{A\beta}}{\mathcal{C}_A \tilde{\mathcal{C}}_\beta} = \frac{\mathcal{Z}_{A\beta}}{(\mathcal{Z}_A/V) \mathcal{Z}_\beta} \exp\left(\frac{-E_{ads}}{k_B T}\right) \quad (2.16)$$

where V is the gas-phase volume, E_{ads} is the negative adsorption energy [88], and $\tilde{\mathcal{C}}_\beta = \mathcal{C}_\beta - \mathcal{C}_{A\beta}$ is the effective concentration of adsorption sites. Solving for $\mathcal{C}_{A\beta}$ and considering all thermodynamic quantities to be on a per-molecule basis, the Langmuir isotherm is recovered.

$$\mathcal{C}_{A\beta} = \frac{K_{ads} \mathcal{C}_A}{1 + K_{ads} \mathcal{C}_A} \mathcal{C}_\beta = \frac{K_{ads} P_A}{k_B T + K_{ads} P_A} \mathcal{C}_\beta \quad (2.17)$$

2.3.3 Ligand Exchange

Table 2.1, $F_{rev} + C_{rev}$

After adsorption, the surface-bound $A\beta$ species may undergo a forward ligand-exchange reaction



where ρ is a surface product of the bulk film and P is a gas-phase by-product. With E^\ddagger activation energy, the above equilibrium may be expressed as

$$K^\ddagger = \frac{C_{A\beta}^\ddagger}{C_{A\beta}} = \frac{\mathcal{Z}_{(A\beta)^\ddagger}}{\mathcal{Z}_{A\beta}} \exp\left(\frac{-E^\ddagger}{k_B T}\right) \quad (2.19)$$

Following Eqns. (2.16) and (2.19), the forward reaction rate is derived.

$$v = \frac{k_B T}{h} \mathcal{C}_{(A\beta)^\ddagger} \quad (2.20)$$

$$= \frac{k_B T}{h} K^\ddagger \mathcal{C}_{A\beta} \quad (2.21)$$

$$= \frac{k_B T}{h} K^\ddagger \frac{K_{ads} P_A}{k_B T + K_{ads} P_A} \mathcal{C}_\beta \quad (2.22)$$

Substituting in all *ab initio* quantities, the rate of the ligand-exchange reaction is found to be

$$v = \frac{k_B T}{h} \frac{\mathcal{Z}_{(A\beta)^\ddagger}}{(\mathcal{Z}_A/V) \mathcal{Z}_\beta} e^{[-(E_{ads} + E^\ddagger)/k_B T]} \frac{P_A \mathcal{C}_\beta}{k_B T + \frac{\mathcal{Z}_{A\beta}}{(\mathcal{Z}_A/V) \mathcal{Z}_\beta} e^{(-E_{ads}/k_B T)} P_A} \quad (2.23)$$

Unsurprisingly, the final rate expression includes partition functions from the reactants, stable adduct, and transition state. This results from the double equilibrium relationship of Eqn. (2.14). Following this conclusion, additional elementary reaction rates can be derived.

2.3.4 Precursor Dissociation

Table 2.1, D_{fwd} or E_{fwd}

Consider the ALD reaction where surface-bound precursor molecule α loses a ligand to neighboring adsorption site β .



The $(^{-L})$ and $(^{+L})$ superscripts respectively represent the loss and gain of a ligand.

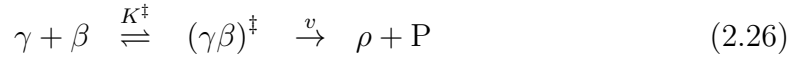
Because the elementary dissociation step is a reversible process, no forward reaction rate is considered. However, the equilibrium relationship is established as

$$K_{dis} = \frac{C_{\alpha-L}C_{\beta+L}}{C_{\alpha}C_{\beta}} = \frac{Z_{\alpha-L}Z_{\beta+L}}{Z_{\alpha}Z_{\beta}} \exp\left(\frac{-E_{dis}}{k_B T}\right) \quad (2.25)$$

2.3.5 Hydrogen Association

Table 2.1, $F_{rev} + C_{rev}$

Consider now the ALD association reaction of Fig. 2.2b



where γ and β both represent available adsorption sites of different kinds. Following similar derivation as shown in previous reactions, the equilibrium constant can be expressed as

$$K^\ddagger = \frac{C_{(\gamma\beta)^\ddagger}}{C_{\gamma}C_{\beta}} = \frac{Z_{(\gamma\beta)^\ddagger}}{(Z_{\gamma}/S)Z_{\beta}} \exp\left(\frac{-E^\ddagger}{k_B T}\right) \quad (2.27)$$

where S is the reactive surface area. The forward reaction rate is thus

$$v = \frac{k_B T}{h} \frac{Z_{(\gamma\beta)^\ddagger}}{(Z_{\gamma}/S)Z_{\beta}} \exp\left(\frac{-E^\ddagger}{k_B T}\right) C_{\gamma}C_{\beta} \quad (2.28)$$

2.3.6 *Densification*

Table 2.1, G_{fwd}

Lastly, densification can be represented by the reaction



where surface species γ and β form a coordinative bond. A similarity may be noted with the previously described association reaction. While the association reaction includes a densification step in formation of the transition state, ultimately two ligands are removed from the surface in the forward reaction. By contrast, a pure densification reaction restructures bonds of the surface and bulk film, but does not yield a by-product. For this reason, it may also be referred to as a “reorganization” reaction.

Densification is important to ALD because it increases the coordination number of each reactant, leading to bulk film growth with equilibrium constant

$$K_{den} = \frac{C_{\gamma\beta}}{C_{\gamma}C_{\beta}} = \frac{Z_{\gamma\beta}}{(Z_{\gamma}/S)Z_{\beta}} \exp\left(\frac{-E_{den}}{k_B T}\right) \quad (2.30)$$

where S is again the reactive surface area.

2.4 Concluding Remarks

A large and growing body of literature has investigated the mechanism of oxide ALD processes, both empirically and theoretically. There is a consensus among researchers that these processes follow a largely similar reaction path which may be decomposed into a series of interdependent elementary reactions. Modeling research to date has tended to focus on computing *ab initio* based thermodynamics for these reaction steps, rather than kinetics. As a result, most growth models poorly predict ALD outcomes except for the use of empirical fitting parameters.

In addition to being highly variable with limited applicability across reactor systems, empirical methods are also limited by their inability to make predictions for novel ALD processes. By contrast, *ab initio* simulations yield more flexibility and also give a more detailed description of reaction chemistry. Indeed, much of the chemical reaction mechanism described herein stems from experimentally-validated *ab initio* simulations. The predictive power of such models has promising implications for the future direction of ALD applications.

An *ab initio* reaction kinetics method was thus suggested through the use of transition state theory and statistical mechanics. This method was applied to several representative elementary reactions, combinations of which are known to describe real oxide ALD processes. In the next chapter, these mechanisms and reaction kinetics formulations will be used to derive equilibrium and rate expressions for the Al_2O_3 deposition system.

3

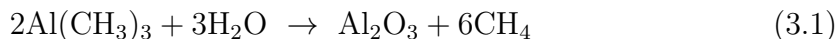
Alumina Case Study

Exhibiting a relatively well-behaved growth cycle, alumina ALD grown from trimethylaluminum (TMA) and water precursors is the prototypical experimental and modeling system. While TMA is a pyrophoric material and thus requires special care in handling, this high reactivity is a key factor in the success of the alumina deposition process. Additionally, liquid TMA has a sufficient vapor pressure for use in a pressure-drawn precursor delivery system, has high thermal stability, and the methane by-product released in reactions with water is benign. While TMA in large quantities could become expensive, it is only needed in small quantities at the research-scale and water is relatively inexpensive. Considering these benefits, the alumina ALD system has been perhaps the most intensely studied [44, 130] and consequently the best ALD process developed to date [140].

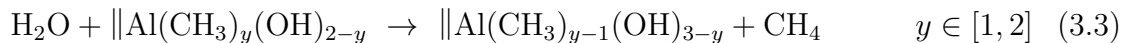
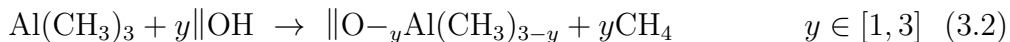
Yet, despite the attention paid to the alumina ALD system, much remains unknown regarding the specific reactions that take place on the growth surface, and no consistent picture has yet emerged in terms of the reaction kinetics of the overall film growth process. As a result of the significant experimental (*e.g.*, [117]) and

quantum-computational (*e.g.*, DFT reaction modeling, [40, 162]) studies, elements of the complete deposition reaction mechanism are beginning to emerge [36].

The model-based methodology presented in Chapter 2 was thus applied exclusively to a case study of sequential surface chemical reactions for the controlled deposition of alumina films using TMA and water precursors [156]. The overall alumina ALD reaction can be represented by its stoichiometrically equivalent CVD reaction as follows.



The corresponding ALD growth cycle has been the subject of several empirical investigations [26, 32, 75, 90, 102, 117, 118, 136, 138, 150, 174] in which the mechanisms for each half-cycle are suggested as follows.



Each alumina half-reaction is further broken down into elemental adsorption and surface reaction steps consistent with those outlined in Table 2.1. Many of the empirical studies cited above suggest molecular precursor adsorption followed by a ligand-exchange reaction. Subsequent studies also pose dissociative adsorption reactions for both TMA [23, 40, 91, 100, 130, 155] and water [35, 39, 60, 61, 75, 91, 118, 138, 155], although the relative importance of these reactions requires further

investigation.

Because of the near impossibility of experimentally measuring the dynamic ALD surface state in real time [117], researchers have turned to quantum chemical computations [37] to evaluate reaction mechanisms, bond configurations, and energetics. Included in the above cited studies are a number of first principles models developed to determine the mechanistic reaction pathways that are thermodynamically favored in ALD. The earliest of such studies reported for alumina was performed using DFT cluster models to predict reaction energetics and transition-state structures for adsorption and a single ligand exchange during both the TMA and water half-reactions [162].

Both reaction paths are initiated by barrierless precursor adsorption in which the oxygen lone-pair electrons interact with the empty p-orbital of the aluminum atom to form a stable Lewis acid-base adduct. If able to overcome an activation energy barrier, this adduct then proceeds to a methane-producing ligand-exchange reaction. As this methane-elimination reaction is rate-limiting and releases a CH_4 molecule to the gas-phase, it may be assumed irreversible [156]. A similar model was later developed that allows up to two ligand-exchange reactions during TMA exposure and goes on to predict growth rates in alumina ALD reactor simulations, although the modeling details were omitted [146].

Ab initio studies of the TMA half-cycle were further advanced in [39,40], where careful consideration was given to the sequence of TMA adsorption and ligand-exchange reactions occurring on bare (*i.e.* dehydroxylated) and fully hydroxylated substrates. On bare alumina, TMA was found to adsorb dissociatively onto bridged

oxygen sites. While film growth was predicted for bare alumina, high ALD growth rates were only possible when surface decomposition occurred in order to sufficiently prevent TMA desorption and maximize Al deposition. On fully hydroxylated alumina, TMA was found to adsorb molecularly and proceed through a ligand exchange, one of three possible methane-elimination reactions. This reaction is considered irreversible because of the removal of methane by the ALD process exhaust and because of the large energy barrier posed by the reverse reaction. The remaining AlMe_2 ($\text{Me} = \text{CH}_3$) fragment was found to then undergo a highly energetically-favored densification reaction with a neighboring hydroxyl group. Similar energetic favorability for densification reactions was also later reported in [23, 79, 80].

Ab initio studies of the water half-cycle were likewise advanced in [22,23], where the relative activation energies associated with the (1-2) H-transfer transition states were compared to the (1-4) H-transfer reactions resulting from adduct interactions with neighboring Me groups. The latter was found to be more energetically favored.

Following early mechanistic studies, a quantitative model was developed to predict saturating growth per cycle (*GPC*) for a subset of binary ALD reactions [128]. The model depends only on the stoichiometry of the metal precursor ligand-exchange reactions and assumes saturation is due to close-packing of the metal precursor ligands on the growth surface. This was used to theoretically validate that y in half-reaction (3.2) can vary from unity and that steric hindrance of the methyl groups is responsible for self-saturation during TMA exposure [129]. DFT results later confirm this theory, finding repulsion between methyl groups as the primary reason for weaker TMA adsorption with increasing methyl group coverage [100].

Expanding the scope of these studies beyond mechanistic analysis, a kinetic Monte Carlo simulation was developed where the primary focus was the definition of the growth-surface lattice and species accounting mechanisms [104]. Reaction transition probabilities were determined from DFT methods but the simulation results stopped short of predicting the saturation times for TMA and water exposures.

3.1 Modeling Objective

The study presented in this thesis chapter builds directly on the body of previously-cited quantum-chemical mechanistic studies, employing reported energetics and transition state structures to compute surface reaction kinetic parameters used in a model of surface coverage dynamics corresponding to alumina ALD growth. The goal is to understand the nonlinear connection between process parameters and the boundaries of the self-limiting growth region. At a minimum, the process parameters that must be investigated are deposition temperature, precursor partial pressures, the length of time corresponding to each exposure, and the thermochemical properties of the ALD reactions.

ALD process development is driven by first understanding the steady ALD growth phase (termed “homodeposition”) in which a constant growth rate is achieved over cycles of product-on-product deposition [38]. In introducing a novel ALD reaction kinetics model, it is thus practical to limit initial analyses to this steady growth phase, providing a conceptual theoretical framework for modeling homodeposition and introducing the concept of limit-cycle dynamic solution computations.

3.1.1 Formulation of Underlying Model Assumptions

A model encompassing TMA (precursor A) and water (precursor B) adsorption and subsequent surface reactions consists of two main components: a representation of the instantaneous state (chemical composition) of the growth surface and the chemical reaction material balances that govern the temporal surface state evolution.

Following the generally accepted mechanism in empirical [26, 32, 75, 90, 102, 117, 118, 136, 138, 150, 174] and theoretical [35, 55, 99, 129, 130, 136, 146, 162, 167] alumina studies, a relatively simple ALD reaction mechanism is assumed. Inherent in the reaction mechanism suggested are several simplifications to the alumina ALD process and assumptions in regard to the surface coverage model:

- (i) Only immobile surface species are considered, *i.e.* surface diffusion is neglected.
- (ii) All adsorption sites of the same type are assumed to be identical.
- (iii) The ALD system can be accurately represented with a Langmuir adsorption model, *i.e.* lateral adsorbate-adsorbate interactions are neglected.
- (iv) Only molecular adsorption is considered, *i.e.* dissociative adsorption is neglected.
- (v) The TMA ligand-exchange transition state is allowed to interact with up to two additional hydroxyl groups, leading to a monomethylaluminum or bare aluminum surface site.
- (vi) The TMA ligand-exchange reaction occurs with the (1-2) H-transfer mecha-

nism and energetics proposed in [162], and as such, elementary densification steps are neglected.

3.2 Chemical Reaction Mechanism

The sequence of elementary reaction steps considered in this model is given in the listings of Table 3.1 for the subset of TMA half-cycle reactions and Table 3.2 for the subset of water half-cycle reactions. The reaction energies for each reaction and the sources of those values are given in Table 3.4.

During the TMA half-cycle, TMA (species A) is reversibly adsorbed on surface hydroxyl groups X, forming surface adduct AX (R_1). The adduct AX can undergo a (1-2) H transfer reaction (R_3), passing through transition state AX^\ddagger (R_2). In this reaction sequence, the rate-determining step is the final irreversible reaction that adds $-Al(CH_3)_2$ to the growth surface and produces one methane molecule that desorbs to the gas phase. The two equilibrium reactions define the surface concentrations of the adduct, AX, and the transition state, AX^\ddagger , between the adduct and the final reaction products. The transition state can also interact with up to two additional hydroxyl groups to increase ligand elimination (R_4 and R_5).

During the water half-cycle, water (species B) is reversibly adsorbed on dimethylaluminum (DMA, S^d) or monomethylaluminum (MMA, S^m), forming surface adduct BS^d (R_6) or BS^m (R_9), respectively. In the case of the DMA adsorption site, the adduct BS^d can undergo a (1-2) H transfer reaction (R_7), passing through transition state $BS^{d\ddagger}$ and undergoing an irreversible ligand-exchange reaction. Similarly, the

BS^m adduct can undergo a (1-2) H transfer by proceeding through transition state $BS^{m\dagger}$. Both of the irreversible reactions of half-cycle B (R_8 and R_{11}) involve a 1:1 methyl to hydroxyl group loss and gain, respectively. In other words, an adsorbed water molecule can undergo only one methane-elimination reaction. This is in contrast to the TMA half-cycle where an adsorbed TMA molecule may react with up to three hydroxyl sites.

3.2.1 *The Surface State*

The main features of the alumina growth surface are the aluminum and oxygen atoms onto which water (B) and TMA (A) can adsorb. To characterize the growth surface, [X], [O], [S], [AX], [BS] and [Me] are noted as the hydroxyl, oxygen, aluminum, TMA-OH adduct, water-aluminum adduct and methyl group surface concentrations (species/nm²), respectively. Despite the amorphous nature of the alumina film, the instantaneous state of the surface is represented in the manner shown in Fig. 3.1, where the X,O,S checkerboard pattern corresponds to a grid of 0.295 nm \times 0.295 nm squares and the Me group radius of 0.2 nm [156].

Oxygen sites consist of surface oxygen bridges and surface hydroxyl groups, while methyl ligands can be bound to the surface aluminum atoms. Using brackets [] to denote species (surface or gas-phase) number densities and the “hat” (^) notation to denote a maximum value, surface coverages are defined as follows

$$\theta_X = \frac{[X]}{[\hat{X}]}, \quad \theta_O = \frac{[O]}{[\hat{O}]}, \quad \theta_{Me} = \frac{[Me]}{[\hat{Me}]} \quad (3.4)$$

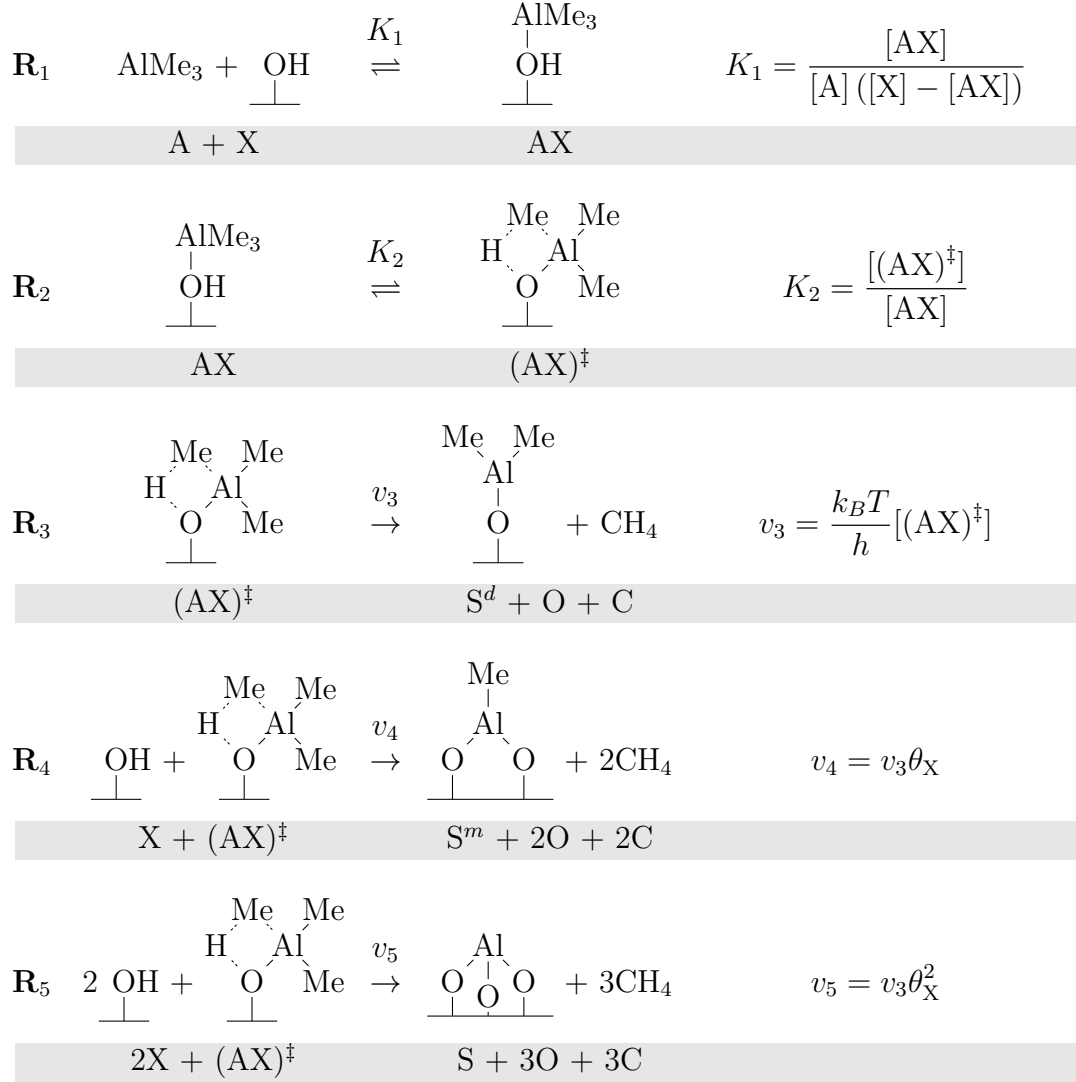


Table 3.1: A subset of elementary surface reactions taking place during TMA exposure as identified in [156]. $\text{Me} = \text{CH}_3$. d and m subscripts denote DMA and MMA surface species.

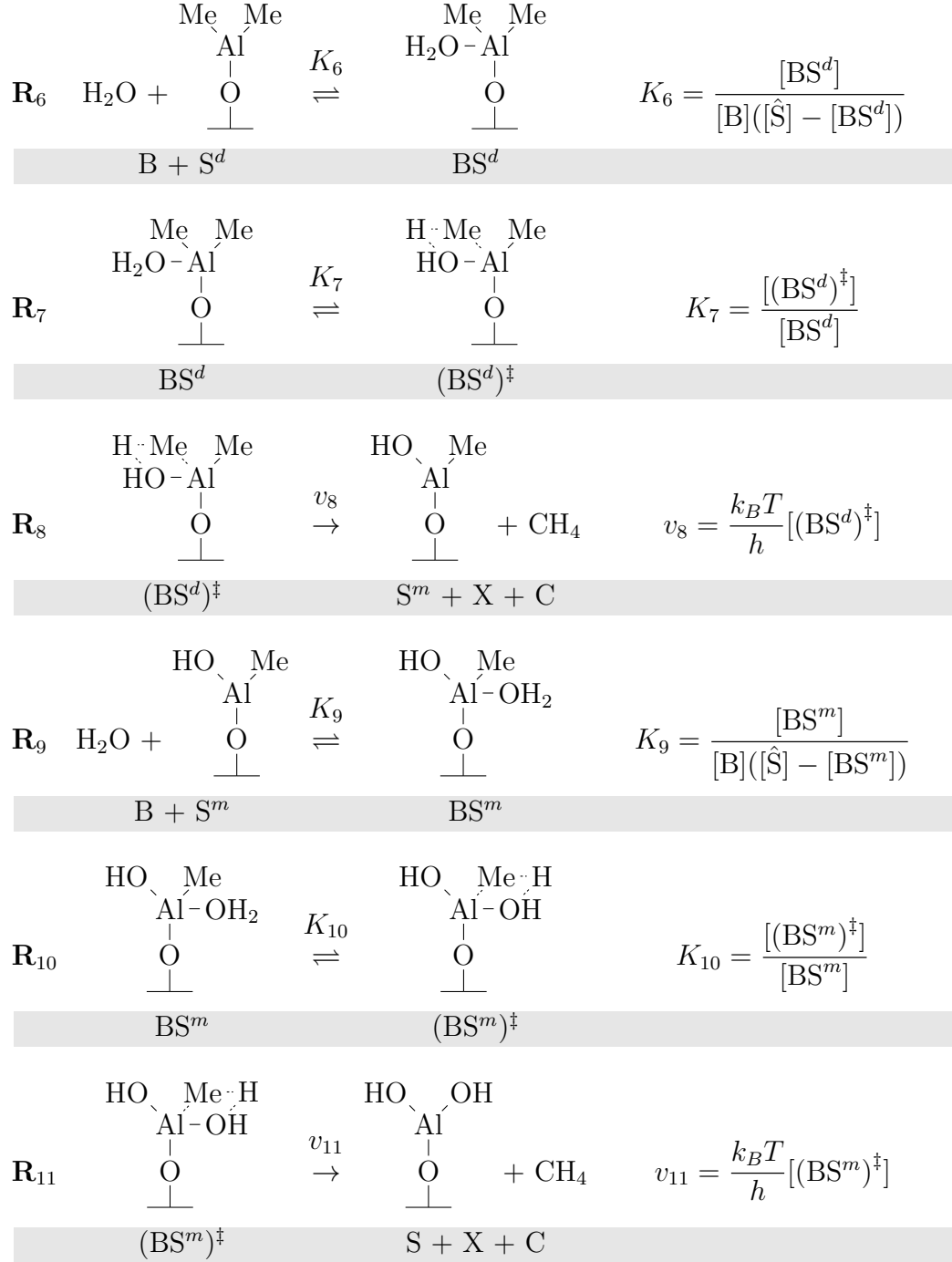


Table 3.2: A subset of elementary surface reactions taking place during water exposure as identified in [156]. $\text{Me} = \text{CH}_3$. d and m subscripts denote DMA and MMA surface species.

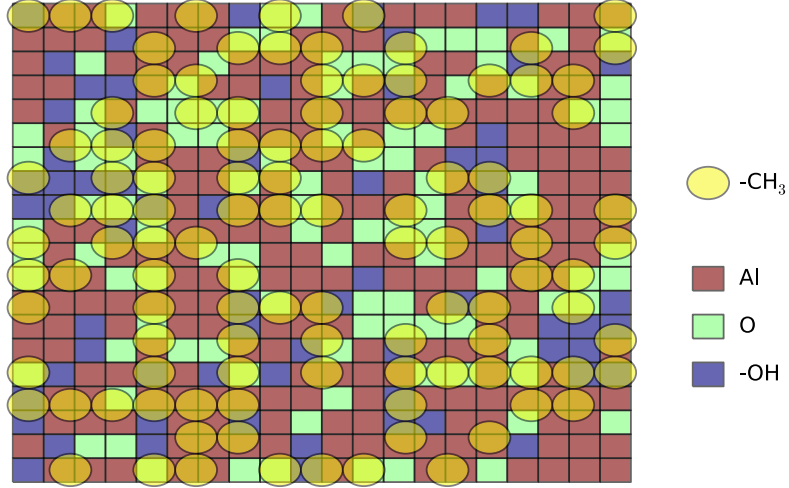


Figure 3.1: A snapshot of a 35 nm^2 portion of the ALD growth surface corresponding to $\theta_O = 0.6$ and $\theta_{Me} = 0.5$.

where site conservation requires $[O] + [X] = [\hat{X}]$ or $\theta_O + \theta_X = 1$. The fraction of the growth surface free of methyl groups ϕ_{Me} is defined as $(1 - \theta_{Me})$. Likewise, the fraction of the growth surface free of hydroxyl groups ϕ_X is defined as $(1 - \theta_X)$.

The limiting (maximum) concentrations of surface species are computed using the number density of the $\text{AlO}_{3/2}$ film molecular unit, a value equivalent to the number density of Al atoms in the Al_2O_3 film.

$$\varrho_N = \frac{\rho N_A}{m_{\text{AlO}_{3/2}}} \quad \text{molecules/cm}^3 \quad (3.5)$$

In this definition, N_A is Avogadro's number, $\rho = 3.3 \text{ g/cm}^3$ is the amorphous alumina film density [53], and $m_{\text{AlO}_{3/2}}$ is the molecular mass of the film minimal molecular unit $\text{AlO}_{3/2}$. Using these values, $\varrho_N = 39.0 \text{ nm}^{-3}$ and the alumina film monolayer thickness

$$\Delta_z = (\varrho_N)^{1/3} = 0.295 \text{ nm} \quad (3.6)$$

Table 3.3: *Surface reaction model parameters.*

Parameter	Description	Value
$[\hat{\text{Me}}]$	close-packing limit, surface Me	7.2 nm^{-2}
$[\hat{\text{O}}], [\hat{\text{X}}]$	alumina surface max O, -OH concentration	17.2 nm^{-2}
$[\hat{\text{S}}]$	alumina surface max Al concentration	11.5 nm^{-2}
P°	standard pressure	101325 Pa
r_{AlC}	Al-C bond length	$1.98 \times 10^{-10} \text{ m}$
r_{AlO}	Al-O bond length	$2 \times 10^{-10} \text{ m}$
ρ	amorphous alumina density	3.3 g cm^{-3}
ϱ_N	amorphous alumina number density	39.0 nm^{-3}
Δ_z	alumina film monolayer thickness	0.295 nm

These computations are similar to those presented in other literature [118,128]; the above computations give $[\hat{\text{S}}] = 11.5 \text{ nm}^{-2}$ and $[\hat{\text{O}}] = [\hat{\text{X}}] = 17.2 \text{ nm}^{-2}$ as the maximum surface Al, O, and X number concentrations. The maximum surface methyl group concentration $[\hat{\text{Me}}] = 7.2 \text{ nm}^{-2}$ is set as the close packing limit [128,130].

3.2.2 *Surface State Dynamics*

The essential self-limiting behavior of the alumina ALD process results from surface Me saturation ($[\text{Me}] \rightarrow [\hat{\text{Me}}]$) shutting down TMA adsorption. During the TMA half-cycle, the growth surface saturates with Me groups and during the water half-cycle, these groups are replaced with OH. Combining these effects and keeping in mind the reaction mechanism shown in Tables 3.1 and 3.2, the material balances over surface methyl and hydroxyl groups are given by

$$\frac{d[\text{Me}]}{dt} = v_3 \phi_{\text{Me}} (2 - \theta_{\text{X}} - \theta_{\text{X}}^2) - (v_8 + v_{11}) \phi_{\text{X}} \quad (3.7)$$

$$\frac{d[\text{X}]}{dt} = -v_3 \phi_{\text{Me}} (1 + \theta_{\text{X}} + \theta_{\text{X}}^2) + (v_8 + v_{11}) \phi_{\text{X}} \quad (3.8)$$

subject to initial conditions $[\text{Me}](t=0)$ and $[\text{X}](t=0)$ at the start of each half-cycle.

During the TMA half-cycle, the surface is depleted of available OH groups by the series of reactions (R_1 - R_5). Reaction (R_3) yields a DMA surface fragment which may undergo reactions (R_4) and (R_5), both resulting in an additional methyl group elimination subject to the availability of surface hydroxyl groups. During the water half-cycle, two irreversible reactions take place (R_8 , R_{11}), each removing one surface methyl group and replacing it with a hydroxyl group. One can see that the overall effects of the irreversible reactions (R_3 - R_5 , R_8 , R_{11}) on $d[\text{Me}]/dt$ and $d[\text{X}]/dt$ are nearly equal in magnitude but opposite in sign.

3.3 Surface Reaction Equilibria and Reaction Rates

Following the principles of transition state theory as derived in Chapter 2, the equilibrium and rate expressions for each elementary reaction step have been formulated for the TMA and water half-cycle and can be found in Tables 3.1 and 3.2, respectively. Recall that to solve these equations numerically, they must be formulated in terms of statistical partition functions considering the relative translational, rotational, vibrational, and electronic energy states of the molecules.

Ab initio energetics are extracted from DFT studies while *ab initio* computation of the entropic contributions to the equilibrium relationships are the main focus of this modeling section. Reaction energetics used in this study are listed in Table 3.4 while the statistical mechanical formulation of the equilibrium and rate expressions for reactions (R_1 - R_{11}) are given in Tables 3.5 and 3.6.

Table 3.4: *Reaction rate energetics data.*

Parameter	Description	Value (eV)	Source
ϵ_1	R ₁ adsorption energy	-0.61	[162]
ϵ_2	R ₂ activation energy	0.52	[162]
ϵ_6	R ₆ adsorption energy	-0.57	[162]
ϵ_7	R ₇ activation energy	0.70	[162]
ϵ_9	R ₉ adsorption energy	-0.74	[162]
ϵ_{10}	R ₁₀ activation energy	0.91	[162]

\mathbf{R}_1	$A + X \xrightleftharpoons{K_1} AX$	$K_1 = \frac{\mathcal{Z}_{AX}}{(\mathcal{Z}_A/V)\mathcal{Z}_X} e^{(-\epsilon_1/k_B T)}$
\mathbf{R}_2	$AX \xrightleftharpoons{K_2} (AX)^\ddagger$	$K_2 = \frac{\mathcal{Z}_{(AX)^\ddagger}}{\mathcal{Z}_{AX}} e^{(-\epsilon_2/k_B T)}$
\mathbf{R}_3	$(AX)^\ddagger \xrightarrow{v_3} S^d + CH_4$	$v_3 = \frac{k_B T}{h} \frac{\mathcal{Z}_{(AX)^\ddagger}}{(\mathcal{Z}_A/V)\mathcal{Z}_X} e^{[-(\epsilon_1 + \epsilon_2)/k_B T]} \frac{P_A[X]}{k_B T + \frac{\mathcal{Z}_{AX}}{(\mathcal{Z}_A/V)\mathcal{Z}_X} e^{(-\epsilon_1/k_B T)} P_A}$
\mathbf{R}_4	$X + (AX)^\ddagger \xrightarrow{v_4} S^m + 2CH_4$	$v_4 = \frac{k_B T}{h} \frac{\mathcal{Z}_{(AX)^\ddagger}}{(\mathcal{Z}_A/V)\mathcal{Z}_X} e^{[-(\epsilon_1 + \epsilon_2)/k_B T]} \frac{P_A[X]^2}{k_B T + \frac{\mathcal{Z}_{AX}}{(\mathcal{Z}_A/V)\mathcal{Z}_X} e^{(-\epsilon_1/k_B T)} P_A} [\hat{X}]$
\mathbf{R}_5	$2X + (AX)^\ddagger \xrightarrow{v_5} S + 3CH_4$	$v_5 = \frac{k_B T}{h} \frac{\mathcal{Z}_{(AX)^\ddagger}}{(\mathcal{Z}_A/V)\mathcal{Z}_X} e^{[-(\epsilon_1 + \epsilon_2)/k_B T]} \frac{P_A[X]^3}{k_B T + \frac{\mathcal{Z}_{AX}}{(\mathcal{Z}_A/V)\mathcal{Z}_X} e^{(-\epsilon_1/k_B T)} P_A} [\hat{X}]^2$

Table 3.5: Statistical mechanical formulation of equilibrium constants and rate expressions for elementary surface reactions taking place during TMA exposure as identified in [156]. Me = CH₃. *d* and *m* subscripts denote DMA and MMA surface species.

\mathbf{R}_6	$B + S^d \rightleftharpoons BS^d$	$K_6 = \frac{\mathcal{Z}_{BS^d}}{(\mathcal{Z}_B/V) \mathcal{Z}_{S^d}} e^{(-\epsilon_6/k_B T)}$
\mathbf{R}_7	$BS^d \rightleftharpoons (BS^d)^\ddagger$	$K_7 = \frac{\mathcal{Z}_{(BS^d)^\ddagger}}{\mathcal{Z}_{BS^d}} e^{(-\epsilon_7/k_B T)}$
\mathbf{R}_8	$(BS^d)^\ddagger \xrightarrow{v_8} S^m + X + CH_4$	$v_8 = \frac{k_B T}{h} \frac{\mathcal{Z}_{(BS^d)^\ddagger}}{k_B T + \frac{\mathcal{Z}_{BS^d}}{(\mathcal{Z}_B/V) \mathcal{Z}_{S^d}}} e^{[-(\epsilon_6 + \epsilon_7)/k_B T]} P_B[\hat{S}]$
\mathbf{R}_9	$B + S^m \rightleftharpoons BS^m$	$K_9 = \frac{\mathcal{Z}_{BS^m}}{(\mathcal{Z}_B/V) \mathcal{Z}_{S^m}} e^{(-\epsilon_9/k_B T)}$
\mathbf{R}_{10}	$BS^m \rightleftharpoons (BS^m)^\ddagger$	$K_{10} = \frac{\mathcal{Z}_{(BS^m)^\ddagger}}{\mathcal{Z}_{BS^m}} e^{(-\epsilon_{10}/k_B T)}$
\mathbf{R}_{11}	$(BS^m)^\ddagger \xrightarrow{v_{11}} X + CH_4$	$v_{11} = \frac{k_B T}{h} \frac{\mathcal{Z}_{(BS^m)^\ddagger}}{k_B T + \frac{\mathcal{Z}_{BS^m}}{(\mathcal{Z}_B/V) \mathcal{Z}_{S^m}}} e^{[-(\epsilon_9 + \epsilon_{10})/k_B T]} P_B[\hat{S}]$

Table 3.6: Statistical mechanical formulation of equilibrium constants and rate expressions for elementary surface reactions taking place during water exposure as identified in [156]. Me = CH₃. *d* and *m* subscripts denote DMA and MMA surface species.

3.4 Computation of Species Partition Functions

With complete derivations of the equilibrium and rate expressions from statistical mechanics and TST, computation of molecular partition functions are the necessary next step to numerically solve the expressions. While much of this discussion has centered around molecular interactions, it is sometimes more useful to look at a system in terms of energy storage modes, rather than of molecules.

Energy storage modes can be readily used to define a system unless they are truly interdependent. For example, a molecule which can store translational, rotational, vibrational, and electronic energy will have independent energy storage modes when the following applies.

$$\epsilon = \epsilon_{trans} + \epsilon_{rot} + \epsilon_{vib} + \epsilon_{elec} \quad (3.9)$$

Note that this equation neglects nuclear energy which is a constant background unless nuclear reactions occur. To handle the complexities of polyatomic molecules and to extract the necessary partition functions for the different energy storage modes, approximate methods must be used based upon a key assumption that the modes of energy storage are essentially independent. If the storage modes are truly independent, vibrational modes do not impact rotational, translational, and electronic modes and so forth. This assumption of energy storage mode independence is almost always a good approximation [66]. Implications of this assumption are as follows:

- (i) Molecule translation does not influence rotational or vibrational energy modes.

Table 3.7: *Molecular partition function contributions for a nonlinear polyatomic ideal gas. DOF, degrees of freedom. n, number of atoms in the molecule. ZPE, zero point energy.*

Mode	DOF	Equation
translation	3	$\mathcal{Z}^{trans} = \left(\frac{2\pi m k_B T}{h^2}\right)^{3/2} V$
rotation	3	$\mathcal{Z}^{rot} = \frac{1}{\sigma} \sqrt{\pi \left(\frac{8\pi^2 k_B T}{h^2}\right)^3 I_x I_y I_z}$
vibration	$3n - 6$	$\mathcal{Z}^{vib} = \prod_{n=1}^{3n-6} \frac{e^{-h\nu_n/(2k_B T)}}{1 - e^{-h\nu_n/(k_B T)}} \quad (\text{with ZPE})$
electronic		$\mathcal{Z}^{elec} = \sum_i \Omega_i e^{-\epsilon_i/(k_B T)} \quad i = 0, 1, 2, \dots$

(ii) Electronic energy levels do not influence rotational, vibrational, or translational energy modes.

(iii) Rotational and vibrational energy modes do not influence each other.

These last two assumptions are certainly approximations, but in many cases they work well. The assumption that energy storage modes are independent allows for the molecular partition function to be written as follows.

$$\mathcal{Z} = \mathcal{Z}^{trans} \mathcal{Z}^{rot} \mathcal{Z}^{vib} \mathcal{Z}^{elec} \quad (3.10)$$

These partition function contributions for a nonlinear polyatomic ideal gas are defined in Table 3.7.

Noting the structure of the equilibrium and rate expressions derived in Tables 3.5 and 3.6, computation of the absolute molecular partition functions are

unnecessary, as the partition function *ratios* (differences in energy modes between chemical species) are what ultimately define the kinetics of each elementary reaction. Thus, the motivation for not explicitly computing the internal contributions to the partition functions is that many of these components approximately cancel in the equilibrium relationships they ultimately define. Considering this, the partition function ratios will be derived for the equilibrium relationships in each ALD half-cycle.

3.4.1 *Half-cycle A*

3.4.1.1 R_1

The partition function ratio for the reaction (R_1) equilibrium relationship is developed according to the following:

- (i) TMA loses all translational freedom upon adsorption.
- (ii) TMA loses all but z-axis (“helicopter”) rotation upon adsorption [40], but rotational freedom of the bare adsorption site is retained. A new and substantial rotational mode is created by the angular momentum I_{AX} of the surface adduct [156] with $I_{AX} = \sqrt{3/4}m_A r_{AlO}^2$ where m_A is the mass of the adsorbed TMA and r_{AlO} is the length of the Al-O bond [40].
- (iii) All vibrational modes from the gas-phase TMA and bare adsorption site are retained. The Al-O bond made in formation of the adduct results in an additional stretching vibrational mode with frequency ν_{AlO} . Following [95], the vibrational frequency of the bond formed during adsorption is approximated

as

$$\nu_{AIO} = \frac{1}{2\pi} \sqrt{\frac{2\pi \rho_N \epsilon_1 r_{AIO}}{m_A}} = 1.1 \times 10^{12} \text{ s}^{-1} \quad (3.11)$$

which falls well within the expected range of frequency values.

- (iv) The electronic energy level difference can be extracted as the zero point energy difference and described by the adsorption energy ϵ_1 of the TMA molecule.

The partition function ratio for reaction (R₁) can thus be expressed as

$$\frac{\mathcal{Z}_{AX}}{(\mathcal{Z}_A/V) \mathcal{Z}_X} = \frac{1 / (1 - e^{-h\nu_{AIO}/k_B T})}{\left(\frac{2\pi m_A k_B T}{h^2}\right)^{3/2} \frac{\sigma_{AX}}{\sigma_A} \sqrt{\pi \left(\frac{8\pi^2 k_B T}{h^2}\right) I_{x,A} I_{y,A} / I_{AX}}} \quad (3.12)$$

3.4.1.2 R₂

The partition function ratio for the reaction (R₂) equilibrium relationship is developed according to the following:

- (i) While the combined rotation of the adduct with moment of inertia I_{AX} is retained, the z-axis TMA rotational mode and an internal rotational mode with moment I_{Me} is lost due to formation of the methane-elimination bond.
- (ii) All vibrational modes of the adduct are retained in the transition state.
- (iii) The electronic energy level difference can be extracted as the zero point energy difference and described by the reaction activation energy ϵ_2 .

The partition function ratio for reaction (R₂) can thus be expressed as

$$\frac{Z_{AX}^\ddagger}{Z_{AX}} = \frac{1}{\frac{1}{\sigma_{Me}} \sqrt{\pi \left(\frac{8\pi^2 k_B T}{h^2} \right)^2 I_{z,A} I_{Me}}} \quad (3.13)$$

These two partition function ratios complete the equilibrium expressions of half-cycle A and consequently also complete the reaction rate expressions for reactions (R₃-R₅).

3.4.2 Half-cycle B

3.4.2.1 R₆ and R₉

Reactions (R₆) and (R₉) are structurally similar and thus can be modeled in much the same way. The partition function ratios for these equilibrium relationships are developed according to the following:

- (i) Water loses all translational freedom upon adsorption.
- (ii) Water loses all but z-axis rotation upon adsorption, but rotational freedom of the bare adsorption site is retained. A new rotational mode is gained upon formation of the adduct with moment of inertia $I_{BS^{m,d}} = m_{BS^{m,d}} r_{AlO}^2$ where $m_{BS^{m,d}}$ is the mass of the respective adduct in reaction (R₆) or (R₉).
- (iii) All vibrational modes from the gas-phase water and bare adsorption sites are retained. A new vibrational mode with frequency $\nu_{AlO} = 1/2\pi \sqrt{2\pi \rho_N \epsilon_{6,9} r_{AlO} / m_B}$ is gained due to formation of the Al-O bond. In this formula, $\epsilon_{6,9}$ is the adsorption energy of water in each respective reaction (R₆ or R₉).

- (iv) The electronic energy level difference can be extracted as the zero point energy difference and described by the adsorption energy (ϵ_6 or ϵ_9) of the water molecule.

The partition function ratio for reaction (R₆) can thus be expressed as

$$\frac{\mathcal{Z}_{BS^d}}{(\mathcal{Z}_B/V) \mathcal{Z}_{S^d}} = \frac{1 / (1 - e^{-h\nu_{AlO}/k_B T})}{\left(\frac{2\pi m_B k_B T}{h^2}\right)^{3/2} \frac{\sigma_{BS^d}}{\sigma_B} \sqrt{\pi \left(\frac{8\pi^2 k_B T}{h^2}\right)} I_{x,B} I_{y,B} / I_{BS^d}} \quad (3.14)$$

and the partition function ratio for reaction (R₉) can be likewise expressed as

$$\frac{\mathcal{Z}_{BS^m}}{(\mathcal{Z}_B/V) \mathcal{Z}_{S^m}} = \frac{1 / (1 - e^{-h\nu_{AlO}/k_B T})}{\left(\frac{2\pi m_B k_B T}{h^2}\right)^{3/2} \frac{\sigma_{BS^m}}{\sigma_B} \sqrt{\pi \left(\frac{8\pi^2 k_B T}{h^2}\right)} I_{x,B} I_{y,B} / I_{BS^m}} \quad (3.15)$$

3.4.2.2 R₇ and R₁₀

Reactions (R₇) and (R₁₀) are also structurally similar and thus can be modeled in much the same way. The partition function ratios for these equilibrium relationships are developed according to the following:

- (i) While the combined rotation of the adduct with moment of inertia $I_{BS^m,d}$ is retained, the z-axis water rotational mode and an internal rotational mode with moment I_{Me} is lost due to formation of the methane-elimination bond.
- (ii) All vibrational modes of the adduct are retained in the transition state.
- (iii) The electronic energy level difference can be extracted as the zero point energy difference and described by the reaction activation energy (ϵ_7 or ϵ_{10}).

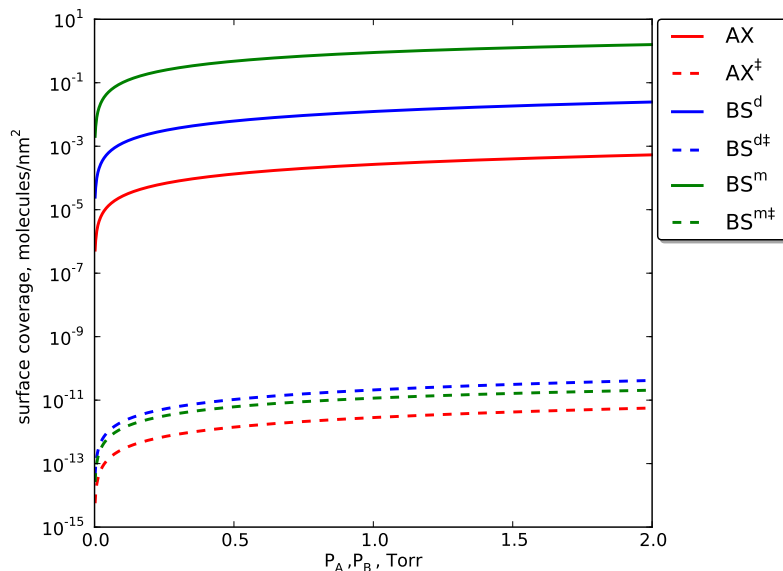


Figure 3.2: Predictions of the maximum adduct and transition state species surface coverages for $T = 500$ K and a range of precursor partial pressures.

The partition function ratios for both reactions (R_7) and (R_{10}) can thus be expressed as

$$\frac{\mathcal{Z}_{BS^{d\dagger}}}{\mathcal{Z}_{BS^d}} = \frac{\mathcal{Z}_{BS^{m\dagger}}}{\mathcal{Z}_{BS^m}} = \frac{1}{\frac{1}{\sigma_{Me}} \sqrt{\pi \left(\frac{8\pi^2 k_B T}{h^2} \right)^2 I_{z,B} I_{Me}}} \quad (3.16)$$

These four partition function ratios complete the equilibrium expressions of half-cycle B and consequently also complete the rate expressions for reactions (R_8) and (R_{11}).

3.5 Representative Surface Coverages and Reaction Rates

Equipped with all elementary reaction rate expressions, the expected growth surface coverage values for the TMA and water adduct species and their transition states are computed and shown in Fig. 3.2. Of the model predictions, the most significant are the small surface coverage values - that typically less than one molecule

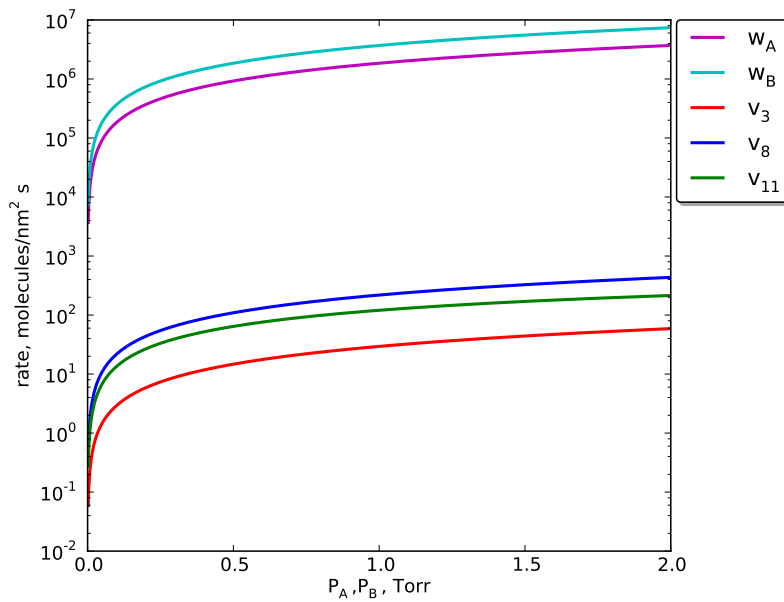


Figure 3.3: Predictions of the reaction rates for $T = 500\text{ K}$ and a range of precursor partial pressures. Gas-phase precursor wall collision frequencies, w_A and w_B , are shown for reference.

occupies an adsorption site per square nanometer at any instant in time. The water precursor adsorbs more effectively than TMA, and the adsorption step of (R₉) is favored over that of (R₆), but the forward reaction rate of (R₈) is faster than (R₁₁). Not surprisingly, the surface concentration of adducts in their transition states are several orders of magnitude smaller than the corresponding adduct species concentration. The important implication of this computation is that the adsorbed species would be very difficult to detect experimentally, and so surface state measurements correspond to permanently bound species [26].

While the adsorbed species concentrations are quite small, the corresponding reaction rate values are consistent with experimental observations. In Fig. 3.3, one can see that surface reaction rate values of >100 reactions/(nm²s) would result in surface saturation times of less than 1 s. The reaction rate for the water/MMA

reaction (R_{11}) is greater than that of (R_8), and both water reaction rates are significantly higher than that of TMA reaction (R_3). All computed reaction rates, though, are much less than the wall collision rates, suggesting that alumina ALD growth is kinetically-limited, as opposed to transport-limited.

3.6 Limit-cycle Solutions

At this point, the surface reaction model is complete and the dynamic nature of the growth surface can be studied as a function of surface state initial conditions and process operating parameters. In terms of the latter, the exposure of the growth surface to precursors A and B is characterized by the partial pressure of each precursor P_A and P_B and the length of each period τ_A and τ_B , resulting in the total exposure values of $\delta_A = P_A\tau_A$ and $\delta_B = P_B\tau_B$ with units 1 Langmuir = 10^{-6} Torr·s. Note that this model assumes constant precursor partial pressures over the duration of the pulse and an instantaneous reactor purge. Of course, the nature of the exposures experienced by a growth surface in a reactor would be of a time-dependent local partial pressure during the pulse period and during a portion of each purge period; modeling these features requires coupling the surface reaction model to a dynamic reactor transport model. This will be demonstrated in Chapters 5 and 6.

To make possible a systematic approach to studying the deposition dynamics, focus is placed on simulating an ABABAB... sequence of reaction steps, each corresponding to constant values of δ_A and δ_B , and computing the AB reaction cycle that would be found under cyclic operation after reaction surface nucleation and

other “unsteady” (with respect to cyclic operation) effects become unimportant. This *limit-cycle* behavior thus models steady reactor operation when P_A and P_B are constant during each pulse and the reactor purge is instantaneous.

3.6.1 A Collocation Procedure

Computation of the limit-cycle solutions requires a numerical procedure because of the nonlinear nature of the modeling equations (3.7, 3.8). Computing the AB limit-cycle over the time period $0 \leq t \leq \tau_A + \tau_B$ requires one additional important criterion: that the state of the surface returns to its initial condition at the end of the cycle $t = \tau_A + \tau_B$. The combination of initial conditions and the modeling equations (3.7, 3.8) constitute a set of ordinary differential and linear algebraic equations; this set of equations is reduced to a larger set of nonlinear algebraic equations using a collocation procedure, solving the algebraic equations using the Newton-Raphson method [18].

To implement the collocation method, the modeling equations over half-cycles A and B (3.7, 3.8) are written in vector form

$$\frac{d\mathcal{C}}{dt} = \mathbf{F}^A(\mathcal{C}), \quad \frac{d\mathcal{C}}{dt} = \mathbf{F}^B(\mathcal{C}) \quad (3.17)$$

where the species concentrations \mathcal{C} are subject to initial conditions for each full cycle $\mathcal{C}(0) = \mathcal{C}(\tau_A + \tau_B)$ and a condition requiring \mathcal{C} to be continuous at $t = \tau_A$. Using a simple polynomial Lobatto collocation technique over the unit interval with n_T collocation points for each half-cycle, $\mathbf{A}^{n_T \times n_T}$ is defined to be the discrete-ordinate

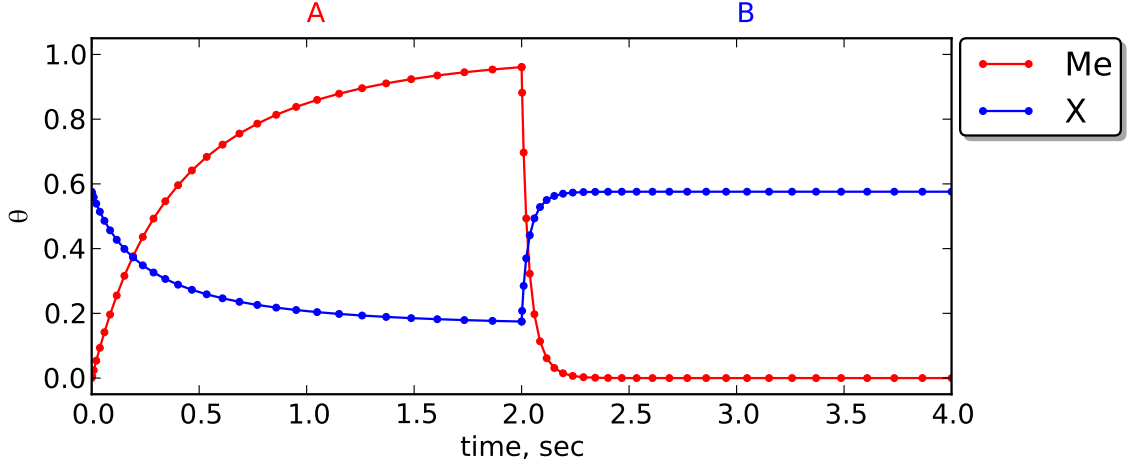


Figure 3.4: *Surface CH_3 and OH limit-cycle coverage dynamics for $P_A = P_B = 1$ Torr and $T = 500$ K. The red and blue curves denote surface Me and OH group coverage, respectively. Dots indicate collocation point locations.*

formulation of the 1st-order differentiation array and $\mathbf{A}_k^{1 \times n_T}$ the k th row of that array

$$\mathcal{C}_i(t_1) = \mathcal{C}_i(t_{2n_T}) \quad \mathcal{C}_i(t_{n_T}) = \mathcal{C}_i(t_{n_T+1}) \quad (3.18)$$

$$\mathbf{A}_k \mathcal{C}_i(\mathbf{t}^A) = \tau_A F^A(\mathcal{C}_i(t_k)) \quad \mathbf{A}_k \mathcal{C}_i(\mathbf{t}^B) = \tau_B F^B(\mathcal{C}_i(t_{k+n_T})) \quad (3.19)$$

for $k = 2, \dots, n_T$, surface species $i = Me, X$, and collocation points $\mathbf{t}^A, \mathbf{t}^B$. This is a straightforward orthogonal polynomial collocation on finite elements discretization procedure for forced-periodic systems.

A representative limit-cycle solution computed using the collocation procedure is shown in Fig. 3.4 where the state of the surface during the AB exposure cycle is plotted as a function of time. Under these conditions, the growth surface approaches, but does not fully reach a saturated state during the TMA pulse. During the water pulse, the surface completely saturates, replacing essentially all methyl ligands with

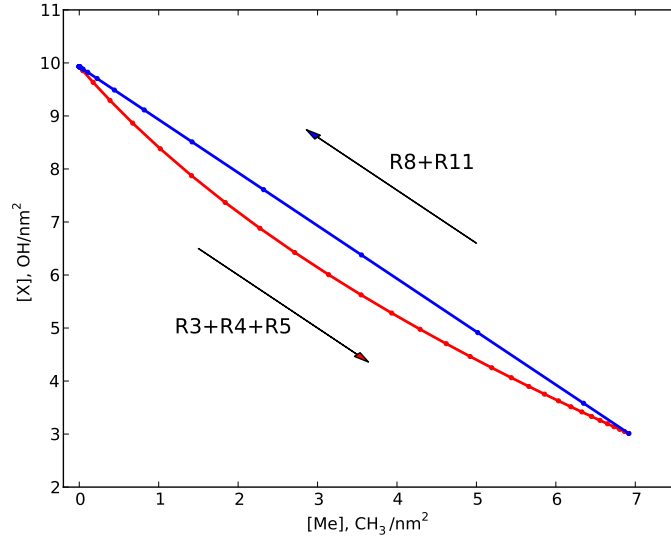


Figure 3.5: *Surface CH_3 and OH limit-cycle coverage dynamics for $P_A = P_B = 1$ Torr and $T = 500$ K. The red and blue curves denote the TMA and water doses, respectively. Dots indicate collocation point locations.*

hydroxyl groups.

An alternate view of this limit-cycle solution is shown in Fig. 3.5 where the changes in surface CH_3 and OH groups during the TMA and water doses are shown as the red and blue portions of the cycle, respectively. The linear nature of the water half-cycle dynamics is attributable to the form of the ligand-exchange reaction used in the surface material balance, where one reacting water precursor molecule results directly in the production of one CH_4 molecule desorbing to the gas phase. The curved nature of the TMA portion of the curve is due to the slower accumulation of CH_3 groups when the growth surface has a higher density of OH groups (recall R_4 and R_5), switching to a more rapid accumulation as CH_3 ligands are left by the TMA surface reactions.

3.7 *GPC* and Film Composition for Self-limiting Growth

Considering the ALD conditions which correspond to surface saturation by Me ligands during half-cycle A followed by a one-to-one exchange of Me ligands with OH during the water half-cycle B, the total number of Al atoms deposited from TMA must be $N_{Al} = 2[\hat{\text{Me}}]/3 = 4.8$ Al atoms/nm² and $N_O = [\hat{\text{Me}}] = 7.2$ atoms/nm². Of course, this results in a stoichiometric Al₂O₃ film; more importantly, the saturating ALD growth per cycle *GPC* can be computed as

$$GPC = 10q_N N_{Al} = 1.23 \text{ \AA/cycle} \quad (3.20)$$

essentially a perfect match to what is observed in practice for lower temperatures, *e.g.*, 180° C as described in [129]. This value of *GPC*, computed only from the film density and the assumption of close-packed Me groups as the saturating mechanism must be independent of temperature, pressure, and other operating conditions. The *GPC* for alumina ALD is known to decrease with increasing deposition temperature [131]. This modeling work focuses on the process-dependent dynamics of the saturation process, the temperature dependence modeling of *gpc* (undersaturated growth rate), and conditions leading to *GPC*.

3.7.1 *GPC and gpc*

An important consequence of the limit-cycle solution procedure is that one can now definitively quantify the difference between saturating ALD and non-saturating

film growth conditions. To make this distinction clear, $gpc(P_A, P_B, \tau_A, \tau_B, T)$ is introduced as the film growth rate per limit-cycle with

$$\max_{P_A, P_B, \tau_A, \tau_B, T} gpc = GPC \quad (3.21)$$

To compute gpc , recall that the number of Al and O atoms deposited per unit area over one deposition cycle are N_{Al} and N_O atoms/nm², respectively. These values can be computed by integrating the reaction rates over each half-cycle

$$N_{Al} = \int_0^{\tau_A} v_3 dt \quad (3.22)$$

$$N_O = \int_{\tau_A}^{\tau_A + \tau_B} (v_8 + v_{11}) dt \quad (3.23)$$

using the quadrature weights of the collocation procedure [18]. The gpc then is computed in the same manner as in Eqn. (3.20). Note that all of the results presented in this study were found to correspond to the stoichiometric N_{Al}/N_O ratio of 2/3.

3.8 A map of $gpc(\delta_A, \delta_B)$

To illustrate the dependency of gpc as a function of both precursor exposure levels for a fixed precursor pressure of $P_A = P_B = 1$ Torr and fixed temperature $T = 500$ K, a $gpc(\delta_A, \delta_B)$ map was generated by computing the limit-cycle solutions over a range of τ_A and τ_B ; the results are shown in Fig. 3.6. The location of the representative limit-cycle solution of Figs. 3.4 and 3.5 is marked as 2 on this plot, indicating its position outside the self-limiting growth domain, in a region where the

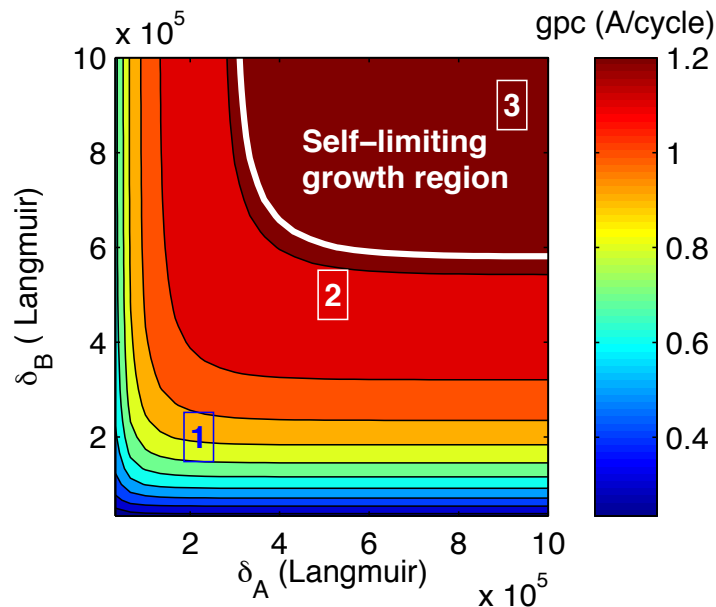


Figure 3.6: A map of gpc as a function of precursor exposure level for $P_A = P_B = 1$ Torr. The point marked 2 corresponds to $\delta_A = \delta_B = 5 \times 10^5$ and to the conditions of Figs. 3.4 and 3.5.

water exposure is non-saturating. For the purposes of this study, the self-limiting growth region is considered as the set of process operating conditions producing a steady film growth rate greater than a set fraction (*e.g.*, 98%) of the saturating GPC .

An important and completely expected feature of the gpc map in Fig. 3.6 is the large plateau of self-limiting growth found when both precursor doses saturate the growth surface in the limit-cycle solution. Saturation is achieved when the product of dose pressure and exposure time is above some critical value for both of the precursors - for this model of alumina deposition, the dark red region of Fig. 3.6 with a boundary defined by 98% of fully saturating cyclic film growth. The self-limiting growth region in the dosage plane is bordered by a steep drop off to zero growth in the limits of zero dose of each precursor. Note the qualitative similarities

between these computations and the film deposition efficiency plots of [121].

3.8.1 Comparison to Measured Exposures

Fig. 3.6 demonstrates the lower boundary for self-limiting growth consists of a curve in the (δ_A, δ_B) plane; for this set of precursor partial pressures and deposition temperature, the saturating ALD conditions correspond to δ_A, δ_B both $> 6 \times 10^5$ L. Model predictions will now be compared to TMA and water exposure levels found in the literature.

When reviewing the alumina ALD literature in which precursor exposure levels can be extracted, one will find that the conditions indicated can correspond to partial or saturating doses. In some cases, exposure values can be estimated based on the experimental conditions reported. For example, time-resolved FTIR measurements demonstrated that the ALD surface reactions were completed after 210 s during the TMA exposure and 180 s during the subsequent water exposure at 500 K and 0.01 Torr precursor partial pressure for both cases, giving total A/B exposures of 2.1×10^6 and 1.8×10^6 L, respectively [26]. The authors of the cited study note that mass transport limitations introduced by the porous substrate were not taken into account [3].

In another study, sequences of one to five 1 s pulses of D₂O were used for the water dose; given their reactor operating pressure of 2 mbar, a rough upper estimate of the exposures necessary for saturation of the water reactions ranges from 1.5×10^6 to 7.5×10^6 L [75]. These relatively high exposure values may be contrasted to another case where a rate constant $k_2 = 0.004 \times 10^{-6}$ Torr⁻¹ s⁻¹ corresponding

to the slowest water reaction mode was identified from ALD experiments taking place at 300 K and ultralow precursor partial pressures [150]. The rate constant in the cited work is reported as $k_2 = 0.004 \text{ Torr}^{-1} \text{ s}^{-1}$, a value confirmed to actually be $k_2 = 0.004 \times 10^{-6} \text{ Torr}^{-1} \text{ s}^{-1}$ [126]. In this case, one can directly compute the exposure $\delta_B = -(\ln 0.001)/k_2 = 1700 \text{ L}$ which would result in 99.9% reaction saturation.

Exposures also can be extracted from time-resolved reactor process pressure data. For example, in [118], a TMA/water dosing procedure was illustrated along with the measured deposition chamber pressure as a function of time. After each pulse, the chamber pressure drops in the manner of a first-order dynamical system with the single time constant given by the ratio of chamber volume to pumping speed. Fitting the pressure traces to a chamber pressure dynamic model, exposures of 1.2×10^5 and $1.7 \times 10^5 \text{ L}$ are estimated for TMA and water, respectively. A commercial ALD reactor system is also considered, where exposure estimates of $8.4 \times 10^4 \text{ L}$ for both the TMA and water pulses in a saturating-dose recipe for alumina ALD in the Savannah 100 reactor can be computed using this procedure [144].

The data cited above give some indication as to the variability in exposures reported in the literature for the TMA/water alumina ALD reaction system. However, the model predictions are of the correct order with respect to the majority of reported exposure levels, with the variability attributable to the differing precursor partial pressures and reactor-specific aspects of the individual studies cited. Model predictions will now be examined in more detail to clarify the role played by deposition temperature on *gpc* and the self-limiting growth boundary location.

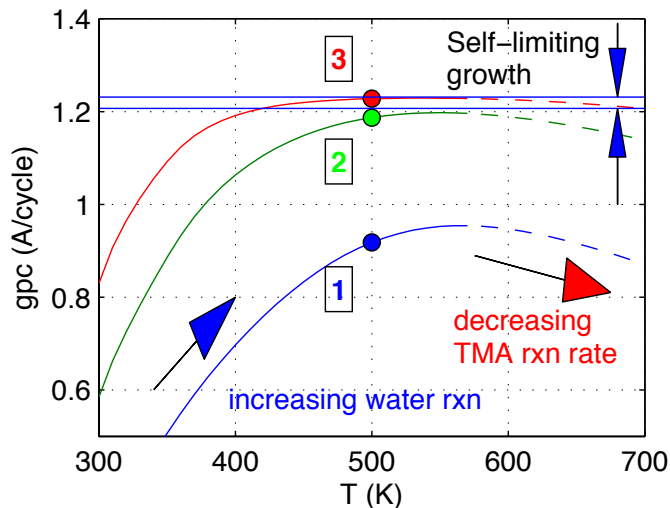


Figure 3.7: *Effect of temperature on gpc for $P_A = P_B = 1$ Torr. Blue curve corresponds to $\delta_A = \delta_B = 2 \times 10^5$ L, green to $\delta_A = \delta_B = 5 \times 10^5$ L, and red to $\delta_A = \delta_B = 9 \times 10^5$ L. Dashed curve segments indicate the temperature range where TMA decomposes [129].*

3.8.2 Effect of Deposition Temperature

Recall that the ALD *GPC* (3.20) is not a function of temperature or any other processing condition. Returning to the $P_A = P_B = 1$ Torr, $T = 500$ K *gpc* map of Fig. 3.6, the three exposure-value sets of δ_A , δ_B will be examined. Maintaining those three sets of conditions as constant, the corresponding $gpc(T)$ as a function of temperature can be computed in Fig. 3.7 with the $T = 500$ K points marked.

Operating condition 1 corresponds to an under-saturating set of exposure values for $T = 500$ K. One can observe that the $gpc(T)$ for this set of exposures drops significantly for $T < 500$ K as well as for $T > 600$ K – there is no self-limiting growth region under these conditions [140]. The *gpc* behavior can be traced to the relative reaction rates of TMA and water: the TMA reacts aggressively at low (*e.g.*, room) temperatures compared to water. However, the water reaction rate quickly

climbs with temperature, only to be modulated by the TMA reaction rate which decreases with increasing temperature. As temperature increases, the entropy of the gas-phase precursor molecules increases significantly, making desorption more favorable and consequently lowering the equilibrium surface coverage, thus lowering the limit-cycle growth rate under these non-saturating conditions.

Additional insight into the initial increase in $gpc(T)$ with temperature can be gained by closer examination of the water reaction thermodynamics. As listed in Table 3.4, the desorption energies of the water reactions are smaller in magnitude relative to the activation energies for the forward, B-cycle deposition reactions. Thus at low temperatures the water deposition reaction is limited by its activation energy barrier, making it thermodynamically more feasible for adsorbed water molecules to desorb than to proceed through the surface ligand-exchange reaction. As temperature increases, the activation energy of the water surface reaction is more easily overcome and an increase in growth is to be expected. However, when temperature is further increased, gas-phase water molecules become much more favored entropically, leading to lower adsorption and reaction.

For the nominal dosage conditions [2], the $gpc(T)$ peak approaches GPC and then the curve flattens and widens into the ideal self-limiting growth region for even higher exposures [3]. Each curve is bounded by the gpc gradients associated with reduced water and TMA reaction rates at low and high temperatures. As stated earlier, it is important not to confuse the temperature dependency of gpc described here with that of GPC described elsewhere. For example, the reduction of GPC at high temperatures generally is attributed to the reduction of surface OH groups with

increasing temperature [131]. While the model findings herein do not relate to the temperature dependency of *GPC*, the TMA reaction rate reduction predicted by the model might play a role in confounding the true mechanism for *GPC* reduction with temperature. Consider, for example, the work of [163, 164] who find that an increase in temperature may also cause a decrease in observed growth rate due to increased desorption competition of the adsorbed precursor. Further clarification of the role of temperature in both *gpc* and *GPC* is worthy of additional study.

3.9 Concluding Remarks

In this chapter, an alumina surface reaction kinetics model was derived based on transition state theory. Energetic and configurational data were adopted from published quantum-chemical computations and used to define partition functions of the reaction equilibrium relationships governing adsorbed surface species concentrations and reaction rates. The primary goal was to derive a tractable deposition model from which quantitative rate information could be extracted. The resulting rate expressions were incorporated into time-dependent reaction material balance expressions accounting for the temporal evolution of the surface states during each exposure period. The surface reaction models were treated as true dynamic systems, with continuous reactor operation described by limit-cycle solutions, numerically computed using a polynomial collocation technique.

The work described in this chapter was motivated by the predictive capabilities of physically based models to decouple the effects of precursor pressure, exposure

time, reactor temperature, and the dynamics of each exposure period on *gpc*, a measure of film growth per limit-cycle which is defined and distinguished from the fully saturating *GPC*. As such, the model demonstrated a good match between its predictions and observed deposition behavior in experimental alumina ALD studies. In particular, the model appears to predict the correct magnitude of TMA and water exposures required to achieve self-saturating ALD growth, with essentially no adjustable parameters. Further refinement of the reaction kinetics model, derivation of additional rate expressions, and derivation of surface species conservation equations to describe a more comprehensive reaction mechanism will be demonstrated in the following chapter.

4

Kinetic Mechanism Analysis

The alumina ALD reaction mechanism with trimethylaluminum and water precursors has been the subject of several experimental [26, 32, 75, 90, 102, 117, 118, 136, 138, 150, 174] and theoretical [35, 55, 99, 129, 130, 136, 146, 162, 167] studies. The mechanism presented in the previous chapter is consistent with the generally accepted chemisorption and ligand-exchange reaction mechanism. However, as more atomic-scale simulations arise, additional details are gained about the hydrogen transfer path and densification mechanisms involved in elementary ALD reaction steps. This yields a much more complex network of reactions for both ALD half-cycles and consequently more complex surface dynamics.

For instance, several studies pose dissociative adsorption reactions for both TMA [23, 40, 91, 100, 130, 155] and water [35, 39, 60, 61, 75, 91, 118, 138, 155], reactions which are often not captured in kinetics model formulations. Additionally, DFT computations have suggested H transfer mechanisms for the TMA [23, 40] and water half-cycle reactions [22, 23] along with densification mechanisms [40, 79, 80].

In this chapter, a more comprehensive network of elementary reactions is pre-

sented, incorporating suggested mechanisms from several quantum-chemical computational studies. Specifically, dissociative adsorption reactions of both precursors are included and densification reactions are assumed to occur barrierlessly and thus immediately [23]. Surface reaction rate predictions, based on thermodynamics and suggested reaction mechanisms from alumina homodeposition [40, 60, 61, 146, 162] and heterodeposition [23, 55, 74, 79, 80] studies, are compared. From this analysis, a kinetically favored reaction mechanism will be suggested.

Finally, the first principles surface reaction model will be used to examine relative rates of competing surface reactions to determine which reactions are crucial to the deposition process by determining the rate-limiting steps of the overall reaction *as the reaction proceeds in time during both precursor pulses*.

H transfer paths were comprehensively analyzed for both TMA and water half-reactions. In all of the cited studies considered in this mechanistic analysis, (1-2) H transfer reactions were suggested as the primary mechanism of surface reactions during the TMA half-cycle, *i.e.* the first TMA ligand-exchange reaction occurs on the surface site onto which the TMA molecule initially adsorbs. A (1-5) H transfer reaction was also considered in [23], but the (1-2) reaction was found to be energetically favored. The resulting dimethyl moiety can then relax to an energetically more-favored 4-coordinate Al through a barrierless densification reaction [23, 40, 79, 80]. Overall, TMA was shown to react with up to three OH sites to form a nearly 4-coordinated Al atom complex when OH groups were available at sufficient proximity, although the third methane-elimination reaction was found to be unfavored energetically.

Barrierless dissociative TMA adsorption was found to occur on locally bare (*i.e.* dehydroxylated) alumina. In this case, TMA adsorbs onto an oxygen bridge and distributes up to two of its Me ligands amongst neighboring surface aluminum atoms, although the second dissociation reaction requires activation [40].

In addition to the TMA half-cycle, the detailed H transfer mechanism was investigated for the water half-cycle in [23]. Unlike the (1-2) H transfer mechanism suggested elsewhere [55, 146, 162] the proposed water reaction involves two MMA species. The water molecule was found to adsorb via the known Lewis acid-base interaction with a surface aluminum, but sharing one hydrogen with an oxygen bound to a neighboring MMA species. From this configuration, a (1-4) H transfer reaction was strongly favored over the (1-2) reaction, the first yielding a 3-coordinate hydroxyl group and the latter a 2-coordinate hydroxyl group.

4.1 Surface Reaction Mechanism

Consistent with the notation introduced in Chapter 3, A and B will be used to designate gas-phase TMA and water, respectively. X' , O' , and S represent surface hydroxyl groups (Al-OH), oxygen bridges (Al-O-Al), and surface Al respectively. The prime (') notation is introduced to represent 2-coordinate oxygen (O and X) and 3-coordinate Al to distinguish them from the 3 and 4-coordinate species representative of the bulk film [53]. The concentration of these sites is conserved during the reactions resulting in $[X]+[X']+[O]+[O']=[\hat{X}]$ where the “hat” (^) notation is used to denote a maximum surface concentration as identified in the previous chap-

ter. Other surface species, such as TMA adsorbed on X and O will be denoted by AX and AO, respectively; activated complexes (*i.e.* transition states) are designated with a double dagger superscript (\ddagger).

The comprehensive set of elementary chemical reactions considered in this study are given in Tables 4.1 through 4.7, beginning with the TMA half-cycle reactions, followed by the water half-cycle reactions, and ending with a CVD-like gas-phase reaction. In each reaction table, equilibrium constants and reaction rate formulations are given in terms of molecular concentrations. As with the surface reaction model derived in Chapter 3, the equilibrium constants and reaction rates are also derived in terms of molecular partition functions based on assumptions regarding the *change* in translational, rotational, and vibrational degrees of freedom which arise in equilibrium relationships.

The modeling theory (*i.e.* TST and *ab initio* formulation of kinetic parameters) used in this chapter is consistent with the methodology presented in Chapter 3. Thus, derivations of the molecular partition functions have been omitted. Instead, the assumptions used in computing the partition function ratio for each equilibrium relationship are provided. These formulations are given in Tables 4.10 through 4.14. The corresponding reaction energies for each equilibrium reaction and the sources of those values are given in Tables 4.8 and 4.9.

Note that in the notation while I_{Me} only corresponds to *internal* rotation of a single Me group, $I_{Me'_2}$ corresponds to the *total* partition function contributions of two surface Me groups along with that of the adsorption site; hence depending on the structure of the complex, these contributions may include vibrational and other

rotational components in addition to the internal rotational contribution of the Me groups themselves.

The key differences in the reaction model presented in Chapter 3 and the model presented in this study are as follows.

- (i) Densification is now considered to occur spontaneously (*i.e.* strongly favored energetically) after ligand-exchange reactions [23,40,79,80]. As a consequence, the DMA and MMA species involved in the water half-cycle reactions involve a 4-coordinate aluminum.
- (ii) Additional surface reactions beyond the initial TMA ligand exchange (*e.g.* with DMA and MMA species) are modeled independent of pressure [23,40].
- (iii) Dissociative adsorption is now considered for both precursors [40,60,61].
- (iv) A gas-phase side-reaction is considered during non-ideal ALD conditions when precursor gases coexist in the reaction chamber [111].

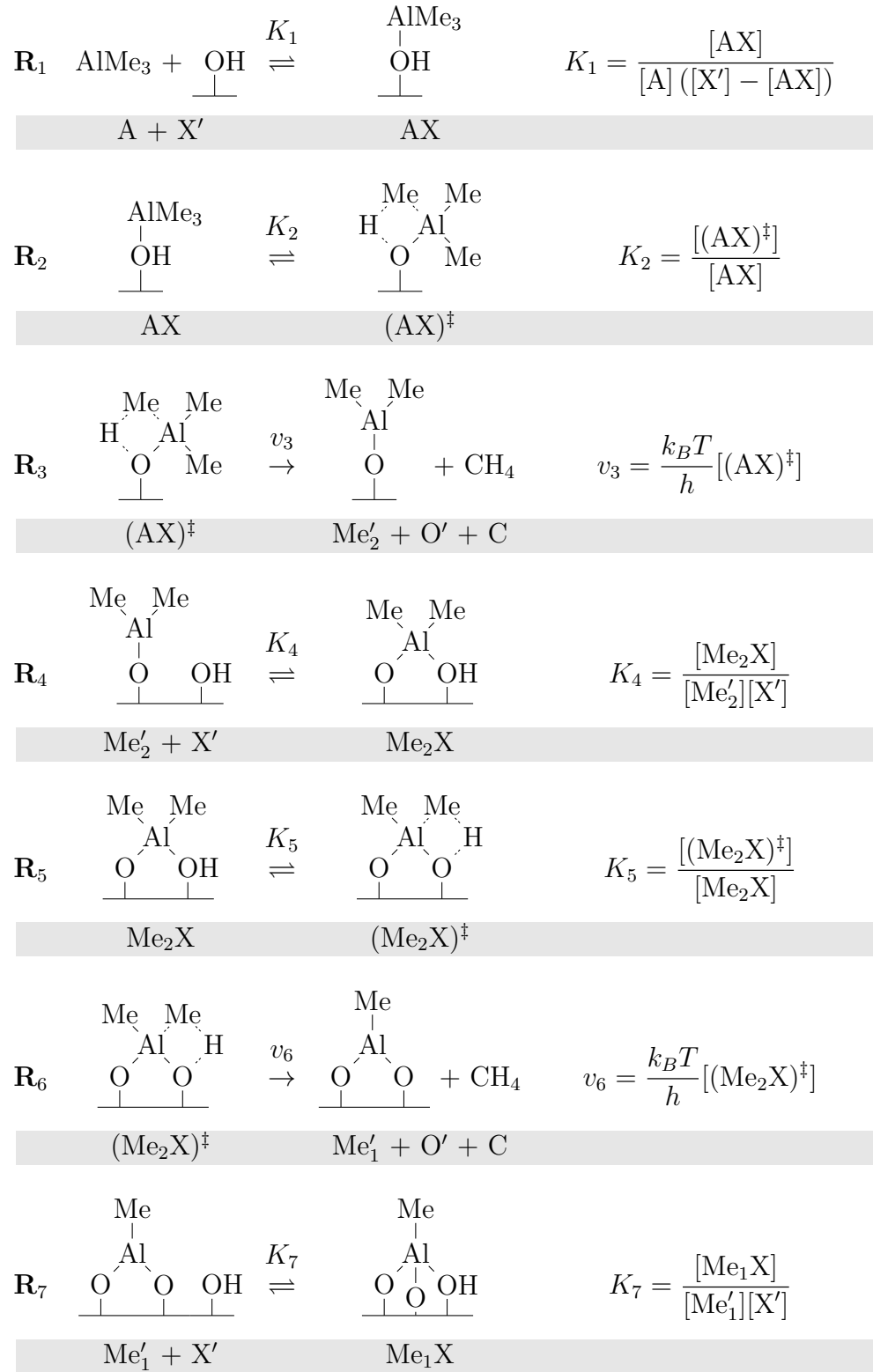


Table 4.1: A subset of elementary surface reactions taking place during TMA exposure, beginning with molecular adsorption. $\text{Me} = \text{CH}_3$.

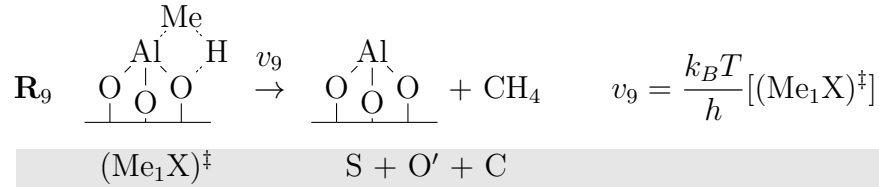
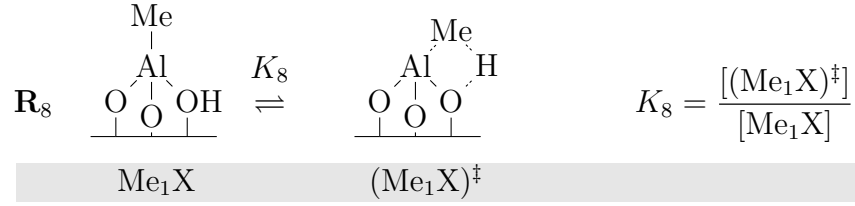


Table 4.2: continued from Table 4.1. A subset of elementary surface reactions taking place during TMA exposure, beginning with molecular adsorption. $\text{Me} = \text{CH}_3$.

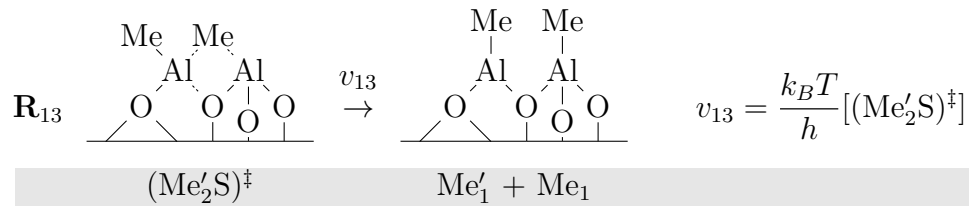
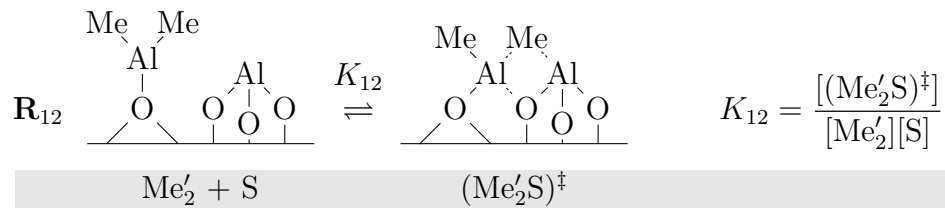
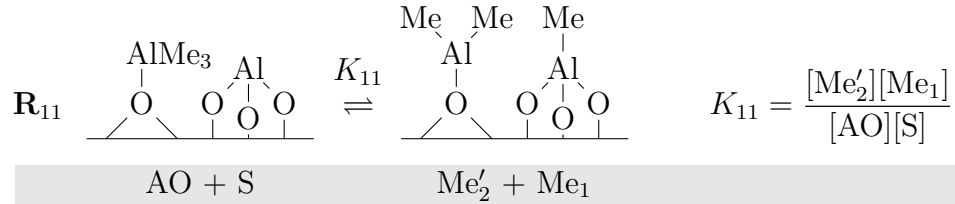
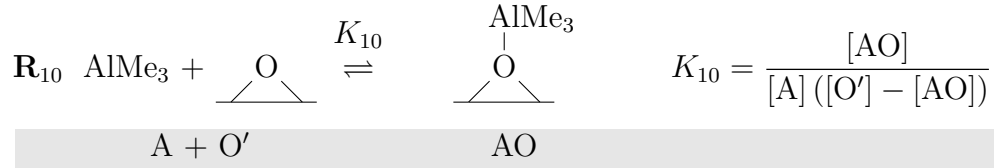


Table 4.3: A subset of elementary surface reactions taking place during TMA exposure, beginning with dissociative adsorption as described in [40]. $\text{Me} = \text{CH}_3$.

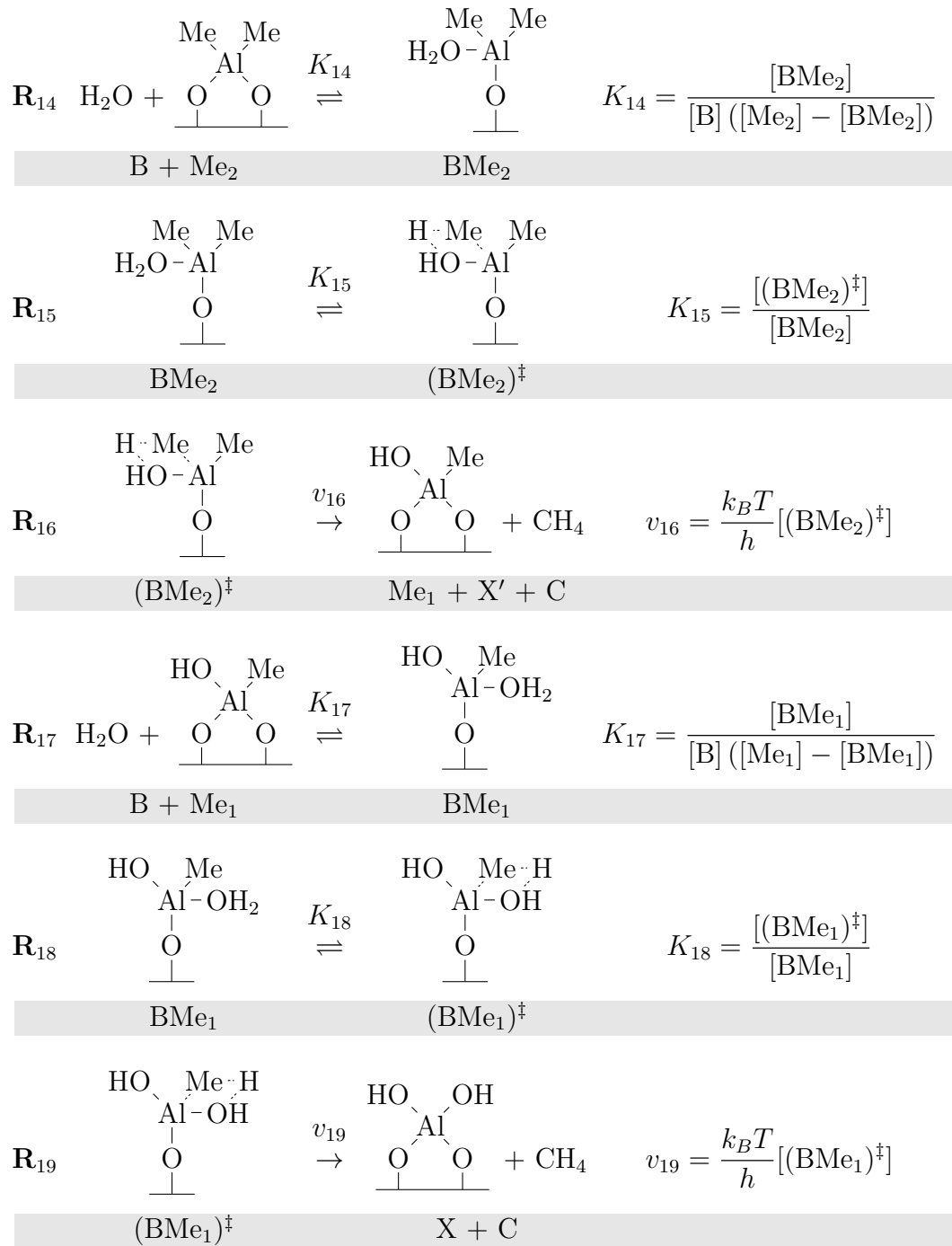


Table 4.4: A subset of elementary surface reactions taking place during water exposure, beginning with molecular adsorption. $\text{Me} = \text{CH}_3$.

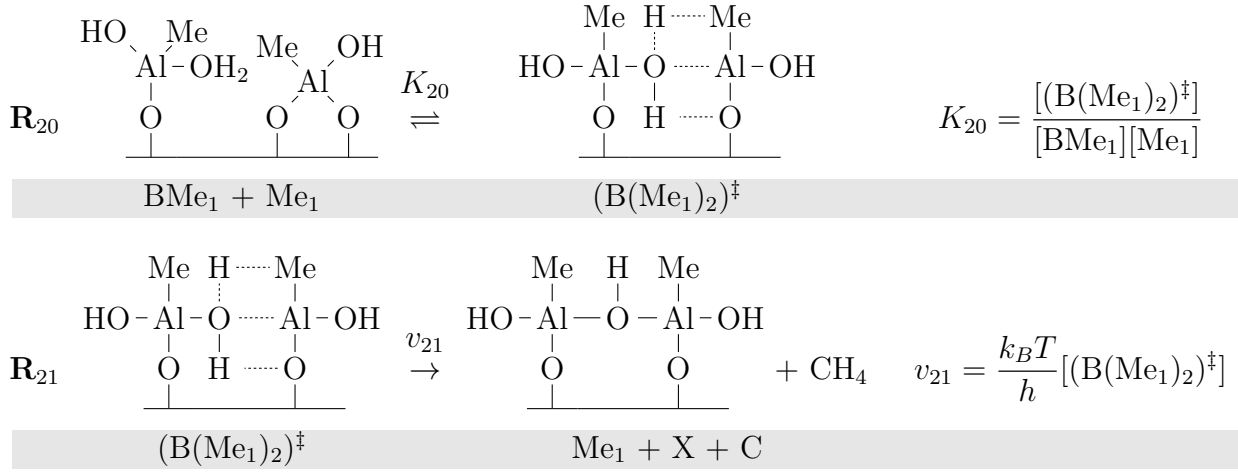


Table 4.5: A subset of elementary surface reactions taking place during water exposure as described in [23]. $\text{Me} = \text{CH}_3$.

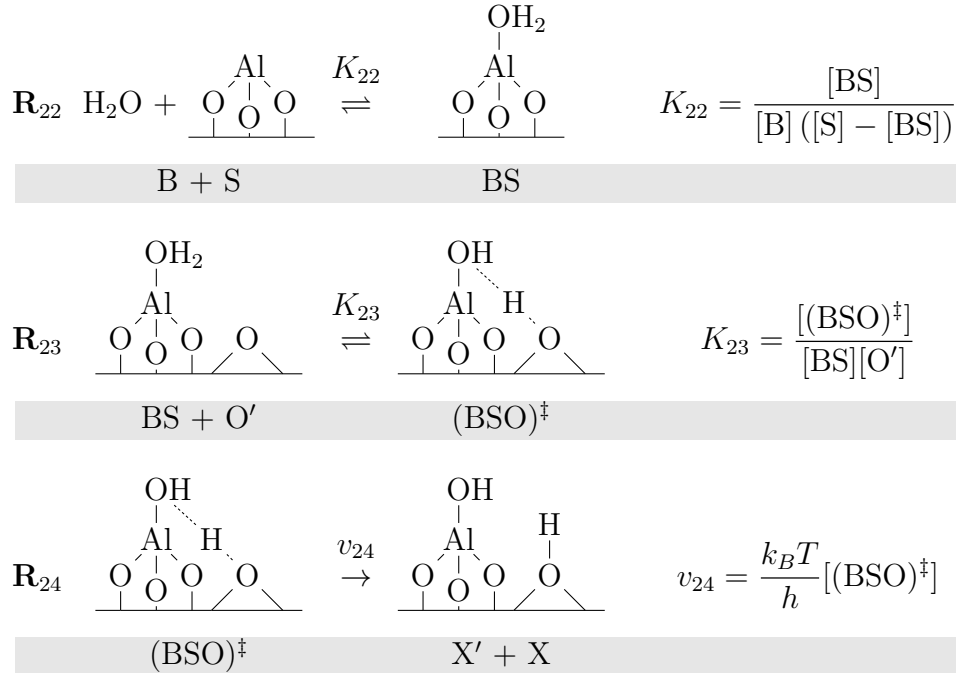


Table 4.6: A subset of elementary surface reactions taking place during water exposure, beginning with dissociative adsorption as posed in [60, 61]. $\text{Me} = \text{CH}_3$.

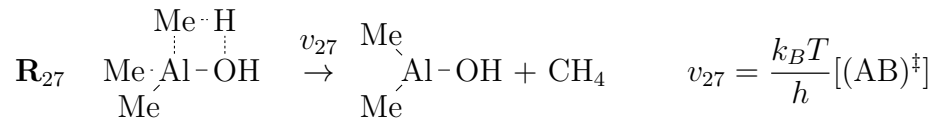
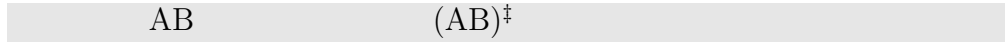
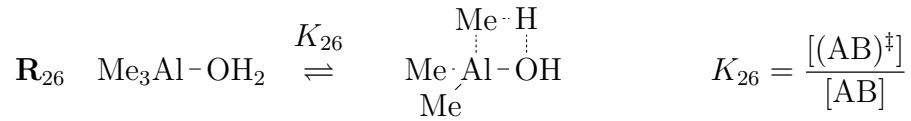
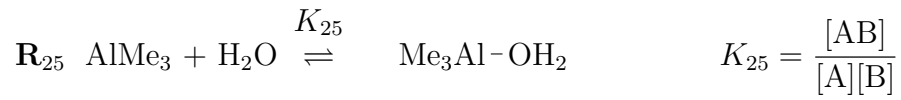


Table 4.7: A set of elementary gas-phase reactions taking place when both TMA and water are present [111]. $\text{Me} = \text{CH}_3$.

Table 4.8: *Reaction rate energetics. Plot estimate values noted with an asterisk (*). In the instance of multiple values for a parameter, the value used in the dynamic growth model is noted with a dagger (†). Alumina homodeposition studies are noted with a plus sign (+), otherwise all other studies correspond to alumina heterodeposition onto Si-OH substrates.*

Parameter	Description	Value (eV)	Source
ϵ_1	R ₁ adsorption energy	-0.70	[40] ⁺
		-0.70	[79, 80]
		-0.62 [†]	[113] ⁺
		-0.61	[162] ⁺
		-0.59	[55]
		-0.49	[23]
		-0.46	[74]
ϵ_2	R ₂ activation energy	1.04	[74]
		0.52	[162] ⁺
		0.51	[146] ⁺
		0.50	[79, 80]
		0.45 [†]	[113] ⁺
		0.48	[23]
		0.40	[55]
	0.26*	[40] ⁺	
ϵ_4	R ₄ reorganization energy	-0.62	[79, 80]
		-0.60 [†]	[40] ⁺
ϵ_5	R ₅ activation energy	1.09 [†]	[40] ⁺
		0.96	[23]
		0.21	[79, 80]
ϵ_7	R ₇ reorganization energy	-1.10	[40] ⁺
ϵ_8	R ₈ activation energy	1.60*	[40] ⁺
		1.21 [†]	[23]

Table 4.9: (continued from Table 4.8) *Reaction rate energetics. Plot estimate values noted with an asterisk (*). In the instance of multiple values for a parameter, the value used in the dynamic growth model is noted with a dagger (†). Alumina homodeposition studies are noted with a plus sign (+), otherwise all other studies correspond to alumina heterodeposition onto Si-OH substrates.*

Parameter	Description	Value (eV)	Source
ϵ_{10}	R ₁₀ adsorption energy	-1.20	[40] ⁺
ϵ_{11}	R ₁₁ dissociation energy	-0.40	[40] ⁺
ϵ_{12}	R ₁₂ activation energy	0.50* to 0.70*†	[40] ⁺
ϵ_{14}	R ₁₄ adsorption energy	-1.04†	[113] ⁺
		-0.85	[55]
		-0.57	[162] ⁺
ϵ_{15}	R ₁₄ activation energy	0.95†	[113] ⁺
		0.81	[146] ⁺
		0.70	[162] ⁺
		0.63	[55]
ϵ_{17}	R ₁₇ adsorption energy	-1.09†	[113] ⁺
		-1.00	[55]
		-0.75	[23]
		-0.74	[162] ⁺
ϵ_{18}	R ₁₈ activation energy	1.06	[23]
		0.93†	[113] ⁺
		0.91	[162] ⁺
		0.80	[55]
ϵ_{20}	R ₂₀ activation energy	0.33	[23]
ϵ_{22}	R ₂₂ adsorption energy	-1.01	[60, 61] ⁺
ϵ_{23}	R ₂₃ (1-2) activation energy	0.29†	[60, 61] ⁺
	(1-4) activation energy	0.095	[60, 61] ⁺
ϵ_{25}	R ₂₅ binding energy	-0.65	[111]
ϵ_{26}	R ₂₆ activation energy	0.66	[111]

Table 4.10: Partition function ratios and underlying assumptions. Parenthetical terms in the ΔZ columns designate degrees of freedom assumed to be lost due to the forward reaction. Terms in the ΔZ columns which are not in parentheses designate degrees of freedom assumed to be gained.

Reaction	Equilibrium constant or reaction rate	ΔZ_{trans}	ΔZ_{rot}	ΔZ_{vib}
R₁	$K_1 = \frac{Z_{AX}}{(Z_A/V) Z_{X'}} e^{(-\epsilon_1/k_B T)}$	$(l_{x,A}, l_{y,A}, l_{z,A})$	$(I_{x,A}, I_{y,A})$	$I_{AX} \quad \nu_{AIO}$
R₂	$K_2 = \frac{Z_{(AX)^\ddagger}}{Z_{AX}} e^{(-\epsilon_2/k_B T)}$		$(I_{z,A}, I_{Me})$	
R₃	$v_3 = \frac{k_B T}{h} \frac{Z_{(AX)^\ddagger}}{k_B T + \frac{Z_{(AX)^\ddagger}}{(Z_A/V) Z_{X'}}} e^{[-(\epsilon_1 + \epsilon_2)/k_B T]} \frac{P_A[X']}{\frac{Z_{AX}}{(Z_A/V) Z_{X'}} e^{(-\epsilon_1/k_B T)} P_A}$	-	-	-
R₄	$K_4 = \frac{Z_{Me_2X}}{Z_{Me_2} Z_{X'} [\hat{X}]} e^{(-\epsilon_4/k_B T)}$		$(I_{x,A})$	ν_{AIO}
R₅	$K_5 = \frac{Z_{(Me_2X)^\ddagger}}{Z_{Me_2X}} e^{(-\epsilon_5/k_B T)}$		(I_{Me})	
R₆	$v_6 = \frac{k_B T}{h} \frac{Z_{(Me_2X)^\ddagger}}{Z_{Me_2X}} e^{(-\epsilon_5/k_B T)} [\text{Me}_2] \theta_X$	-	-	-
R₇	$K_7 = \frac{Z_{Me_1X}}{Z_{Me_1} Z_{X'} [\hat{X}]} e^{(-\epsilon_7/k_B T)}$			ν_{AIO}
R₈	$K_8 = \frac{Z_{(Me_1X)^\ddagger}}{Z_{Me_1X}} e^{(-\epsilon_8/k_B T)}$		(I_{Me})	
R₉	$v_9 = \frac{k_B T}{h} \frac{Z_{(Me_1X)^\ddagger}}{Z_{Me_1X}} e^{(-\epsilon_8/k_B T)} [\text{Me}_1] \theta_X$	-	-	-

Table 4.11: (continued from Table 4.10) Partition function ratios and underlying assumptions. Parenthetical terms in the $\Delta\mathcal{Z}$ columns designate degrees of freedom assumed to be lost due to the forward reaction. Terms in the $\Delta\mathcal{Z}$ columns which are not in parentheses designate degrees of freedom assumed to be gained.

Reaction	Equilibrium constant or reaction rate	$\Delta\mathcal{Z}_{trans}$	$\Delta\mathcal{Z}_{rot}$	$\Delta\mathcal{Z}_{vib}$
\mathbf{R}_{10}	$K_{10} = \frac{\mathcal{Z}_{AO}}{(\mathcal{Z}_A/V)\mathcal{Z}_{O'}} e^{(-\epsilon_{10}/k_B T)}$	$(l_{x,A}, l_{y,A}, l_{z,A})$	$(I_{x,A}, I_{y,A})$	ν_{AIO}
\mathbf{R}_{11}	$K_{11} = \frac{\mathcal{Z}_{Me'_2}\mathcal{Z}_{Me_1}}{\mathcal{Z}_{AO}\mathcal{Z}_S} e^{(-\epsilon_{11}/k_B T)}$		$(l_{z,A})$	$I_{Me'_2}$
\mathbf{R}_{12}	$K_{12} = \frac{\mathcal{Z}_{(Me'_2S)^\ddagger}}{\mathcal{Z}_{Me'_2}\mathcal{Z}_S[\hat{S}]} e^{(-\epsilon_{12}/k_B T)}$		$(I_{Me'_2}, I_{Me})$	
\mathbf{R}_{13}	$v_{13} = \frac{k_B T}{h} \frac{\mathcal{Z}_{(Me'_2S)^\ddagger}\mathcal{Z}_{Me_1}}{(\mathcal{Z}_A/V)\mathcal{Z}_{O'}(\mathcal{Z}_S)^2[\hat{S}][Me_1]} \frac{[S]^2}{e^{[-(\epsilon_{10} + \epsilon_{11} + \epsilon_{12})/k_B T]}} \frac{P_A[O']}{k_B T + \frac{\mathcal{Z}_{AO}}{(\mathcal{Z}_A/V)\mathcal{Z}_{O'}} e^{(-\epsilon_{10}/k_B T)} P_A}$	-	-	-

Table 4.12: (continued from Table 4.11) Partition function ratios and underlying assumptions. Parenthetical terms in the $\Delta\mathcal{Z}$ columns designate degrees of freedom assumed to be lost due to the forward reaction. Terms in the $\Delta\mathcal{Z}$ columns which are not in parentheses designate degrees of freedom assumed to be gained.

Reaction	Equilibrium constant or reaction rate	$\Delta\mathcal{Z}_{trans}$	$\Delta\mathcal{Z}_{rot}$	$\Delta\mathcal{Z}_{vib}$
R₁₄	$K_{14} = \frac{\mathcal{Z}_{BMe_2}}{(\mathcal{Z}_B/V)\mathcal{Z}_{Me_2}} e^{(-\epsilon_{14}/k_B T)}$	$(I_{x,B}, I_{y,B}, I_{z,B})$	$(I_{x,B}, I_{y,B})$	$I_{BMe_2} \quad \nu_{AIO}$
R₁₅	$K_{15} = \frac{\mathcal{Z}_{(BMe_2)^\ddagger}}{\mathcal{Z}_{BMe_2}} e^{(-\epsilon_{15}/k_B T)}$		$(I_{z,B}, I_{Me})$	
R₁₆	$v_{16} = \frac{k_B T}{h} \frac{\mathcal{Z}_{(BMe_2)^\ddagger}}{k_B T + \frac{\mathcal{Z}_{BMe_2}}{(\mathcal{Z}_B/V)\mathcal{Z}_{Me_2}} [-(\epsilon_{14} + \epsilon_{15})/k_B T]} e^{(-\epsilon_{14}/k_B T)} P_B$		-	-
R₁₇	$K_{17} = \frac{\mathcal{Z}_{BMe_1}}{(\mathcal{Z}_B/V)\mathcal{Z}_{Me_1}} e^{(-\epsilon_{17}/k_B T)}$	$(I_{x,B}, I_{y,B}, I_{z,B})$	$(I_{x,B}, I_{y,B})$	$I_{BMe_1} \quad \nu_{AIO}$
R₁₈	$K_{18} = \frac{\mathcal{Z}_{(BMe_1)^\ddagger}}{\mathcal{Z}_{BMe_1}} e^{(-\epsilon_{18}/k_B T)}$		$(I_{z,B}, I_{Me})$	
R₁₉	$v_{19} = \frac{k_B T}{h} \frac{\mathcal{Z}_{(BMe_1)^\ddagger}}{k_B T + \frac{\mathcal{Z}_{BMe_1}}{(\mathcal{Z}_B/V)\mathcal{Z}_{Me_1}} [-(\epsilon_{17} + \epsilon_{18})/k_B T]} e^{(-\epsilon_{17}/k_B T)} P_B$		-	-

Table 4.13: (continued from Table 4.12) Partition function ratios and underlying assumptions. Parenthetical terms in the $\Delta\mathcal{Z}$ columns designate degrees of freedom assumed to be lost due to the forward reaction. Terms in the $\Delta\mathcal{Z}$ columns which are not in parentheses designate degrees of freedom assumed to be gained.

Reaction	Equilibrium constant or reaction rate	$\Delta\mathcal{Z}_{\text{trans}}$	$\Delta\mathcal{Z}_{\text{rot}}$	$\Delta\mathcal{Z}_{\text{vib}}$
\mathbf{R}_{20}	$K_{20} = \frac{\mathcal{Z}_{(B(Me_1)_2)^\ddagger}}{\mathcal{Z}_{BMe_1} \mathcal{Z}_{Me_1}} e^{(-\epsilon_{20}/k_B T)}$		$(I_{z,B}, I_{Me}, I_{BMe_1})$	
\mathbf{R}_{21}	$v_{21} = \frac{k_B T}{h} \frac{\mathcal{Z}_{(B(Me_1)_2)^\ddagger}}{(\mathcal{Z}_B/V)(\mathcal{Z}_{Me_1})^2 [\widehat{Me}]} e^{[-(\epsilon_{17} + \epsilon_{20})/k_B T]} \frac{P_B [Me_1]^2}{k_B T + \frac{\mathcal{Z}_{BMe_1}}{(\mathcal{Z}_B/V) \mathcal{Z}_{Me_1}} e^{(-\epsilon_{17}/k_B T)}}$	-	-	-

Table 4.14: (continued from Table 4.13) Partition function ratios and underlying assumptions. Parenthetical terms in the ΔZ columns designate degrees of freedom assumed to be lost due to the forward reaction. Terms in the ΔZ columns which are not in parentheses designate degrees of freedom assumed to be gained.

Reaction	Equilibrium constant or reaction rate	ΔZ_{trans}	ΔZ_{rot}	ΔZ_{vib}
R₂₂	$K_{22} = \frac{Z_{BS}}{(Z_B/V) Z_S} e^{(-\epsilon_{22}/k_B T)}$	$(I_{x,B}, I_{y,B}, I_{z,B})$	$(I_{x,B}, I_{y,B})$	ν_{AIO}
R₂₃	$K_{23} = \frac{Z_{(BSO)^\ddagger}}{Z_{BS} Z_{O'} [\hat{O}]} e^{(-\epsilon_{23}/k_B T)}$		$(I_{z,B})$	
R₂₄	$v_{24} = \frac{k_B T}{h} \frac{Z_{(BSO)^\ddagger} [\hat{O}']}{k_B T (Z_B/V) Z_S Z_{O'} [\hat{O}]} e^{[-(\epsilon_{22} + \epsilon_{23})/k_B T]} \frac{P_B[S]}{Z_{BS} Z_{O'} [\hat{O}]} e^{(-\epsilon_{22}/k_B T)} P_B$	-	-	-
R₂₅	$K_{25} = \frac{Z_{AB}}{(Z_A/V) Z_B} e^{(-\epsilon_{25}/k_B T)}$	$(I_{x,A}, I_{y,A}, I_{z,A})$ $(I_{x,B}, I_{y,B}, I_{z,B})$ $I_{x,AB}, I_{y,AB}, I_{z,AB}$	$(I_{x,A}, I_{y,A})$ $(I_{x,B}, I_{y,B})$ $I_{x,AB}, I_{y,AB}, I_{z,AB}$	ν_{AIO}
R₂₆	$K_{26} = \frac{Z_{(AB)^\ddagger}}{Z_{AB}} e^{(-\epsilon_{26}/k_B T)}$		(I_{Me})	
R₂₇	$v_{27} = \frac{k_B T}{h} \frac{Z_{(AB)^\ddagger}}{(Z_A/V) Z_B} e^{[-(\epsilon_{25} + \epsilon_{26})/k_B T]} \frac{P_A P_B}{(k_B T)^2}$	-	-	-

4.1.1 TMA Reactions on Hydroxylated Alumina

The TMA half-cycle is typically initiated by barrierless chemisorption of TMA (R_1), forming a coordinative bond with the oxygen of a surface hydroxyl group. While the adsorbed TMA has no translational freedom, it maintains a “helicopter” rotational mode and the combined angular momentum of the adduct. This stable adduct may then proceed through a 4-coordinate Al transition state to produce the DMA moiety and methane gas which immediately desorbs (R_2 , R_3). The primary entropic difference between the adsorbed TMA and transition state is the loss of internal rotational freedom of one Me group due to bond formation. The trigonal planar 3-coordinate Al of the DMA that remains after the reaction is denoted by Me'_2 .

This Me'_2 is then assumed to undergo immediate densification with a surface OH, recovering the 4-coordinate Al state Me_2 (R_4). The primary distinction between the two is the helicopter rotation mode of Me'_2 that does not exist for Me_2 : the contribution of this rotation mode is approximately equivalent to rotation about the Al-Me bond (with rotational inertia $I_{Me'_2} = \sqrt{3}r_{Al-C}^2 m_{Me}$) for gas-phase TMA. For typical operating conditions, $K_4 \approx \mathcal{O}(10^5)$ indicating the favorability of finding the relaxed Me_2 species relative to Me'_2 . Thus, if surface hydroxyl groups are present, reaction (R_3) will produce Me_2 , not Me'_2 .

Each of the two surface Me groups left after reaction (R_4) can undergo subsequent reactions with a surface OH site, producing methane that immediately desorbs to the gas phase. The 4-coordinate Me_2 can undergo a reaction where H from

a neighboring OH site is transferred to a Me group on the 4-coordinated Al to eliminate another methane molecule in reactions (R₅) and (R₆). As in the previous methane elimination, the trigonal Me'₁ can immediately relax to form Me₁, which caps two surface O and one hydroxyl group X, through reaction (R₇) with $K_7 \approx \mathcal{O}(10^{13})$. As can be readily seen by the large energy associated with the reorganization [40] listed in Table 4.8, the Me₁ species is highly favored over Me'₁ as the result of reaction (R₆). Following this sequence, the final Me group can then be eliminated by reactions (R₈) and (R₉), leaving a bare surface aluminum.

4.1.2 TMA Reactions on Bare Alumina

Having considered the adsorption and methane-elimination reactions on a hydroxylated surface, the adsorption and dissociation reactions of TMA on *locally* bare (*i.e.* dehydroxylated) alumina will be described by reaction sequence (R₁₀-R₁₃). Of course no methane is produced in any of the reaction steps because of the lack of surface H. In reaction (R₁₀), TMA adsorbs barrierlessly at a bridged oxygen site O', forming a Lewis acid-base adduct similar to the mechanism of (R₁). However, in this case, the adduct is considered unstable (in an energetic sense with $\epsilon_{11} < 0$) and so can undergo a barrierless dissociation reaction, forming Me'₂ and Me₁ surface species (R₁₁).

Depending on the proximity of more aluminum sites, this process may be repeated. The Me'₂ moiety may further dissociate onto a neighboring aluminum, although this does require an activation energy and consequently formation of a transition state (R₁₂). The energetics for this transition state, however, have only

been estimated [40]. The final product of the reaction sequence is a completely dissociated TMA molecule, distributed about the surface as three MMA groups with a 3- or 4-coordinate aluminum (R_{13}).

4.1.3 Water Reactions on Methylated Alumina

The water half-cycle is typically initiated by barrierless chemisorption of water (R_{14}), forming a coordinative bond with a surface aluminum. While the adsorbed water has no translational freedom, it maintains a “helicopter” rotational mode and the combined angular momentum of the adduct. Because of the highly-favored densification reactions of the TMA half-cycle, the surface aluminum onto which water adsorbs is likely to be 4-coordinate. Thus, one of the shared Al-O bonds of the adsorption site may be released in interaction with an incoming water molecule [23]. In this way, the aluminum atom maintains the 4-coordinate state.

In the case that the aluminum involved in the stable adduct contains two methyl ligands, then the adduct may proceed through a 1-2 H transfer transition state to produce a surface hydroxyl group X, a Me'_1 moiety, and methane gas which immediately desorbs (R_{15} , R_{16}). The primary entropic difference between the adsorbed water and transition state is the loss of internal rotational freedom of one Me group due to bond formation. As in the TMA half-cycle reactions, Me'_1 undergoes a barrierless and immediate densification, recovering the 4-coordinate Al state Me_1 [23]. Specific energetics have not been reported for this densification step. Thus, it has not been explicitly modeled in this work.

Water may also adsorb onto a surface aluminum which contains only one

methyl ligand (R_{17}). This adsorption reaction is relatively the same as with the dimethyl aluminum reaction, but with slightly different energetics. The adduct proceeds through a 1-2 H transfer transition state (R_{18}) and adds a surface hydroxyl group while releasing methane to the gas phase (R_{19}). This product is also assumed to immediately proceed to densification.

As an alternative to the 1-2 H transfer reaction, a 1-4 H transfer mechanism has been suggested in [23] whereby the BMe_1 adduct interacts with a neighboring Me_1 to yield a more complex transition state (R_{20}). From this transition state, a methane molecule is formed with the methyl group of a neighboring aluminum as opposed to the aluminum atom onto which the water molecule originally adsorbed. Thus, several rotational modes are lost—helicopter rotation of the water molecule, an internal methyl group rotation, and the BMe_1 rotational inertia. The forward reaction releases the methane, forming a bridged hydroxyl group between the two aluminum atoms (R_{21}). This 1-4 H transfer was reported to be several orders more favored (energetically) than the 1-2 H transfer mechanism.

4.1.4 Water Reactions on Bare Alumina

Having considered the adsorption and methane elimination reactions on a methylated surface, the adsorption and dissociation reactions of water on *locally* bare (*i.e.* demethylated) alumina will be described by reaction sequence (R_{22} - R_{24}). As in the TMA dissociative adsorption reactions, no methane is produced in any of the reaction steps. In reaction (R_{22}), water adsorbs barrierlessly onto a bare aluminum atom, forming a Lewis acid-base adduct similar to the mechanism on a

methylated surface. Except for the absence of an adduct rotational moment, this adsorbed water molecule is entropically identical to the molecularly adsorbed water onto a methylated surface.

Given the availability of an undercoordinated oxygen atom, the adduct may proceed through a transition state, transferring a hydrogen to this atom and resulting in the loss of the helicopter rotational mode. While this reaction is not barrierless, the activation energy to form the transition state (R_{23}) is relatively low. Although, the 1-4 H transfer path is reported to be more energetically favored when compared to the the 1-2 H transfer path [60,61], consistent with the findings of [23] for the methylated surface. Nonetheless, the adduct ultimately proceeds through this transition state, resulting in the formation of two surface hydroxyl groups (R_{24}).

4.1.5 Gas-phase Side Reactions

While gas-phase reactions are certainly non-ideal in ALD, a sequence of elementary gas-phase side reactions have been included in the ALD kinetics model to account for CVD-like reactions that may occur in the case of insufficient purge periods, *i.e.* when TMA and water precursors coexist in the reaction chamber [111]. This sequence begins when a TMA and water molecule collide to barrierlessly form a stable gas-phase Lewis acid-base adduct (R_{25}). The translational freedom of the separate molecules is replaced by the three translational degrees of freedom associated with the adduct. Likewise, the rotational modes of the adduct replace the rotational modes of the separate molecules. Internal rotation in the axial direction remains, however, for each molecule in the adduct. All vibrational modes are

assumed to be retained and an additional mode arises from the Al-O bond.

This adduct may proceed to form a transition state in preparation for methane elimination. The primary entropic difference between the adduct and transition state is the loss of internal rotational freedom of one Me group due to bond formation (R_{26}). The product of the forward reaction is a methane molecule and $\text{Al}(\text{CH}_3)_2\text{-OH}$ (DMA-OH) which is noted as “D” in the model formulation developed herein (R_{27}). No additional gas-phase or surface reactions involving this species are considered beyond this point. This species, however, is a known product of ALD side reactions and serves as a way to account for the relative significance of gas-phase side-reactions in a dynamic ALD kinetics model. Predictions of significant DMA-OH formation would, for instance, suggest the need for longer purge periods and/or decreased precursor exposures.

4.2 Analysis of Reaction Mechanism

Several researchers have investigated the alumina ALD surface reaction mechanism using quantum-chemical computational methods and have reported values for the energetics of relevant elementary reaction steps. These values are given in Tables 4.8 and 4.9. Of these studies, four investigate alumina homodeposition [40, 113, 146, 162], two are alumina water adsorption studies [60, 61], and the others are alumina heterodeposition studies on Si-OH substrates. Values are not considered for heterodeposition on other substrates (*e.g.* Si-H, Ge-S, TiO_2 etc.), although the general mechanism is fairly similar [23, 54, 56, 57, 83, 91, 99, 100, 113, 139, 155, 167, 168, 173].

In some instances, the suggested reaction energies and/or reaction mechanisms vary widely across different studies of the alumina ALD process. Considering that energetics are exponential terms in reaction rate formulations, wide variations in these values will produce wide variations in the reaction rates produced. In one instance, for different H transfer paths, the difference in the computed rate is $\mathcal{O}(10^6)$ [23], but this is also seen in reported values for the typical 1-2 H transfer mechanism. To resolve these differences with a kinetic analysis and choose a set of energetic parameters most consistent with the observed ALD mechanism is thus the objective of this section.

4.2.1 Comparative Analysis of TMA Kinetics

Having derived v_3 , v_6 , v_9 , and v_{13} the values of these rate expressions are plotted as a function of TMA partial pressure for $T = 450$ K. To compare the energetics suggested for pressure-dependent TMA half-cycle reactions vs. pressure-independent reactions, the rate expressions for molecular adsorption and ligand-exchange v_3 have been plotted with dissociative adsorption v_{13} in Fig. 4.1. The rates of the subsequent surface methane-elimination reactions v_6 and v_9 are likewise shown together in Fig. 4.2. Note that these values are not rate constants as they depend on P_A , $[X]$, $[X']$, $[O']$, $[S]$, $[Me_1]$, and $[Me_2]$; for the figures, rates are evaluated at the maximum surface concentration of these species, *e.g.*, $[X] = [\hat{X}]$. For this reason and because the modulating effect of surface Me group coverage has not yet been included, the rates portrayed *correspond to the upper limits of the surface reaction rates.*

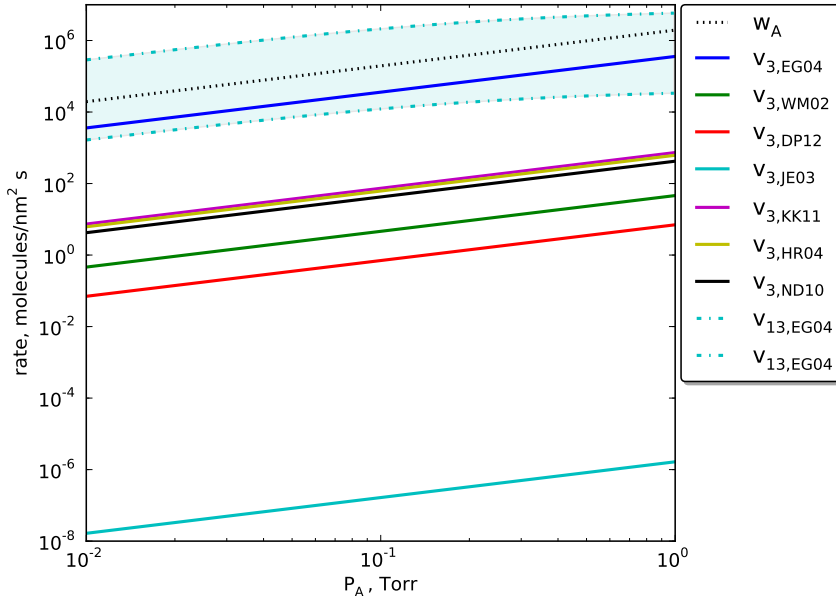


Figure 4.1: Representative reaction rates of irreversible TMA half-cycle reactions corresponding to pressure-dependent reactions at $T = 450$ K and maximum surface concentration values for $[X]$, $[X']$, $[O]$, $[S]$, $[Me_1]$, and $[Me_2]$. For reference, the TMA wall collision rate w_A also is shown. Data labels denote the source of energetic information used in the rate computation; e.g. EG04 corresponds to ElliottGreer2004 (first author, last author, and year of publication).

Because v_3 and v_{13} depend on the adsorption of the gas-phase precursor A, their values are expected to increase with P_A while v_6 and v_9 are independent of P_A . The dissociative adsorption rate v_{13} approaches a limiting value as P_A grows, indicating saturation in the Langmuir equilibrium relation; an important consequence is that the adsorbed adduct can subsequently desorb during the purge phase between exposures A and B, reducing the effectiveness of the overall deposition process.

For reference, the TMA wall collision rate is plotted as $w_A = P_A / \sqrt{2\pi m_A k_B T}$. For the lower end of the ϵ_{13} range (*i.e.* the upper limit for v_{13} shown in the plot), $v_{13} > w_A$ indicating the system is not in equilibrium with the gas-phase TMA at P_A . An additional gas-phase transport term would have to be included to sustain these rates, otherwise this corresponds to a mass-transfer limited situation.

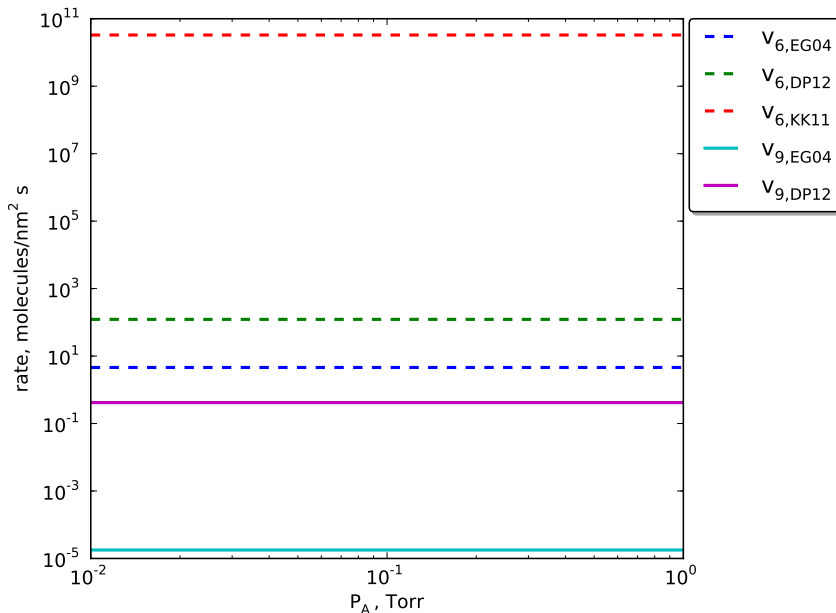


Figure 4.2: *Representative reaction rates of irreversible TMA half-cycle reactions corresponding to pressure-independent reactions at $T = 450$ K and maximum surface concentration values for $[X]$, $[X']$, $[O]$, $[S]$, $[Me_1]$, and $[Me_2]$. Data labels denote the source of energetic information used in the rate computation; e.g. EG04 corresponds to ElliottGreer2004 (first author, last author, and year of publication).*

The energetics associated with each elementary reaction step have been extracted from quantum-chemical computational studies. As can be seen from Tables 4.8 and 4.9, in many instances, very different values have been reported. In these cases, reaction rates were computed based on each source and noted in the figures. For example, $v_{3,EG04}$ corresponds to a rate for reaction (R₃) computed using an (R₁) adsorption and (R₂) activation energy from [40] which has been noted ElliottGreer2004 (first author, last author, year of publication).

4.2.1.1 Resolution of Thermodynamics

When considering the thermodynamics reported in this collection of DFT studies, it is important to choose values which are consistent with what is known about

the ALD mechanism. In some instances, reaction rates are several orders larger or smaller than the general trend of quantum-chemical computations. For instance, in EG04 [40], the estimated activation energy for ϵ_2 is significantly lower than other reported values and thus these energetics yield reaction rates for (R_3) which are several orders larger when compared to other predictions. On the other end of the spectrum, JE03 [74] reports a barrier more than double than what has been suggested in other studies. The corresponding rate for (R_3) based on those energetics is thus significantly lower.

Note that in some instances the reported adsorption energy may be relatively consistent with other studies, but the ligand-exchange activation energy may not agree, or vice versa. Because the initial adsorption and transition state formation reaction are inherently pressure-dependent, the forward rate also has this dependency. Thus, to maintain consistency in rate computations, both energy values are taken from the same source, *i.e.* adsorption energy from one source will not be combined with the ligand-exchange activation energy of another.

The energetics of WM02 [162] and ND10 [113] were both taken from homodeposition studies and are in fair agreement with one another. They, however, yield slightly different reaction rates. Thermodynamics from the heterodeposition studies of KK11 [80] and HR04 [55] also yield a range of (R_3) rate predictions which appear to be consistent with other reports.

To knowledge, there has been only one quantum-chemical computational study reporting ALD energetics for dissociative TMA adsorption on a bare alumina surface [40]. The energetics for the (R_{10} - R_{13}) reaction sequence thus are taken solely

from this study. It is interesting to note that the rate of the dissociative TMA reaction is significantly higher than the comparable rate of reaction on a hydroxylated surface. Because there are no other reported values with which to compare the thermodynamics of this reaction, the consistency of $\epsilon_{10} - \epsilon_{12}$ with respect to other reports cannot be discussed. It must also be noted that the transition state was not able to be computed for the dissociative adsorption reaction and thus ϵ_{12} is an estimate. A range is therefore shown for $v_{13,EG04}$.

Moving now to the pressure-independent reactions, one will notice that there have been notably fewer quantum-chemical computational studies devoted to the subsequent surface reactions following adsorption and ligand exchange. KK11 [80] reports a very small activation energy barrier ϵ_5 yielding a very high reaction rate which is clearly in disagreement with other reports. The homodeposition study of EG04 [40] suggests an activation energy barrier for the second methane-elimination reaction which yields a lower (R_6) rate than what has been reported in the heterodeposition study of DP12 [23]. Substrate effects may account for this difference. In the final methane-elimination reaction (R_9), EG04 was unable to locate a transition state and thus only an estimate was given for the activation barrier. In this instance, energetics from DP12 may be used as an alternative.

4.2.2 Comparative Analysis of Water Kinetics

Having likewise derived v_{16} , v_{19} , v_{21} , and v_{24} , the values of these rate expressions are plotted as a function of water partial pressure for $T = 450$ K and are collectively shown in Fig. 4.3. Again, note that these values are not rate constants

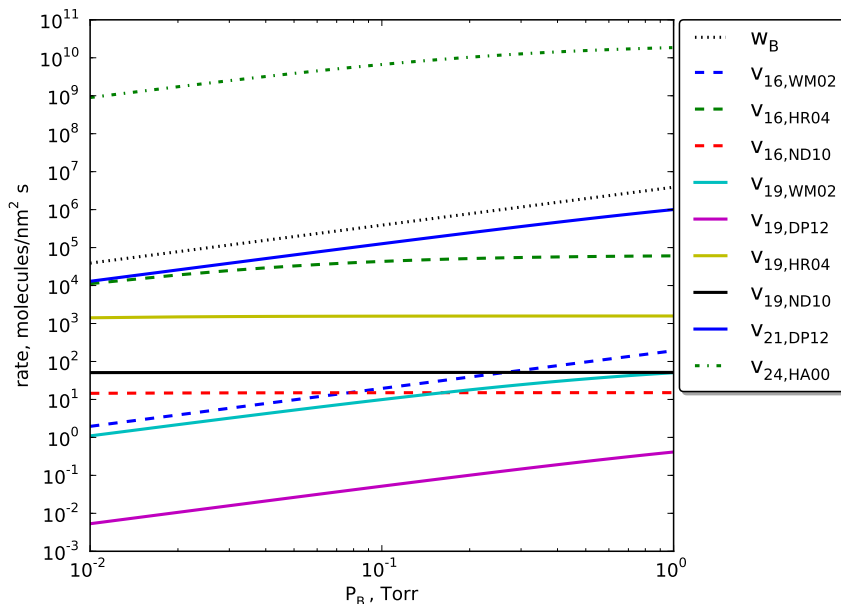


Figure 4.3: Representative reaction rates of irreversible water half-cycle reactions corresponding to pressure-dependent reactions at $T = 450$ K and maximum surface concentration values for $[X]$, $[X']$, $[O']$, $[S]$, $[Me_1]$, and $[Me_2]$. For reference, the water wall collision rate w_B also is shown. Data labels denote the source of energetic information used in the rate computation; e.g. WM02 corresponds to WidjajaMusgrave2002 (first author, last author, and year of publication).

as they depend on P_B , $[X]$, $[X']$, $[O']$, $[S]$, $[Me_1]$, and $[Me_2]$; for this figure, rates are evaluated at the maximum surface concentration of these species, e.g., $[X] = [\hat{X}]$. For this reason and because the modulating effect of surface hydroxyl group coverage has not yet been included, the rates portrayed correspond to the upper limits of the surface reaction rates.

Because all water half-cycle rates depend on the adsorption of the gas-phase precursor B, their values are expected to increase with P_B . Both the dissociative adsorption rate v_{24} and the MMA reaction rate v_{19} approach a limiting value as P_B grows, indicating saturation in the Langmuir equilibrium relation. For reference, the water wall collision rate is plotted as $w_B = P_B/\sqrt{2\pi m_B k_B T}$. Similar to the

TMA dissociative adsorption reaction, $v_{24} \gg w_B$ indicating a mass-transfer limited situation.

4.2.2.1 Resolution of Thermodynamics

The water adsorption and ligand-exchange activation energies associated with reaction sequence (R₁₄-R₁₆) have been reported in two homodeposition studies, WM02 [162] and ND10 [113] and one heterodeposition study HR04 [55]. The rate computed from HR04 involves a stronger adsorption interaction and lower ligand-exchange barrier and is consequently several orders higher. Considering this, the thermodynamics derived from homodeposition will be considered.

The water adsorption and ligand-exchange activation energies associated with reaction sequence (R₁₇-R₁₉) have been reported in the above cited studies and in an additional heterodeposition study DP12 [23]. However, energetics from the heterodeposition studies yield reaction rates significantly higher and lower than those reported for the homodeposition studies. Specifically, an alternative 1-4 H transfer path has been suggested with reaction energies yielding rates $v_{21,DP12}$ that are several orders faster than the typical 1-2 H transfer mechanism $v_{19,DP12}$ suggested in the same study. The 1-4 H transfer path is also much faster than reaction rate prediction of all other cited studies based on molecular water adsorption. Note that the predictions of this study are based on alumina deposition onto a Si-OH substrate. Thus, substrate effects may account for the differences in reported energetics when compared to alumina homodeposition results. It is thus unclear if this mechanism is applicable to the present study.

Reaction rate predictions based on WM02 and DP12 are very different at low pressures, but are of similar order at higher pressures. This can be explained by the distinct differences in the adsorption and reaction energies reported. The suggested adsorption energy of ND10 is nearly double that of WM02, but the reaction activation energy is significantly higher. The adsorption energies reported in ND10 [113] and HR04 [55] are relatively high, yielding rates which appear to be independent of pressure, indicating an almost immediate surface saturation.

Two quantum-chemical computational studies are widely referenced in the context of water interactions with bare alumina [60,61]. The energetics for the dissociative water reaction sequence (R₂₂-R₂₄) are taken solely from these studies. As with the TMA dissociative adsorption reactions, it is interesting to note that the rate of the dissociative water reaction is several orders higher than the comparable rate of reaction on a methylated surface. It must be noted that while these studies have been referenced in other ALD works [23], the energetics may not correspond to the amorphous alumina film grown by ALD. The reported energetics correspond to α -alumina which has a significantly higher density ($\rho_\alpha = 3.98 \text{ g/cm}^3$) compared to the amorphous phase deposited during ALD ($\rho_{am} = 3.3 \text{ g/cm}^3$) [53]. It is therefore uncertain whether these thermodynamics are applicable to the alumina ALD process.

4.2.3 Gas-phase Side Reaction Mechanism Analysis

Representative rates for the gas-phase side-reaction are shown in Fig. 4.4. In the top plot, the partial pressure of one precursor is kept constant at 0.01 Torr

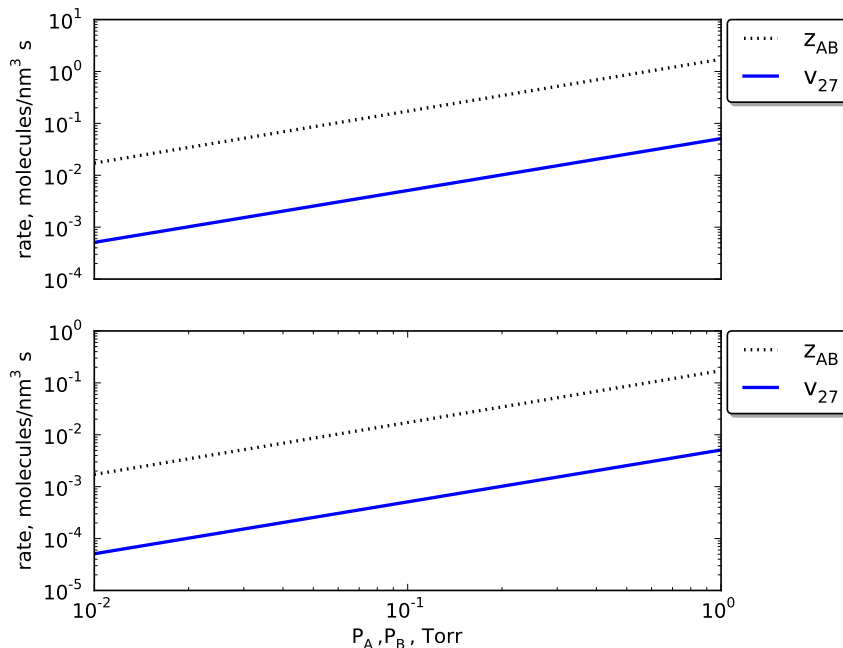


Figure 4.4: *Representative reaction rate of the gas-phase side reaction. (top) Rate computed with one precursor at constant partial pressure of 0.01 Torr. (bottom) Rate computed with one precursor at constant partial pressure of 0.001 Torr. All rates correspond to reactions at $T = 450$ K. For reference, the gas-phase TMA-water collision frequency z_{AB} also is shown.*

while the other is varied, *i.e.* $P_A = 0.01$ Torr. The bottom plot corresponds to a precursor partial pressure of 0.001 Torr for one precursor while the other is varied, *i.e.* $P_A = 0.001$ Torr. This is meant to mimic residual precursor gases in the reaction chamber following a purge period. The rate obviously increases with pressure and could become significant without proper separation of the pulsing intervals.

4.3 Thermodynamic Sensitivity

It is very important to note the sensitivity of computed reaction rate expressions to the thermodynamics used in the computations. Because reaction energies are placed inside an exponential term, small variations in these values could result

in significant variations in computed kinetics. As previously stated, energetics for the models derived in this thesis have been adopted from reported thermodynamics of quantum-chemical computational studies. As demonstrated in Figs. 4.1-4.3, reaction energetics can cause significant differences in computed kinetics, with magnitude differences of several orders for the same reaction. These discrepancies may be attributed to differences in the level of theory used in the various DFT studies and also by current computational challenges posed by atomic-scale simulations.

In DFT, electronic structures of chemically-reacting species are determined by approximately solving the quantum mechanical Schrödinger wave equation, which gives access to atomic structures, reaction energetics at zero temperature, and dynamics at finite temperatures. However, ALD chemistries are often very complex and there still exist issues relating to the accuracy of DFT models such that computing Gibbs free energies of activation to “chemical accuracy” (< 5 kJ/mol) remains a difficulty in *ab initio* simulations [38]. For this reason, a detailed survey of reported *ab initio* energetics was performed herein for the alumina ALD system.

4.4 Growth Surface State Dynamics

It is generally reported that steric hinderance by surface Me groups regulates TMA surface reactions [10,40,128,129,131,161]. This conclusion is supported by observations that TMA surface reactions self-terminate when Me group concentration reaches an approximately constant value denoting saturation of adsorbed species, a value which approaches the Me group close-packing limit [10, 127, 131–135, 161].

Steric hindrance of surface Me groups appears to cause the termination of TMA reactions and so TMA adsorption proceeds until the surface becomes saturated with Me groups which can shield active bonding sites. For these reasons, it is important to include in an alumina ALD growth model an account of surface Me group concentration.

Total concentration $[\text{Me}]$ of surface Me groups is found to be a combination of chemisorbed Me_1 and Me_2 plus the Me groups of adsorbed adducts AO and AX. Recalling that $\theta_{\text{Me}} = [\text{Me}]/[\hat{\text{Me}}]$ and $\phi_{\text{Me}} = 1 - \theta_{\text{Me}}$,

$$[\text{Me}] = [\text{Me}_1] + 2[\text{Me}_2] + 3([\text{AX}]^{eq} + [\text{AO}]^{eq}) \phi_{\text{Me}} \quad (4.1)$$

$$= \frac{[\text{Me}_1] + 2[\text{Me}_2] + 3([\text{AX}]^{eq} + [\text{AO}]^{eq})}{1 + 3([\text{AX}]^{eq} + [\text{AO}]^{eq})/[\hat{\text{Me}}]} \quad (4.2)$$

where the superscript eq indicates values computed using the equilibrium relationships shown in Tables 4.1 and 4.3. Likewise, $\theta_{\text{X}^{tot}} = \theta_{\text{X}} + \theta_{\text{X}'} = [\text{X}^{tot}]/[\hat{\text{X}}]$ and $\phi_{\text{X}} = 1 - \theta_{\text{X}^{tot}}$. Thus

$$[\text{X}^{tot}] = [\text{X}] + [\text{X}'] + ([\text{BMe}_2]^{eq} + [\text{BMe}_1]^{eq}) \phi_{\text{X}} \quad (4.3)$$

$$= \frac{[\text{X}] + [\text{X}'] + [\text{BMe}_2]^{eq} + [\text{BMe}_1]^{eq}}{1 + ([\text{BMe}_2]^{eq} + [\text{BMe}_1]^{eq})/[\hat{\text{X}}]} \quad (4.4)$$

With ϕ_{Me} representing the fraction of growth surface not blocked by Me groups and ϕ_{X} representing the fraction of growth surface not blocked by hydroxyl groups,

the time-rate of change of surface species Me_1 , Me_2 , and O, O', S, X, and X' are

$$\frac{d[\text{Me}_1]}{dt} = v_6 - v_9 + 3v_{13}\phi_{Me} + (v_{16} - v_{19})\phi_X \quad (4.5)$$

$$\frac{d[\text{Me}_2]}{dt} = v_3\phi_{Me} - v_6 - v_{16}\phi_X \quad (4.6)$$

$$\frac{d[\text{O}]}{dt} = v_{13}\phi_{Me} \quad (4.7)$$

$$\frac{d[\text{O}']}{dt} = (v_3 - v_{13})\phi_{Me} + v_6 + v_9 - v_{24}\phi_X \quad (4.8)$$

$$\frac{d[\text{S}]}{dt} = v_9 - 2v_{13}\phi_{Me} - v_{24}\phi_X \quad (4.9)$$

$$\frac{d[\text{X}]}{dt} = v_3\phi_{Me} - v_9 + v_{24}\phi_X \quad (4.10)$$

$$\frac{d[\text{X}']}{dt} = -2v_3\phi_{Me} - v_6 + (v_{16} + v_{19} + v_{24})\phi_X \quad (4.11)$$

subject to initial conditions $[\text{Me}_1](0)$, $[\text{Me}_2](0)$, \dots , $[\text{X}'](0)$. Thus, the evolution of the surface state can be computed by integrating Eqns. (4.5-4.11) from the specified initial conditions. Furthermore, the instantaneous adsorbed and activated-complex species concentrations can be recovered from the states defined by Eqns. (4.5-4.11) and the equilibrium relationships described earlier.

4.4.1 *Dynamic Simulation Results*

With the surface-state dynamic modeling differential and algebraic equations in hand, the evolution of the surface state can be examined over the complete ALD cycle by integrating the differential equations (4.5-4.11) subject to the initial state of the surface. For this purpose, the collocation-based technique described in the previous chapter is employed. Three representative cases are shown in Fig. 4.5

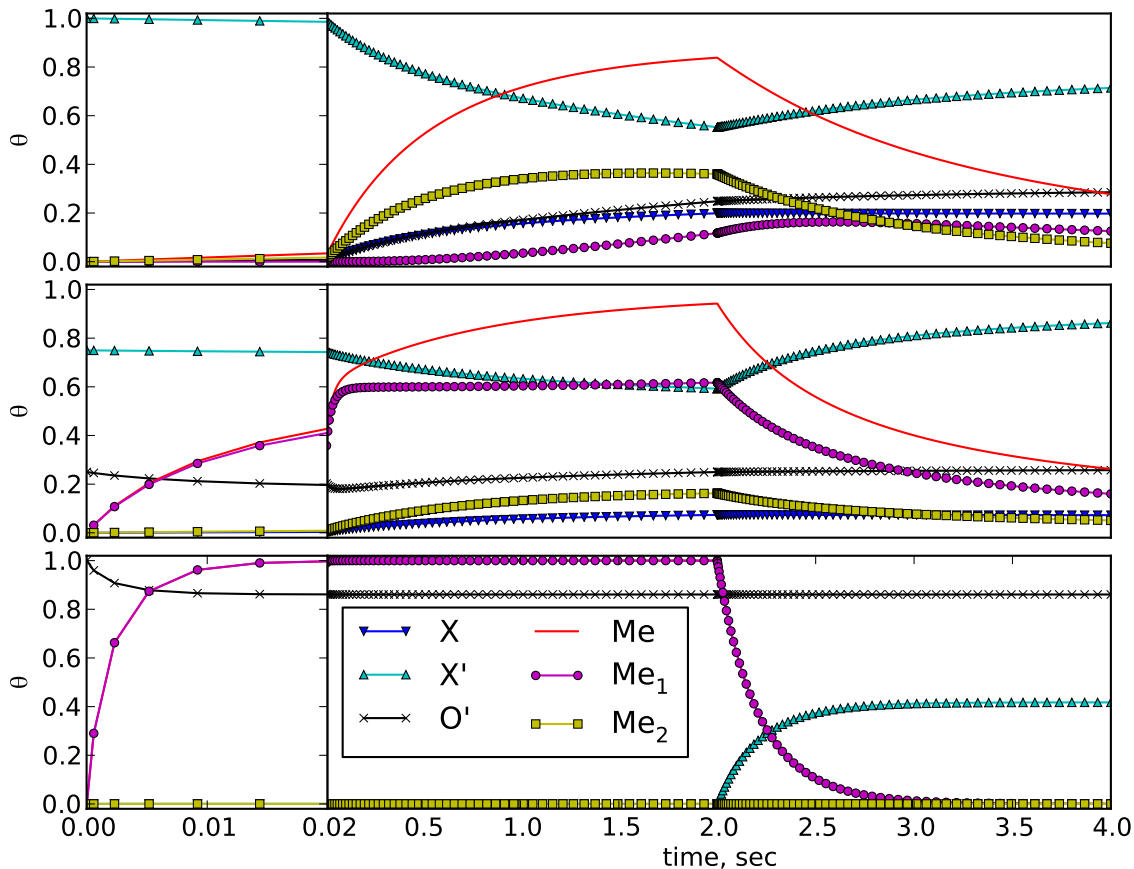


Figure 4.5: *Surface species dynamics for $\theta'_X(0) = 1$ (top), $\theta'_X(0) = 0.75$ (middle), and $\theta'_X(0) = 0$ (bottom) at $T=450$ K and $P = 2$ Pa. The initial 0.02 s of the TMA half-cycle have been emphasized to capture the fast surface reactions.*

and all correspond to an initial surface devoid of Me groups. The first simulation shown in the uppermost plot corresponds to the initial state $[X'](0) = [\hat{X}]$, a fully hydroxylated surface. Early in the simulation, $[X']$ drops quickly upon exposure to TMA, producing surface Me_2 by (R₃), some of which reacts with surface X to form Me_1 . During the subsequent water pulse, most but not all of the Me groups are consumed, but the water self-saturation limit is not reached.

A set of initial conditions at the other end of the range of $[X'](0)$ corresponds to a bare alumina surface ($[X'](0)=0$) and the resulting simulation is shown in the bottom plot of Fig. 4.5. The dynamic behavior in this situation is simple and

quick: TMA adsorbs onto the bare O' sites and proceeds through the sequence of reactions (R_{10} - R_{13}), quickly saturating the surface with Me_1 , after which, no other reactions are possible. This is completely expected as no methane-elimination reactions are possible without the presence of hydroxyl groups. What is interesting is the behavior of the process during the water pulse, when compared to the Me_1 and Me_2 terminated surface in the top plot. The dynamics of the water exposure when starting from the bare surface are significantly faster. The Me_1 groups are quickly consumed, after which the OH concentration remains constant. In the previous case, however, the Me_2 groups were more readily consumed, but when converted to Me_1 , this reduction was much slower. This demonstrates the competition between these two reactions at higher surface hydroxylation.

Intermediate between the fully hydroxylated and bare surfaces is the case $[X'](0) = 3[\hat{X}]/4$, $[O'](0) = [\hat{X}]/4$ shown in the middle plot of Fig. 4.5. Despite the significant concentration of surface OH species X' , the dynamics share more in common with those corresponding to the bare surface. As in the latter case, reaction (R_{13}) proceeds to quickly saturate the surface with Me_1 ; however, after the saturation point, reactions (R_6) and (R_9) can proceed, albeit slowly, because of the available X sites. During the water exposure, Me_1 groups are much more quickly consumed than Me_2 , which was not the case for the surface with higher hydroxylation. Together, these results suggest that reaction (R_{19}) may dominate at lower hydroxyl group coverage, perhaps due to the greater availability of Me_1 groups under those conditions. But reaction (R_{16}) becomes more competitive at higher hydroxyl group coverage when Me_2 is more readily available.

Another implication of these results stem from the inability of the water reactions to remove all Me groups and thus produce a saturated surface under the conditions considered in the model. While the TMA dynamics also do not completely saturate, the saturation limit is approached much more quickly than in the water half-cycle. This would suggest that the water exposure should be higher than that of the TMA in order to ensure self-limiting growth conditions. This is consistent with previous modeling [156] as well as experimental observations requiring higher water exposures (relative to TMA) to sufficiently remove all methyl ligands [75,102]. Note that dissociative water reactions were not allowed in the dynamic growth model due to great uncertainty as to the applicability of the available thermodynamic parameters. Of course, inclusion of these reactions would likely lead to higher hydroxyl coverage.

4.4.2 Growth per cycle

Defining the number of Al atoms deposited during pulse A by reactions (R₃) and (R₁₃) by

$$N_{Al,R3} = \int_0^{\tau_A+\tau_B} v_3 \phi_{Me} dt \quad (4.12)$$

$$N_{Al,R13} = \int_0^{\tau_A+\tau_B} v_{13} \phi_{Me} dt \quad (4.13)$$

the growth per cycle can be determined as

$$gpc = 10 \varrho_N (N_{Al,R3} + N_{Al,R13}) \quad \text{\AA}/\text{cycle} \quad (4.14)$$

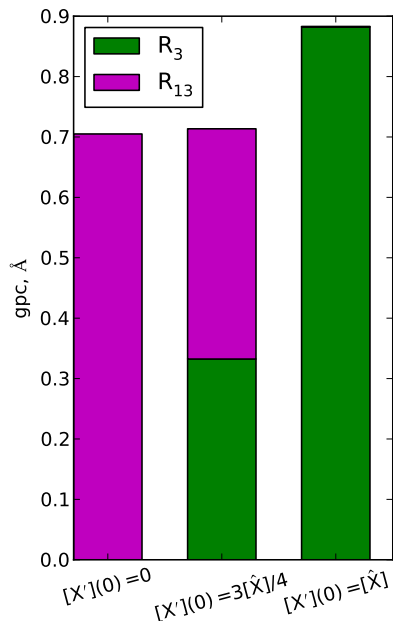


Figure 4.6: *Relative film growth rate contributions of (R_3) and (R_{13}) as a function of initial surface OH group concentration.*

where, as previously stated, ϱ_N is the number density of amorphous Al_2O_3 [156]. Results are shown in Fig. 4.6. In this chart the relative contributions of Al deposited by reactions (R_3) and (R_{13}) are distinguished. The majority of Al atoms are deposited by reaction (R_3) for the fully hydroxylated initial surface state, resulting in an overall growth rate of 0.88 \AA/cycle , a value near the commonly accepted range of $0.9\text{-}1.1 \text{ \AA/cycle}$ as nominal ALD growth under saturating conditions [118, 120, 129, 131, 138, 150]. From Fig. 4.5 (top) one can see that the surface approaches, but does not reach self-saturating conditions during the TMA and water pulses for the fully-hydroxylated initial surface. Thus it would follow that the *gpc* for this case (given the pressure and pulse times used in the model) would approach, but not fully reach the saturating *GPC*. For the intermediate case where the initial surface hydroxyl concentration is $3/4$ the maximum value, both reactions

(R₃) and (R₁₃) share significant responsibility for alumina ALD growth, yielding a *gpc* of 0.71 Å/cycle.

The dominance of reaction (R₁₃) is observed under conditions corresponding to surfaces that are dehydroxylated at the start of the TMA exposure in the left-most plot of Fig. 4.6. Model predictions suggest a growth rate of 0.70 Å/cycle when the surface is completely devoid of hydroxyl groups. These results are consistent with experimental [13, 26, 43, 129, 134, 135, 150, 161] and theoretical [40, 129, 162] studies in which it was concluded that TMA adsorbs at bridged oxygen sites in the case of low hydroxyl group coverage.

Experimental ALD growth data have been reported [135] and numerically analyzed [130] concluding nonzero alumina ALD growth rates on a completely dehydroxylated surface and suggesting that TMA chemisorption under this condition results in three surface methyl groups, which is consistent with the products of reaction (R₁₃). The data in those studies is reported in terms of the number of aluminum atoms deposited per cycle, which may be translated into a growth per cycle using the formulation in [128, 129], similar to Eqn. (4.14) as described herein.

Further, an empirically-based growth model suggested in [130] predicts an aluminum deposition rate which yields a growth per cycle (using the growth rate model in [128, 129]) of approximately 0.5 Å/cycle on a completely dehydroxylated surface. It must be noted, however, that the model is derived from *combined* alumina growth data on both alumina and silica surfaces and from a range of temperatures 353-573 K. Due to these additional variables, only a general comparison should be expected from the model presented herein and the empirical growth data reported

in [130]. Even so, the film growth rate predictions shown in Fig. 4.6 are within reasonable quantitative agreement with experimental ALD growth data [130,135] and are consistent with experiments which suggest TMA surface reaction mechanisms at bridged oxygen sites for low hydroxyl group coverage [13,26,43,129,134,135,150,161].

It is important to note that experimental growth rates are generally quoted as thickness increments per ALD cycle, whereas physically-based models predict *mass* increments per cycle from chemical reactions. Direct comparison between a model and thickness measurements is therefore only possible if the mass density of the film is known, which can vary considerably with precursor chemistry and reactor conditions. Unfortunately, film densities are rarely measured and reported along with thicknesses [38].

4.5 Concluding Remarks

In this chapter, a surface reaction kinetics and film growth model was presented based on combined reaction energetics and configurational data from quantum-chemical computational studies and kinetic parameters determined using statistical thermodynamics and absolute reaction rate theory. The reaction mechanisms which are responsible for ALD growth were examined at varying hydroxyl group coverage. Note that precursor exposure (combination of precursor partial pressure and pulsing time) may significantly impact growth rates as was shown in the previous chapter. This study was focused to examine the kinetic reaction mechanism and the effects of surface coverages on kinetic reaction favorability.

Results indicate that TMA dissociation reactions on bare alumina oxygen bridges are kinetically competitive with TMA ligand-exchange reactions with hydroxyl sites. Due to the currently available approximate activation energy for dissociative adsorption and the consequential uncertainty in reaction rate, determination cannot be made as to whether molecular or dissociative adsorption reactions are always kinetically favorable. However, dissociative adsorption does appear to dominate at low surface hydroxylation, while molecular adsorption reaction activity grows with increasing hydroxylation and appears to dominate at saturation. Maximum ALD growth was only achieved at an initially saturating hydroxyl group density. Together molecular and dissociative adsorption TMA reactions are more kinetically favored than the other considered reactions and are predominantly responsible for ALD growth.

As such, subsequent reactions to the initial ligand exchange are significantly less favored kinetically, with complete removal of methyl groups during TMA exposure being the least favored reaction even at the upper limit of its reaction rate, confirming that complete removal of all three Me groups during the TMA half-reactions is both thermodynamically and kinetically unlikely. Results further indicate the relative favorability of the water reactions with varying hydroxyl site density. At higher hydroxyl coverage, the dimethyl and monomethyl aluminum species present fair competition for the selectivity of incoming water molecules. However, model predictions suggest that at lower hydroxyl site density, the reaction with the Me_1 species will dominate.

Building on previous mechanistic ALD studies by quantifying surface reaction

rate kinetic parameters, this work provides detailed insight into reaction selectivity and surface species dynamics. The surface reaction and growth-surface dynamics models, when combined with reactor-scale models of precursor transport, constitute useful tools for quantifying the rates of the deposition reactions as well as for dynamic optimization of commercial ALD processes. This will be described in the following chapter.

5

Dynamic ALD Reactor Design

Dynamic reactor-scale models with accurate surface reaction rate expressions are necessary to identify the ALD process operating limits corresponding to saturating growth conditions. One of the most important contributions of system-level reactor models for thin-film processes is the ability to use dynamic models to accurately characterize the time-dependent composition of the reactant gases to which the growth surface is exposed. As such, these models constitute useful tools for the design of novel reactors, quantifying the rates of deposition reactions, as well as for optimization of deposition conditions and adaptation to commercial ALD processes for high-throughput systems.

In this chapter, the ALD surface reaction and dynamic film growth model developed in Chapter 4 is coupled to a dynamic reactor-scale model for a process design application. Effects of structural and parametric changes are assessed in an optimization framework aimed at increasing the ALD growth per cycle. A lumped parameter dynamic model is employed to study the temporal behavior of the ALD process and provides a useful tool for novel design diagnostics.

5.1 ALD Reactor Designs

ALD reactors share many similarities with their CVD counterparts, but there are several key distinctions that reflect the unique features of ALD. One is the need to supply precursors in an alternating fashion hundreds or thousands of times in each deposition process. Reasonable throughput requires this cycling to be carried out as rapidly as possible, thereby putting strict demands on both the precursor source and reaction chamber designs. At the same time, uniform distribution of precursors across the substrate may be necessary to ensure film growth uniformity, although this theoretically should not be an issue for a truly self-limiting ALD process.

There are two distinct types of ALD reactors which can be differentiated by the presence or absence of a carrier gas. The first type is a reactor where precursor gases are delivered into the reaction chamber without the use of a carrier gas (*e.g.* by throttled pumping) and thus the total pressure in the reaction chamber corresponds to the precursor pressure [118]. After each pulse period, the reaction chamber is opened and completely evacuated by use of a vacuum pump. So there is no continuous flow of gases, but rather a series of exposure and evacuation steps. While this approach leads to longer residence times and thus more efficient use of the precursors, the evacuation step is often slow which consequently leads to longer cycle times.

Another type of reactor, the most employed design in practice, is a continuous flow reactor where precursors are introduced into the reaction chamber with an inert carrier gas which flows continuously to a downstream vacuum pump. This carrier

gas is used for transportation of the precursor species and to facilitate purging, which is faster than evacuating the reaction chamber between each precursor pulse [31]. Thus, the advantage of this continuous flow reactor is much shorter cycle times relative to the previously discussed design. Most often nitrogen or argon is used as the inert gas at flow rates yielding a reaction chamber pressure in the range 1 – 10 Torr [140]. In these flow-type reactors, the residence time in the chamber is often very short due to the high flow rate of the carrier gas, consequently making the precursor pulse dispersion much smaller when compared to the previous design. But theoretically, this should not be an issue due to the self-limiting nature of ALD reactions. Because this is the more widely used design, all further reactor components will be discussed in the context of the continuous ALD flow reactor.

5.1.1 Precursor Delivery

As previously noted, the primary feature of ALD is separate and sequential precursor pulsing intervals providing means for self-limiting film growth. This requires a separation of the precursor source and the reaction chamber by a mechanical valve or some other rapid valving system. To avoid deposition in the source lines, precursors are commonly transported to the reaction chamber along separate lines, one for each precursor.

For precursors with sufficient vapor pressure, a pulsing valve separates the source from the reaction chamber, and, when the valve is opened, precursors are simply drawn into the carrier gas stream by a pressure differential across the control valve. Since a pressure drop across the valve is the necessary driving force, it follows

that precursor gases (or liquids) must have a vapor pressure higher than the reaction chamber pressure in order for this precursor delivery method to be effective. In some cases, the precursor will need to be heated to reach the desired vapor pressure, in which case the control valve and source lines must also be heated to prevent condensation. A bubbler may be used for precursors with insufficient vapor pressure or when a faster delivery rate is desired, *e.g.* for large surface area applications [140].

In some instances, there may be the desire to carefully control the amount of precursor gas that enters the reactor in any given pulse period. Of course the pulsing valve enables one to control dosing level by adjusting the amount of time that the valve is allowed open. To more accurately control dosing, however, two valves may be placed in series with a storage volume in between [63, 157]. So, the configuration of the precursor delivery system would be

source \rightarrow control valve \rightarrow storage volume \rightarrow control valve \rightarrow reaction chamber.

First, the valve near the source is opened and the high vapor pressure of the precursor facilitates flow across the control valve, thereby filling the storage volume. Then, the first valve is closed and the valve nearest the reaction chamber is opened, thereby evacuating the storage volume and introducing the precursor into the reaction chamber. Using this method and monitoring the pressure inside the storage volume enables one to accurately compute and control the precursor dose.

5.1.2 *Reaction Chamber*

Single-wafer ALD reactors may have different configurations for gas flow—usually either “cross-flow” (also called flow-channel or traveling-wave) or “showerhead” (also called perpendicular-flow). In a cross-flow reactor, gases flow parallel across the substrate, whereas gases flow perpendicular to the substrate in showerhead designs. When the gas inlet is very near to the substrate, the design may be better described as radial-flow and shares more similarities with the cross-flow design in terms of advantages and disadvantages [44].

Compared to the showerhead design, the cross-flow reactor has the advantage of higher throughput. This speed benefit arises from the simple geometry of the reaction chamber, in that the height of the channel (distance from the substrate to the top wall of the flow channel) can be made to be very small, on the order of millimeters. In these high-aspect-ratio systems, precursor molecules collide multiple times with the substrate along the length of the reactor, thereby increasing the probability that it will find an open adsorption site as well as the rate at which the substrate becomes saturated due to irreversible surface reactions [140]. This configuration enables increased precursor utility and shortened exposure time, when compared to a more open reaction chamber design. The small volume of the flow channel also allows for rapid purging of the reactor, another key feature for high-throughput designs.

The disadvantage of the cross-flow reactor is its sensitivity to non-idealities such as precursor decomposition and by-product readsorption, both leading to non-

uniformity in film thickness [94]. When precursor molecules undergo irreversible surface reactions, a by-product is formed which immediately releases to the gas-phase. This by-product can then compete with precursor molecules for adsorption and can also effectively decrease the precursor partial pressure, if sufficient by-product is present. By contrast, the showerhead reactor design theoretically ensures that each site on the substrate receives the precursor pulse at the same time, thereby decreasing by-product adsorption competition.

5.1.2.1 Batch Reactors

To improve the cost and time-effectiveness of commercial ALD processes, batch reactors are often employed to deposit films on multiple substrates simultaneously [44]. While the cycle length for these reactors is often much longer due to the larger reaction volume, shortened cycle times can be achieved when substrates are packed back-to-back to form flow channels similar to the single-wafer cross-flow reactor [62]. Large batch tools of 50-150 wafers (up to 30 cm in diameter) are commercially available and commonly used in the semiconductor industry [21, 52, 115] as well as other industries, *e.g.* 44 substrates measuring 40×50 cm or 82 substrates at 16×27 cm [140, 141].

5.2 A Continuous Cross-flow ALD Reactor

The laboratory-scale ALD reactor considered in this thesis is a continuous cross-flow reactor currently in testing phase and to be used in evaluating ALD for

a range of spacecraft-related thin-film applications [30]. As illustrated in Fig. 5.1, the reaction chamber (RC) consists of a stainless steel process tube surrounded by a bench-top tube furnace, containing the substrate(s) and a quartz crystal microbalance (QCM) for real-time mass deposition measurements. The reactor performance will be initially tested with the commonly used ALD precursors of trimethylaluminum and water; both are contained in the liquid state in temperature-controlled laboratory bottles. External induction heating is provided by a furnace which surrounds the reaction chamber, acting as a hot-wall temperature controller (TC). Each of the precursors flows through a separate sequence of needle valves/orifices to control their flow rates and, then, through solenoid-activated control valves, CV1-5, to regulate the precursor dosages and lengths of the purge periods.

A mass flow controller (MFC) is used to regulate the Argon purge gas flow rate, and low-pressure manometers (P1 and P2) respectively record gas pressure at the reactor outlet and the small ballast chamber (BC) used to regulate the TMA dose. Residual gas analysis (RGA) is performed using a mass spectrometer; the primary pressure controller (PC) consists of a vacuum pump located downstream of the RGA, and a smaller pump is used to vent water vapor between water doses. Reactor dimensions and other reactor component specifications are listed in Table 5.1.

Table 5.1: *Reactor dimensions and primary system component design parameters of the ALD reactor system shown in Fig. 5.1. TMA, trimethylaluminum.*

Parameter	Description	Value
A_s	substrate growth surface area	$6.45 \times 10^{-4} \text{ m}^2$
A	total growth surface area	0.207 m^2
L	reactor length	0.864 m
AR	aspect ratio	11.3
\dot{m}_I	Ar mass flow controller range	0 – 500 sccm
R	reactor internal radius	0.0381 m
V	reactor volume	$3.94 \times 10^{-3} \text{ m}^3$
V_{bc}	TMA ballast chamber volume	$7.85 \times 10^{-7} \text{ m}^3$ (0.02% of V)
S_t	primary exhaust pump capacity	$14.6 \text{ ft}^3/\text{min}$

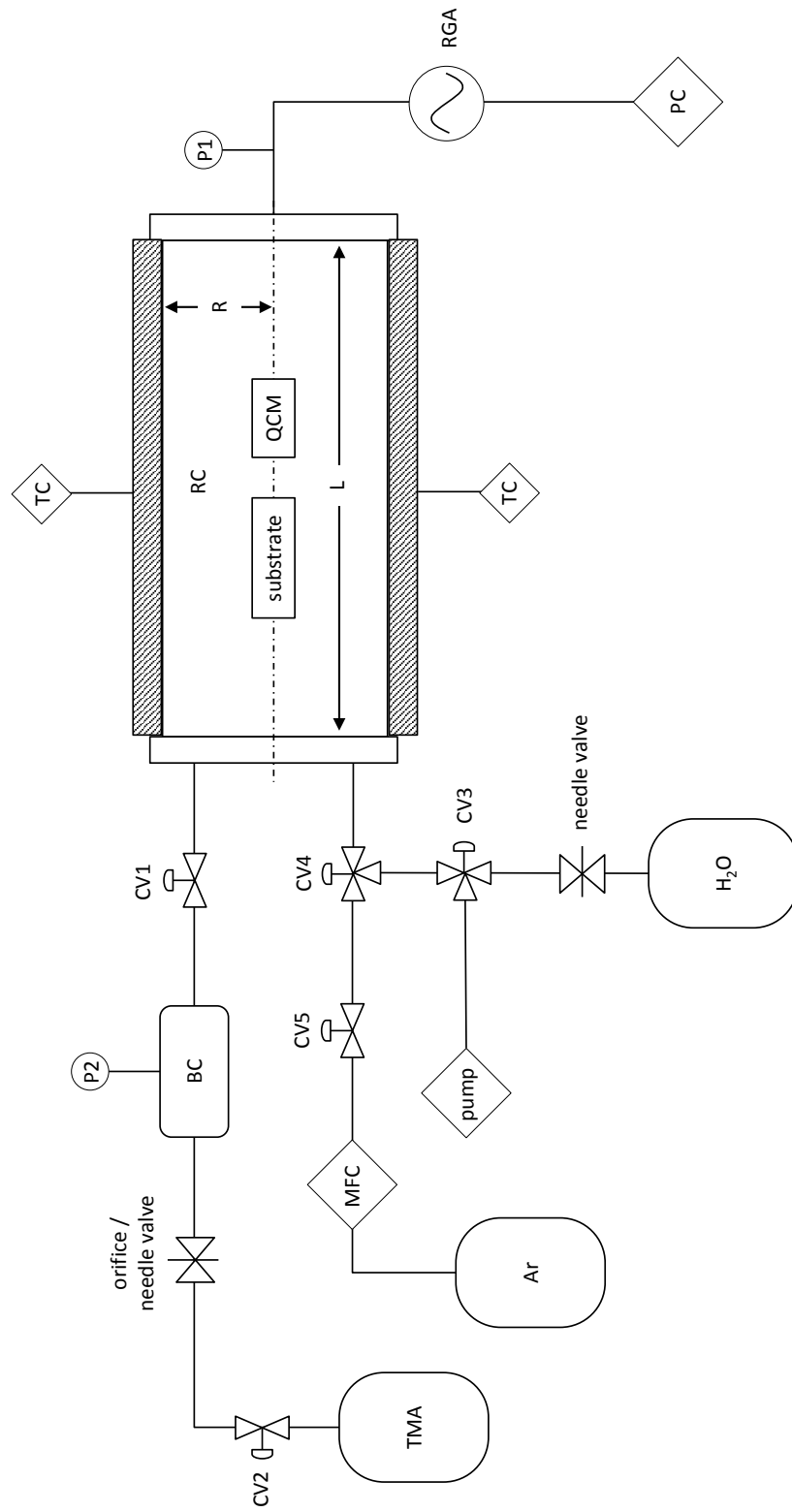


Figure 5.1: Process and instrumentation schematic of the continuous cross-flow ALD reactor.

5.2.1 Process Recipe

The carrier gas flows continuously while each precursor is introduced sequentially, separated by a purge period to prevent gas-phase reactions.

$$\begin{array}{ccccccccc} \text{pulse A} & \rightarrow & \text{purge A} & \rightarrow & \text{pulse B} & \rightarrow & \text{purge B} & \rightarrow & \text{pulse A} & \rightarrow & \dots \\ \tau_A \text{ sec} & & \tau_{AP} \text{ sec} & & \tau_B \text{ sec} & & \tau_{BP} \text{ sec} & & \tau_A \text{ sec} & & \dots \end{array}$$

where the AB cycle repeats—potentially thousands of times—building the film one submonolayer at a time. After the initial nucleation transient following a change in the precursor system (*e.g.*, when depositing a nanolaminate consisting of alternating thin-film materials), the deposition behavior during each AB cycle approaches a limit-cycle solution, the computation of which is the main focus of this simulation study. The time length (in seconds) for the AB pulses and purge periods are denoted as τ_A , τ_B , τ_{AP} and τ_{BP} , respectively.

Referring to Fig. 5.1, control valves CV2 and CV5, normally are open during all pulse and purge periods and, so, will not be discussed further. During the purge period prior to pulse A, CV1 is closed to allow TMA to fill the ballast chamber; the TMA partial pressure in this chamber can potentially reach the vapor pressure of TMA in the supply bottle containing liquid-phase TMA. During pulse A, CV1 is opened to allow TMA vapor to flow into the reactor, reducing the pressure in the ballast chamber. Note that a small flow of TMA will continue through the orifice/needle valve during pulse A. At the end of pulse A, CV1 is closed, and the pressure rebuilds in the TMA ballast chamber.

Regardless of the position of CV4, Ar carrier gas flows continuously during

all pulse and purge periods. During both purge periods and during pulse A, CV3 is open between the water source and the water purge pump, as well as to CV4; however CV4 is closed in the direction of CV3, resulting in no water flow to the reactor. During the water pulse, CV4 is switched to the all-open position, but CV3 is closed in the direction of the water purge pump, allowing the flow of Ar and water to the reactor. This configuration was designed to prevent condensation in the water delivery system and to improve the reproducibility of the water dose [82].

5.3 Precursor Characteristics

Development of the ALD reactor system model begins with precursor thermophysical property and precursor delivery system modeling. From the National Institute of Standards and Technology (NIST) WebBook [114], the Antoine’s equation coefficients for TMA (between 337–400 K) and water (between 293–343 K) are determined as

$$\log_{10} P_{TMA}^{vap} = 4.67984 - \frac{1724.231}{T - 31.398} + \log_{10} \frac{760}{1.01325} \quad (5.1)$$

$$\log_{10} P_{H_2O}^{vap} = 6.20963 - \frac{2354.731}{T + 7.559} + \log_{10} \frac{760}{1.01325} \quad (5.2)$$

where the vapor pressure units are Torr and T is in K. The vapor pressures computed by these relationships corresponding to the TMA and water sources are given in Table 5.2.

As pointed out in [166], at lower temperatures and higher TMA partial pres-

tures, the dimer of TMA (d-TMA) is favored over the monomer (m-TMA) in the gas phase. This is important in determining the true dose values for the precursor delivery system. The d-TMA dissociation extent as a function of temperature was studied in [92], where values for the degree of dissociation, α , were given as a function of temperature. The degree of dimer dissociation is defined as follows

$$\alpha = \frac{\text{moles of m-TMA}}{\text{moles of m-TMA} + 2(\text{moles of d-TMA})} = \frac{\text{moles of m-TMA}}{n_A^\circ} \quad (5.3)$$

where n_A° is the total number of $\text{Al}(\text{CH}_3)_3$ molecules whether in monomer or dimer form. Using a least-squares procedure, an exponential expression was fit to the data contained in the cited source to find

$$\ln K_d = -\frac{13756.5425}{T} + 32.2019 \quad (5.4)$$

where T again is in K. For a binary mixture of d-TMA and m-TMA, the equilibrium expression may be written as

$$K_d = \frac{(y_m P_{TMA}^{vap}/P^\circ)^2}{(1 - y_m) P_{TMA}^{vap}/P^\circ} \quad (5.5)$$

for the mole fraction of the monomer y_m with $P^\circ = 760$ Torr. Note that the m-TMA mole fraction is related to the degree of dissociation, α [92], by $y_m = 2\alpha/(1 + \alpha)$ when considering a binary mixture.

In a mixture containing additional species that do not participate in the dimerization reaction, defining n_N as the total moles of species not participating in the

Table 5.2: *Nominal ALD reactor conditions. d-TMA, dimer of TMA.*

Parameter	Description	Value
\dot{m}_I	nominal Ar molar flow	3.72×10^{-4} mol/s
m_{base}	reactor base molar capacity	1.42×10^{-4} mol
τ_{res}	reactor base residence time	0.381 s
T_{amb}	ambient temperature	300 K
T_{bc}	ballast chamber temperature	300 K
T	reactor temperature	450 K
P_{base}	reactor base pressure	1.01 Torr
$P_{bc,base}$	ballast chamber base pressure	13.67 Torr
ΔP_z	base pressure drop across reactor	6.8×10^{-4} Torr
P_{TMA}^{vap}	TMA vapor pressure at T_{amb}	13.67 Torr
$P_{H_2O}^{vap}$	water vapor pressure at T_{amb}	26.82 Torr
α	d-TMA dissociation degree at T_{amb}	4.04×10^{-3}
x_1	base pressure differential ratio at CV1	0.93
x_2	base pressure differential ratio at CV2	0.00
x_3	base pressure differential ratio at CV3	0.96
τ_A	Pulse A	0.1 s
τ_{AP}	Purge A	4 s
τ_B	Pulse B	0.1 s
τ_{BP}	Purge B	4 s

d-TMA/m-TMA reaction, the gas-phase m-TMA and d-TMA mole fractions, y_m and y_d , can be written in terms of α , as follows

$$y_m = \frac{2\alpha}{1 + \alpha + 2\phi}, \quad y_d = \frac{1 - \alpha}{1 + \alpha + 2\phi} \quad (5.6)$$

where $\phi = n_N/n_A^\circ$. If K_d corresponds to the d-TMA dissociation equilibrium coefficient determined above, defining

$$\frac{y_m^2}{y_d} = \kappa = \frac{P^\circ K_d}{P} \quad (5.7)$$

allows for the following.

$$\alpha = \frac{-\kappa\phi + \sqrt{\kappa^2\phi^2 + \kappa(4 + \kappa)(1 + 2\phi)}}{4 + \kappa} \quad (5.8)$$

Given the conditions inside the TMA source ($T = 300$ K, $P = P_{TMA}^{vap}$ and $\phi = 0$), the extremely small value of α listed in Table 5.2 shows that TMA leaves the bubbler essentially entirely as the dimer, d-TMA. This can also be observed in Fig. 5.2, where the TMA vapor pressure and degree of dissociation are plotted.

5.4 Precursor Delivery System Model

The objective of this model element is to predict the time-dependent precursor molar flow rates, $\dot{m}_{in}^A(t)$ and $\dot{m}_{in}^B(t)$, as they enter the reaction chamber. As seen in Fig. 5.1, the precursor delivery system is designed to inject a TMA dose regulated

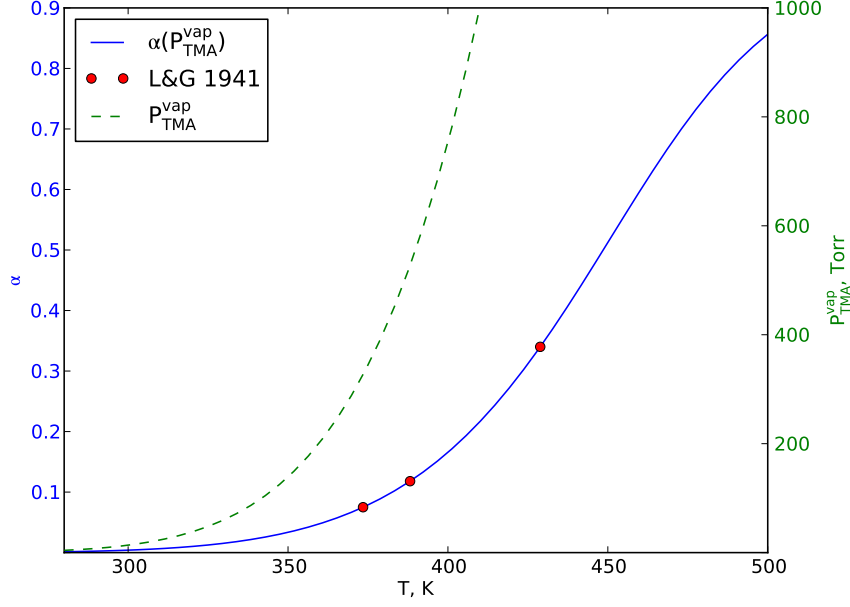


Figure 5.2: *TMA* vapor pressure and degree of dissociation, α , as a function of temperature; data presented in [92] are shown as filled red circles.

by the size of a ballast chamber and the TMA pressure P_2 in this chamber prior to the opening of control valve CV1. A material balance on the ballast chamber is thus written as

$$\frac{dm_{bc}}{dt} = \dot{m}_{CV2} \frac{1 + \alpha_{bc}}{1 + \alpha_{source}} - \gamma_1(t) \dot{m}_{CV1} \quad (5.9)$$

where α_{source} and α_{bc} are the degrees of d-TMA dissociation in the TMA source and ballast chamber, respectively, computed using Eqn. (5.8) with $\phi = 0$. The function γ_1 indicates the time-dependent position of CV1. CV2 is always open under typical operating conditions, allowing for finite gas flow rate whether or not CV1 is open. \dot{m}_{CV1} and \dot{m}_{CV2} are the molar flow rates through control valves CV1 and CV2, respectively.

Following this, the molar flow rate of TMA from the ballast chamber into the

reaction chamber is computed by

$$\dot{m}_{in}^A(t) = \gamma_1(t)\dot{m}_{CV1} \frac{1 + \alpha_{rxx}}{1 + \alpha_{bc}} \quad (5.10)$$

where α_{rxx} is the d-TMA dissociation degree under reactor pressure and composition conditions and is computed using Eqn. (5.8) and ϕ_{rxx} .

Because of the potential for condensation of water in a ballast chamber for this precursor, the alternative design developed by [82] is used where water evaporating in the H₂O source is vented using an auxiliary purge pump during the TMA pulse and purge periods (a similar approach cannot be used for TMA, because of the expense of discarding unused precursor). This configuration gives rise to a relatively simple model for the water dose

$$\dot{m}_{in}^B = \gamma_3(t)\dot{m}_{CV3} \quad (5.11)$$

where the function γ_3 indicates the time-dependent position of CV3 and \dot{m}_{CV3} is the molar flow rate of water through control valve CV3.

The molar flow rate of gases into the reactor is ultimately dependent on the pressure differential between the reaction chamber and precursor storage vessels. The reactor and ballast chamber pressures are computed by

$$P_1 \approx P = \frac{mR_gT}{V}, \quad P_2 = P_{bc} = \frac{m_{bc}R_gT_{bc}}{V_{bc}} \quad (5.12)$$

where P is the reactor pressure, approximately measured by manometer P1.

5.4.1 *Universal Gas Sizing Flow Equation for Control Valves*

The dependence of gas molar flow rate through the control valves would be a significant challenge to predict by a purely physically-based modeling approach. To perform such computations would require (at a minimum) the size and shape of the orifice, the diameter of the pipe, the pressure drop across the valve, and the fluid density. But in addition to this, all of the valve passage dimensions and all of the changes in size and direction of flow through the valve would be required, as well. However, rather than doing these computations, the valve flow coefficient C_v is employed, which combines the effects of all flow restrictions in the valve.

Valve manufacturers determine the valve flow coefficient by testing the valve with water at several flow rates, using a standard test method developed by the International Society of Automation (formerly the Instrument Society of America) for control valves and now used widely for essentially all valves [153]. Following standards set forth by the American National Standards Institute (ANSI) and the International Society of Automation (ISA) [9], the flow rate of a compressible fluid through a control valve can be determined by

$$\dot{m} = NC_v P_{in} \left(1 - \frac{x}{3F_\gamma x_T} \right) \sqrt{\frac{x}{G_g T_{in} Z}} \quad (5.13)$$

where P_{in} is the upstream (or inlet) pressure and $x = \Delta P/P_{in} = (P_{in} - P_{out})/P_{in}$ is the differential pressure between upstream and downstream pressure taps. G_g is the gas specific gravity, the density ratio of the gas to air with both at standard condi-

tions, which is considered in this practice to be equal to the ratio of the molecular weights. T_{in} is the absolute temperature of the inlet stream, Z is the compressibility factor of the fluid ($Z = 1$ for ideal gases), and N is a numerical constant for units. F_γ is a specific heat ratio factor and x_T is the critical pressure differential ratio factor at choked flow. These terms will be discussed further. Parameters for the valve flow model are listed in Table 5.3.

The parenthetical expression in Eqn. (5.13) is known as the expansion factor and accounts for the change in density as the fluid passes from the valve inlet to the *vena contracta* (the location just downstream of the orifice where the jet stream area is a minimum). It also accounts for the change in the *vena contracta* area as the pressure differential is varied. If the inlet pressure is held constant and the outlet pressure pressure is progressively lowered, the mass flow rate through a valve will increase to a maximum limit, a condition referred to as choked flow. Further reductions in outlet pressure will produce no further increase in flow rate. This limit is reached when the pressure differential x reaches the value of $F_\gamma x_T$.

The limiting value of x is defined as the critical differential pressure ratio. Thus, the value of x , for computational purposes, is held to this limit. Although the actual pressure differential ratio may be greater, x is not to exceed $F_\gamma x_T$. If $x \geq F_\gamma x_T$, then the x value is replaced with $F_\gamma x_T$, reducing Eqn. (5.13) to

$$\dot{m} = \frac{2}{3} N C_v P_{in} \sqrt{\frac{F_\gamma x_T}{G_g T_{in} Z}} \quad (5.14)$$

for the choked flow regime. Note that the factor x_T is determined experimentally and

Table 5.3: *Parameters for precursor delivery model. Valve flow equations yield flow rates in units of mol/s with pressure in bar and temperature in K.*

Parameter	Description	Value	Source
N	numerical units constant	4.889	[9]
C_v	Swagelok valve flow coefficient	0.27	[154]
$F_{\gamma,A}$	specific heat ratio factor, TMA	0.8	[9]
$F_{\gamma,B}$	specific heat ratio factor, water	0.9	[9]
x_T	critical pressure differential ratio factor	0.55	[9]
$G_{g,A}$	gas specific gravity, TMA	2.489	
$G_{g,d-A}$	gas specific gravity, TMA dimer	4.889	
$G_{g,B}$	gas specific gravity, water	0.622	
Z	compressibility factor	1	

given for certain valve types. This value is based on air near atmospheric pressure as the flowing fluid with a specific heat ratio of 1.40. The specific heat ratio factor ($F_\gamma = \gamma/1.40$) is thus used to adjust x_T using the appropriate specific heat γ for the flowing fluid.

5.4.2 *Development of a Continuous Flow Equation*

The discontinuity introduced by the switch between non-choked and choked flow may bring rise to numerical difficulties when implementing these flow equations into an iterative Newton-Raphson procedure. The Jacobian matrix elements necessary for this procedure can be computed by finite differences; typically samples are selected within a specified range of a function's input values to determine the derivatives based on the function's response to such sampling. A discontinuous function or one with a discontinuous derivative could be problematic in numerical model implementation, *e.g.* as in the models presented herein.

To avoid these numerical issues, an alternative valve flow equation is proposed

where a single continuous flow equation is used for both choked and non-choked flow. Noting the behavior of Eqns. (5.13) and (5.14) with respect to ΔP and x , a continuous equation is formulated using maximum flow (choked flow) as a horizontal asymptote approached as $x \rightarrow \infty$.

$$\dot{m} = \dot{m}_{choked} \frac{x}{\sqrt{x^2 + (2/3)^2}} \quad (5.15)$$

$$\dot{m} = \frac{2}{3} NC_v \Delta P \sqrt{\frac{F_\gamma x_T}{G_g T_{in} Z}} \sqrt{\frac{1}{x^2 + (2/3)^2}} \quad (5.16)$$

A continuous flow equation may also be formulated using a linear approximation as follows.

$$\dot{m} = \dot{m}_{choked} x \quad (5.17)$$

$$\dot{m} = \frac{2}{3} NC_v \Delta P \sqrt{\frac{F_\gamma x_T}{G_g T_{in} Z}} \quad (5.18)$$

Comparative values of the molar flow rates predicted by these equations are shown in Table 5.4 for a randomized set of pressures. To generate this data, the inlet and outlet pressure was randomized with $P_{in} \in [0, 5]$ bar and $P_{out} \in [0, 5]$ bar and then used to compute the pressure differential ratio x . These values were then supplied to each molar flow rate equation. From the randomized pressure experiment data shown in Table 5.4, one can see that the continuous flow equation approximations are typically within an order of magnitude of the standard ANSI/ISA flow equations, improving in accuracy as the pressure differential increases to the choked

Table 5.4: *Selection of data for comparison of water molar flow rate predictions (mol/s) from randomized pressure differentials. Eqns. (5.13) and (5.14) are standard flow equations based on ANSI/ISA guidelines [9]. Eqns. (5.16) and (5.18) are asymptotic and linear approximations, respectively, to the standard equations.*

ΔP	x	\dot{m} (5.13, 5.14)	\dot{m} (5.16)	\dot{m} (5.18)
0.040	0.014	0.032	0.003	0.002
0.531	0.118	0.137	0.036	0.024
0.928	0.206	0.170	0.060	0.042
1.530	0.313	0.209	0.094	0.069
0.442	0.402	0.049	0.026	0.020
2.248	0.531	0.192	0.120	0.102
1.773	0.640	0.126	0.087	0.080
2.164	0.745	0.132	0.098	0.098
3.889	0.840	0.210	0.164	0.176
3.774	0.938	0.182	0.149	0.171

flow regime, a behavior that is to be expected.

This must be considered in context of the ALD reactor to be modeled. From the nominal reactor conditions listed in Table 5.2, one can see that the pressure in the reaction chamber is significantly lower than pressures in the precursor source containers. An analysis of the nominal pressure differential ratios shows choked flow at CV1 and CV3, while no pressure differential exists at CV2, signifying initial equilibration of the ballast chamber pressure with the TMA source. However, as CV1 is opened and the ballast chamber pressure decreases, then flow will move from non-choked and potentially choked flow across CV2. Because choked flow appears to be the primary regime in the ALD reactor system modeled herein, the lower accuracy of the approximations in non-choked flow may not be significant, except at times for the ballast volume pressure differential with respect to the TMA source. However,

this does not significantly impact flow rate predictions for TMA into the reaction chamber, since the near vacuum reactor pressure will ultimately yield choked flow pressure differentials.

Graphical representation of the randomized pressure experiment used to generate the data in Table 5.4 is shown in Figs. 5.3 and 5.4. The scatter plot arrays are used to demonstrate the qualitative behavior of the valve flow rate equations with respect to ΔP and x for a typical range of pressure differentials $x \in [0, 1]$. One can see that, when combined, the two standard flow rate equations reveal a somewhat asymptotic relation bounded by choked flow, suggesting that a continuous asymptotic equation would be an appropriate approximation tool.

In both figures, the standard non-choked (NC) flow equation predictions are shown in blue with the standard choked (C) flow equation predictions shown in red. The asymptotic approximations (AA) and linear approximations (LA) are both shown in white overlays to the standard equations. From these plots, one can see the boundaries of all flow equations. The standard non-choked flow equation predicts a maximum flow rate, after which point the rate decreases with increase in pressure differential. Of course, this does not make physical sense. On the other hand, the standard choked flow equation predicts a flow rate only dependent on the inlet pressure, which overshoots the flow rate prediction in the low pressure regime. One thus switches between these two equations to yield accurate predictions depending on the pressure differentials across the control valve. This is the standard routine for determining volumetric valve flow rates [9].

Instead of switching between Eqns. (5.13) and (5.14), the asymptotic and

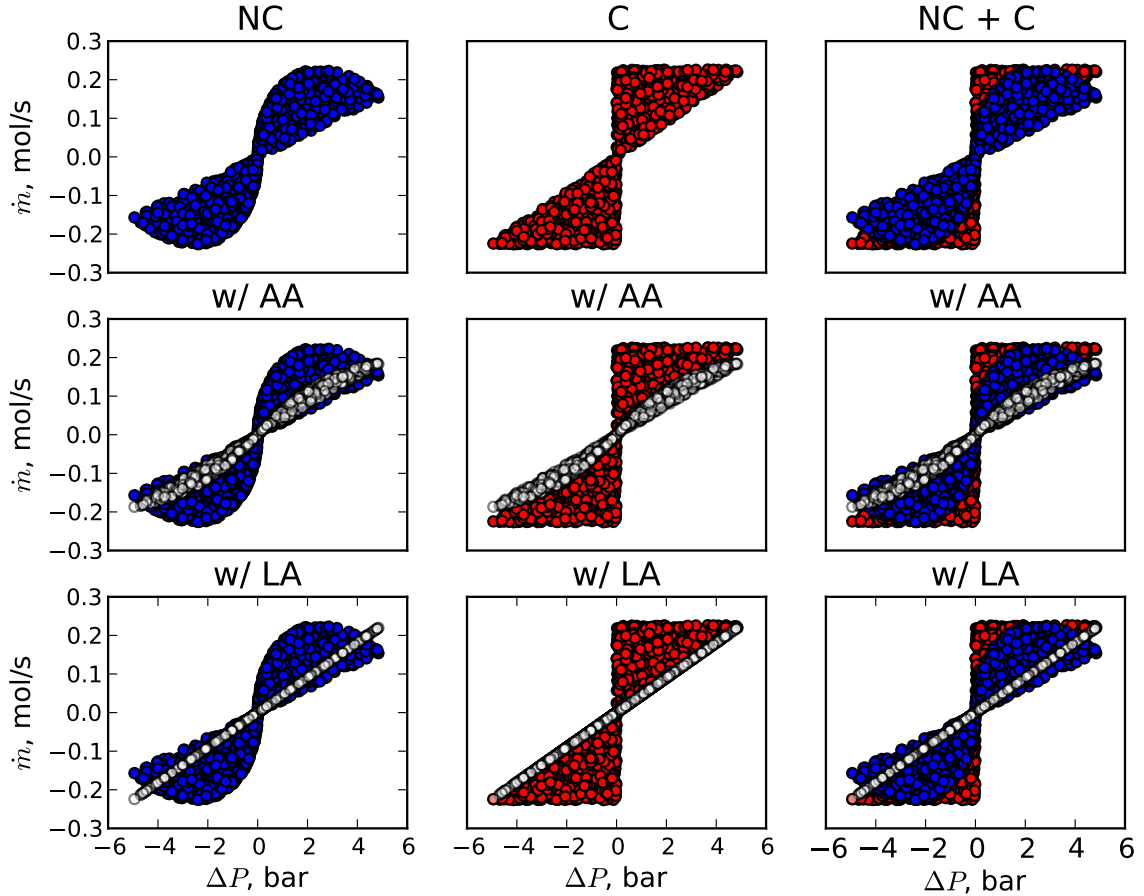


Figure 5.3: Water molar flow rate predictions for a randomized set of pressures using the non-choked (NC) and choked (C) flow Eqns. (5.13) and (5.14). The asymptotic approximations (AA) of Eqn. (5.16) and linear approximations (LA) of Eqn. (5.18) for the same random set of pressures are overlaid, illustrating the approximation boundaries with respect to the standard flow rate formulations.

linear approximation equations suggested herein are used. Specifically, Eqn. (5.16) maintains the qualitative relationship between the molar flow rate and pressure differentials, while also maintaining agreement within an order of magnitude to the standard equations for the pressures of interest in the ALD reaction chamber.

Note that the additive term in the square root of Eqn. (5.16) may be adjusted to better fit the predictions of the standard flow equations, yielding a steeper slope near the origin, as is seen in the non-choked flow rate predictions of Figs. 5.3 and 5.4.

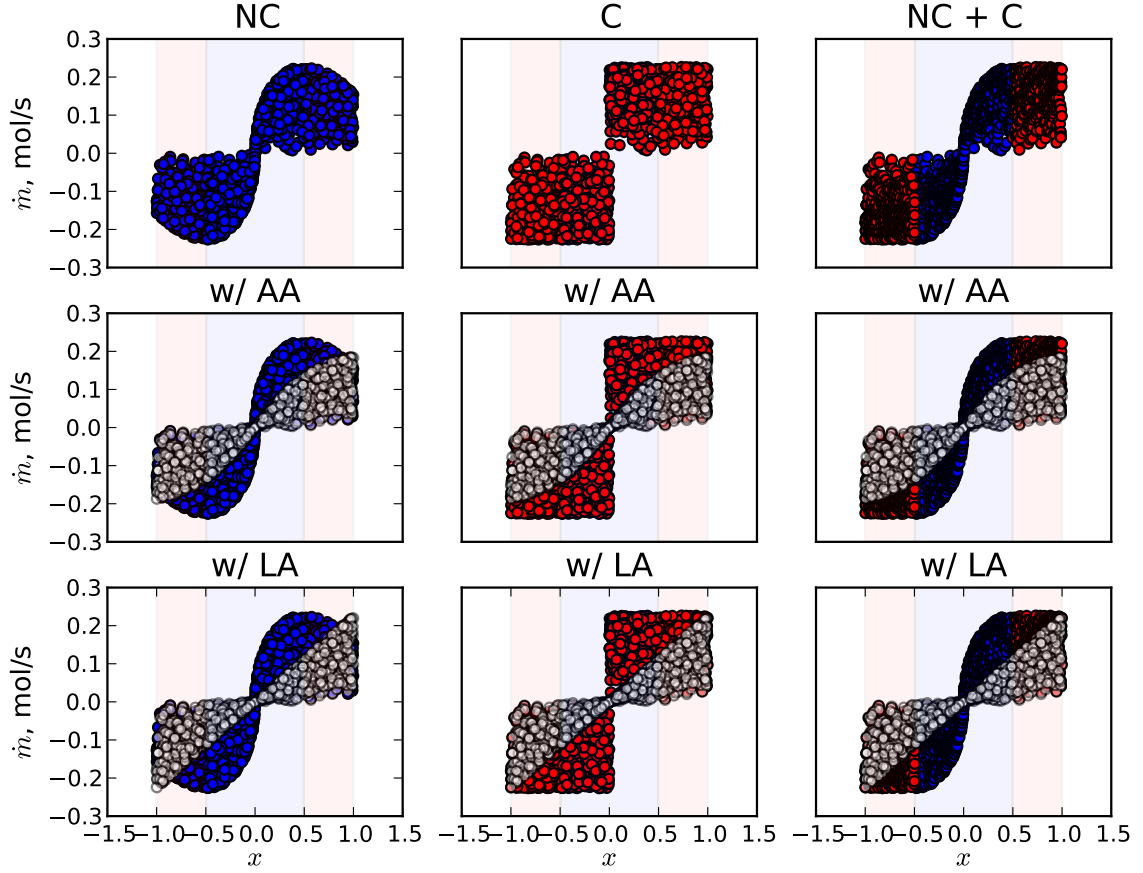


Figure 5.4: Water molar flow rate predictions for a randomized set of pressures using the non-choked (NC) and choked (C) flow Eqns. (5.13) and (5.14). The asymptotic approximations (AA) of Eqn. (5.16) and linear approximations (LA) of Eqn. (5.18) for the same random set of pressures are overlaid, illustrating the approximation boundaries with respect to the standard flow rate formulations. Non-choked and choked flow regions are shaded blue and red, respectively.

However, the flow equation derivatives with respect to pressure become infinitely large in this region, potentially causing additional convergence issues in the numerical model. For this reason, the squared $2/3$ is used. This also has physical meaning: it is the expansion factor under choked flow. When $x \rightarrow 0$, this term cancels with the expansion factor in the equation, yielding an expansion factor of approximately one, consistent with low pressure-drop in non-choked flow.

5.5 Reactor Model

With the precursor delivery model in place, the reactor model can now be developed. Defining $m(t)$ as the total moles of gas-phase species in the reaction chamber, \dot{m}_{in} , the total reactor feed molar flow rate, and \dot{m}_{out} , the molar flow of residual gas out of the reactor, an overall reactor material balance gives

$$\frac{dm}{dt} = \dot{m}_{in} - \dot{m}_{out} - (\Gamma^A + \Gamma^B + \Gamma^C + \Gamma^D) \quad (5.19)$$

The instantaneous consumption rates of the TMA and water precursors Γ^A and Γ^B , methane by-product Γ^C , and gas-phase side-reaction product Γ^D are based on the reaction kinetics model of Chapter 4. The surface phase rate equations are coupled to the gas phase through the precursor partial pressures P_A and P_B . To compute the rate of gas-phase depletion of the precursors due to the surface (and possibly gas-phase) reactions and the rate of by-product production, the rates of consumption (positive quantities) of TMA, water, methane, and DMA-OH must be determined. These are denoted as Γ^A , Γ^B , Γ^C , and Γ^D respectively:

$$\Gamma^A = (v_3 + v_{13})\phi_{Me}A + v_{27}V \quad \text{molecules/s} \quad (5.20)$$

$$\Gamma^B = (v_{16} + v_{19} + v_{24})\phi_XA + v_{27}V \quad (5.21)$$

$$\Gamma^C = -[v_3\phi_{Me} + (v_{16} + v_{19})\phi_X]A - v_{27}V \quad (5.22)$$

$$\Gamma^D = -v_{27}V \quad (5.23)$$

Vacuum pump capacity is rated by the volumetric pumping capacity per unit time, S_t , given in Table 5.1. Over the pump's operating range, this value is considered pressure-independent. Based on m , the reactor instantaneous total pressure is computed using the ideal gas law Eqn. (5.12); so, the residual gas molar flow rate can be computed by

$$\dot{m}_{out} = \frac{S_t P}{R_g T} = \frac{m S_t}{V} \quad (5.24)$$

The total molar feed to the reactor is the sum of the precursor and inert flow rates, and so

$$\begin{aligned} \dot{m}_{in} &= \dot{m}_{in}^A(t) + \dot{m}_{in}^B(t) + \dot{m}_{in}^I(t) \\ &= \gamma_1(t) \dot{m}_{CV1} \frac{1 + \alpha_{rxr}}{1 + \alpha_{bc}} + \gamma_3(t) \dot{m}_{CV3} + \dot{m}_{CV5} \end{aligned} \quad (5.25)$$

Under steady flow conditions with no precursor feed, such as at the end of a very long purge period, no surface reactions take place, and so, the *baseline* reactor pressure is defined using $\dot{m}_{out} = \dot{m}_{in} = \dot{m}_{in}^I$ and

$$P_{base} = \frac{R_g T}{S_t} \dot{m}_{in}^I \quad (5.26)$$

which for a nominal argon flow \dot{m}_{in}^I gives P_{base} listed in Table 5.2.

Defining y_A as the gas-phase mole fraction of m-TMA plus d-TMA and y_B , y_C and y_D as, respectively, the gas-phase water, methane, and DMA-OH mole fractions,

the dynamic species conservation equations can be written as follows

$$\frac{dm}{dt} = \dot{m}_{in} - \frac{mS_t}{V} - (\Gamma^A + \Gamma^B + \Gamma^C + \Gamma^D) \quad (5.27)$$

$$m \frac{dy_A}{dt} + y_A \frac{dm}{dt} = \dot{m}_{in}^A - \frac{mS_t}{V} y_A - \Gamma^A \quad (5.28)$$

$$m \frac{dy_B}{dt} + y_B \frac{dm}{dt} = \dot{m}_{in}^B - \frac{mS_t}{V} y_B - \Gamma^B \quad (5.29)$$

$$m \frac{dy_C}{dt} + y_C \frac{dm}{dt} = -\frac{mS_t}{V} y_C - \Gamma^C \quad (5.30)$$

$$m \frac{dy_D}{dt} + y_D \frac{dm}{dt} = -\frac{mS_t}{V} y_D - \Gamma^D \quad (5.31)$$

subject to initial conditions, $y_A(0)$, $y_B(0)$, $y_C(0)$, $y_D(0)$, $m(0)$, the time-varying state of the growth surface and the total molar inlet flow \dot{m}_{in} , given by Eqn. (5.25). Note that at this time it is unclear whether d-TMA or only m-TMA can participate in the adsorption reactions, and so, the total y_A is used.

5.6 Limit-Cycle Computations

The surface reaction rate equations are coupled to the gas phase through the precursor partial pressures, P_A and P_B , which are used in the surface kinetics model as shown in Chapter 4. Likewise, the rates of precursor depletion and by-product production are computed as functions of the surface and possible gas-phase reaction rates. At this point, the complete model is written as

$$\frac{d\boldsymbol{\xi}}{dt} = \mathbf{f}(\boldsymbol{\xi}) \quad (5.32)$$

and the differential equation right-hand sides, model variables and process recipe parameters can be collected in the following table

modeling differential equations	$\mathbf{f} = [(5.9), (5.27)-(5.31), (4.5)-(4.11)]^T$
process variables	$\boldsymbol{\xi} = [m_{bc}, m, y_A, y_B, y_C, y_D, \theta_{Me_1}, \theta_{Me_2}, \theta_X]^T$
process recipe	$\tau_A, \tau_{AP}, \tau_B, \tau_{BP}, V_{bc}, T = 450 \text{ K}$

where $y_I = 1 - y_A - y_B - y_C - y_D$ and the length of the full process cycle is

$$\tau_{cycle} = \tau_A + \tau_{AP} + \tau_B + \tau_{BP} \quad (5.33)$$

All simulations are implemented in the Python programming language, making extensive use of the PyLab and Numdiff tools modules. Therefore, any computationally specific discussions that follow will be in the context of a Python implementation.

5.6.1 Time Discretization for Forced-periodic Systems

The solution strategy implemented for the dynamic ALD process is to only consider the limit-cycle solutions that describe steady (but periodic) operation of the reactor system during the homodeposition ALD phase; *i.e.* nucleation and other events leading to transients spanning multiple exposure cycles are not considered. Computation of limit-cycle solutions naturally lend themselves to a two-step procedure, where the modeling Eqn. (5.32) is first discretized in time over each pulse and purge period using global collocation over each of the four periods ($\tau_A, \tau_{AP}, \tau_B, \tau_{BP}$), enforcing continuity between each interval, effectively resulting in periodic boundary conditions between the end of pulse B and the start of the next A pulse. The

resulting nonlinear equations, then, are solved using the Newton-Raphson method.

To implement the collocation procedure, the format of the Python array used to represent the time-discretized vector of state variables, $\boldsymbol{\xi} \in R^n$, as $\boldsymbol{\Xi} \in R^{mn}$, must first be defined. For reasons advantageous to computing the Jacobian array elements in the Newton procedure, the Python list, $\boldsymbol{\Xi}$, is defined as a list of the process variables, where $\boldsymbol{\Xi}(\mathbf{i}, \mathbf{j})$ is state j at point i in time; defined in this manner, $\boldsymbol{\Xi}(\mathbf{i})$ is a list representing a snapshot of the states at a specific time. Given this format for the discretized states, the discretized form of Eqn. (5.32) can be written as

$$\hat{\mathbf{A}}\boldsymbol{\Xi} - \mathbf{f}(\boldsymbol{\Xi}) = \mathbf{0} \quad (5.34)$$

where the $\boldsymbol{\Xi}$ list is flattened to the shape appropriate for matrix multiplication using the Python ravel method, and $\hat{\mathbf{A}}$ is defined below.

With $\mathbf{A}^{n \times n}$ corresponding to the standard Lobatto first-order differentiation array (computed using either finite differences or using polynomial collocation techniques), the discretization array suitable for vectors of discretized states, $\hat{\mathbf{A}}$, is created from diagonal $m \times m$ arrays from elements of \mathbf{A}

$$\hat{\mathbf{A}}^{mn \times mn} = \begin{bmatrix} \mathbf{I}_{1,1} & \mathbf{0} & \dots & \mathbf{0} \\ \vdots & \mathbf{a}_{2,2} & & \\ & & \ddots & \\ \mathbf{a}_{n,1} & & & \mathbf{a}_{n,n} \end{bmatrix} \quad \text{with} \quad \mathbf{a}_{i,j} = \begin{bmatrix} A_{i,j} & & 0 \\ & A_{i,j} & \\ & & \ddots \\ 0 & & & A_{i,j} \end{bmatrix}^{m \times m}$$

Note that the identity array, $\mathbf{I}_{1,1}$, has dimensions $n \times n$ and is used to satisfy the

initial conditions. In this study, each of the discretized intervals uses n collocation points (including both endpoints). Writing the vector of discrete points in time over each pulse and purge period,

$$\mathbf{t} = \begin{bmatrix} \mathbf{t}_A \\ \mathbf{t}_{AP} \\ \mathbf{t}_B \\ \mathbf{t}_{BP} \end{bmatrix}, \quad \hat{\mathbf{A}} = \begin{bmatrix} \hat{\mathbf{A}}_A & \mathbf{0} & \mathbf{0} & \mathbf{P} \\ \mathbf{C} & \hat{\mathbf{A}}_{AP} & \mathbf{0} & \mathbf{0} \\ \mathbf{0} & \mathbf{C} & \hat{\mathbf{A}}_B & \mathbf{0} \\ \mathbf{0} & \mathbf{0} & \mathbf{C} & \hat{\mathbf{A}}_{BP} \end{bmatrix}$$

where the off-diagonal blocks, \mathbf{C} , are used for continuity across the spline point, and the off-diagonal block \mathbf{P} is used to enforce periodicity.

5.6.2 Newton-Raphson Procedure

With the discretization complete, the Newton-Raphson procedure is written in terms of the residual, \mathbf{r} , update, \mathbf{u} , and refined solution estimate, Ξ , at iteration ν .

$$\mathbf{r}^\nu = \hat{\mathbf{A}}\Xi^\nu - \mathbf{f}(\Xi^\nu) \quad (5.35)$$

$$\mathbf{u}^\nu = [\mathbf{J}^\nu]^{-1}\mathbf{r}^\nu \quad (5.36)$$

$$\Xi^{\nu+1} = \Xi^\nu + \mathbf{u}^\nu \quad (5.37)$$

While perfectly standard, the Newton-Raphson procedure is presented to point out the structure of the Jacobian array. Numerical approximation of the full Jacobian

array does not take advantage of its structure

$$\mathbf{J}^{mn \times mn} = \hat{\mathbf{A}} - \begin{bmatrix} \left[\frac{\partial \mathbf{f}}{\partial \boldsymbol{\xi}} \right]_{i=0} & 0 & \cdots & 0 \\ 0 & \left[\frac{\partial \mathbf{f}}{\partial \boldsymbol{\xi}} \right]_{i=1} & \cdots & 0 \\ \vdots & \vdots & \ddots & \vdots \\ 0 & 0 & \cdots & \left[\frac{\partial \mathbf{f}}{\partial \boldsymbol{\xi}} \right]_{i=n-1} \end{bmatrix} \quad (5.38)$$

This limits the extent to which a finite-difference procedure must be applied to compute the block-diagonal Jacobian elements corresponding to the relatively complicated nonlinear terms in the rate expressions, precursor thermodynamics descriptions, and reactor material balances. The Jacobian array \mathbf{J} is then constructed in a block-diagonal manner, calling the Python function, `numdifftools.Jacobian`, for each (collocation) point in time to define the block-diagonal elements of Eqn. (5.38).

5.7 Representative Results

A limit-cycle solution is presented in Fig. 5.5 corresponding to a base case design, both in terms of the reactor component specifications and the process recipe. The nominal design parameter values have been listed in Table 5.1. Four sets of plots are presented in Fig. 5.5 in which subplots illustrating the TMA ballast chamber, reactor gas phase, and growth surface composition dynamics are shown. One can observe that all states conform to periodic boundary conditions over the processing cycle; the markers indicate the locations of the temporal collocation points and the shaded rectangles, the collocation interval endpoints.

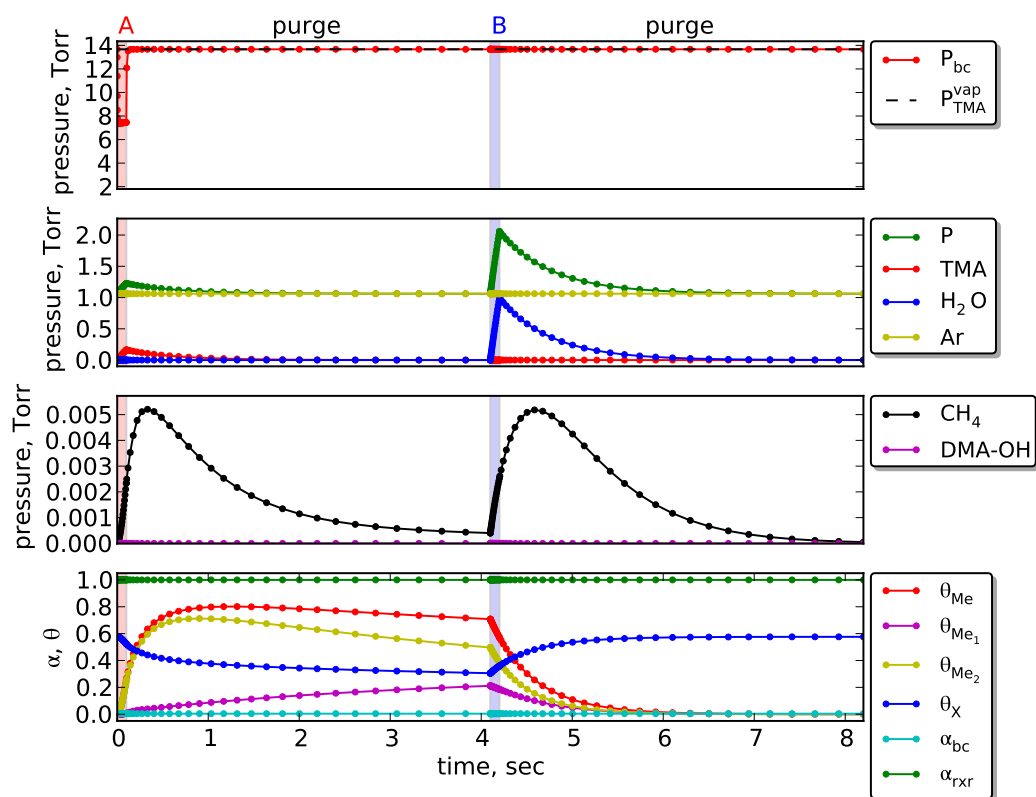


Figure 5.5: *Representative reactor limit-cycle solution with $gpc = 0.806 \text{ \AA}/\text{cycle}$. Reactor nominal conditions consist of $\tau_A = 0.1 \text{ s}$, $\tau_{AP} = \tau_{BP} = 4 \text{ s}$, $\tau_B = 0.1 \text{ s}$ and $V_{bc}/V = 0.02\%$.*

5.7.1 TMA Ballast Chamber Dynamics

The full process limit-cycle is shown to begin with pulse A, where the valve between the ballast chamber and reactor is opened; the valve between the TMA source and ballast chamber (CV2) is always open through the entire process cycle. During pulse A, the TMA flows from the ballast chamber to the reaction chamber, reducing the pressure of the former. At the end of pulse A, the ballast chamber/reactor valve CV1 is closed, allowing the TMA pressure to rebuild during the subsequent purge and B pulse intervals.

As seen in Fig. 5.5, top, the ballast chamber pressure behaves exactly as expected, with a rapid initial drop in pressure, due to the small volume V_{bc} . However, what is interesting to observe is the degree of d-TMA dissociation α_{bc} in the bottom plot of Fig. 5.5: except for a slight upward deviation during the ballast chamber depressurization, $\alpha_{bc} \approx 0$, indicating that virtually all of the TMA is in dimer form while in the TMA ballast chamber.

5.7.2 *Reactor-scale Dynamics*

As seen in the center plots of Fig. 5.5, during pulse A, the total reactor pressure, TMA partial pressure and methane partial pressure all increase as expected, while the Ar carrier gas partial pressure remains constant. During the subsequent purge period, the total pressure relaxes to the baseline pressure. It is now interesting to observe that the TMA monomer fraction in the reactor is essentially unity ($\alpha_{rxx} \approx 1$), indicating that the d-TMA dissociates as it enters the lower-pressure, higher-temperature reaction chamber. Note that the energy required to heat the incoming reactant and inert gases is negligibly small compared to the rates of radiative heat transfer in the reactor, and so, the thermal dynamics of the gases as they are heated to T from T_{amb} or T_{bc} are not explicitly modeled.

During pulse B, a steeper increase in total pressure is observed, because water is supplied to the reactor from a water vapor source held at constant pressure with $P_{water}^{vap} \gg P_{base}$. Again, the system relaxes to the baseline pressure P_{base} after valves CV3 and CV4 are switched to their purge positions.

5.7.3 Growth Surface Dynamics

At the start of pulse A in the limit-cycle solution, $\theta_{Me} \approx 0$ and $\theta_X \approx 0.6$. As TMA enters the reactor, a *small fraction* rapidly reacts with the surface OH, leading to a reduction in θ_X and the increase in θ_{Me} shown in Fig. 5.5. With sufficient TMA dosage levels, $\theta_{Me} \rightarrow 1$ very rapidly, indicating the aggressiveness of the adsorption/ligand-exchange reaction as evidenced by the steep increase in θ_{Me_2} . As the growth surface saturates with Me groups, the rate of the adsorption/ligand-exchange reaction slows, and the rate-controlling step switches to the second ligand-elimination reaction. Observe that additional ligand elimination continues throughout the purge period, reducing both the surface Me_2 and X ligand density. However, the total Me density decreases only slightly, indicating that some TMA adsorption and ligand-exchange reactions continue throughout the purge period until all gas-phase TMA is swept from the reactor.

When water is introduced during pulse B, θ_{Me} rapidly drops as the surface Me groups are replaced with OH in both the dimethyl and monomethyl reactions. As the water partial pressure drops during purge B, all reactions, except residual ligand elimination, come to a stop, leaving a nearly unchanging growth surface for much of the purge period. The full length of the purge period is required, however, to prevent remaining gas-phase H_2O from reacting with surface Me and gas-phase TMA once pulse A resumes.

5.8 Mapping the *gpc* Behavior

As described earlier, a distinguishing feature of ALD processes is the self-limiting nature of the surface reactions, leading to a fixed *gpc* during steady, but cyclic, reactor operation. The total number of Al and O atoms deposited per unit area over one deposition cycle are denoted as N_{Al} and N_O atoms/nm², respectively; these values are computed by integrating the consumption rates of both precursors, as shown in Section 4.4.2, over the limit-cycle using the quadrature weights of the collocation procedure.

Alternatively, if η is the extent of reaction for TMA adsorption/ligand exchange, and this is assumed the only reaction involving gas-phase TMA (*i.e.* neglecting dissociative adsorption), then

$$N_{Al} = \eta = \frac{[Me]_f - [Me]_o + [X]_o - [X]_f}{3} \quad (5.39)$$

where the subscripts, o and f , denote surface concentrations at the start of pulse A and at the end of purge A, respectively. Note that this relationship holds *only* when no reactions take place under CVD conditions (where both gas-phase precursors are found in the reactor, resulting in the possibility of all reactions taking place simultaneously). Under these idealized ALD reactor operating conditions and under fully saturating conditions when dissociative TMA adsorption is negligible, $[Me]_o = [X]_f = 0$ and $[Me]_f = [X]_o = [\hat{Me}]$, resulting in Eqn. (5.39), reducing to the maximum *gpc* possible for an idealized ALD process, a value derived in Chapter 3

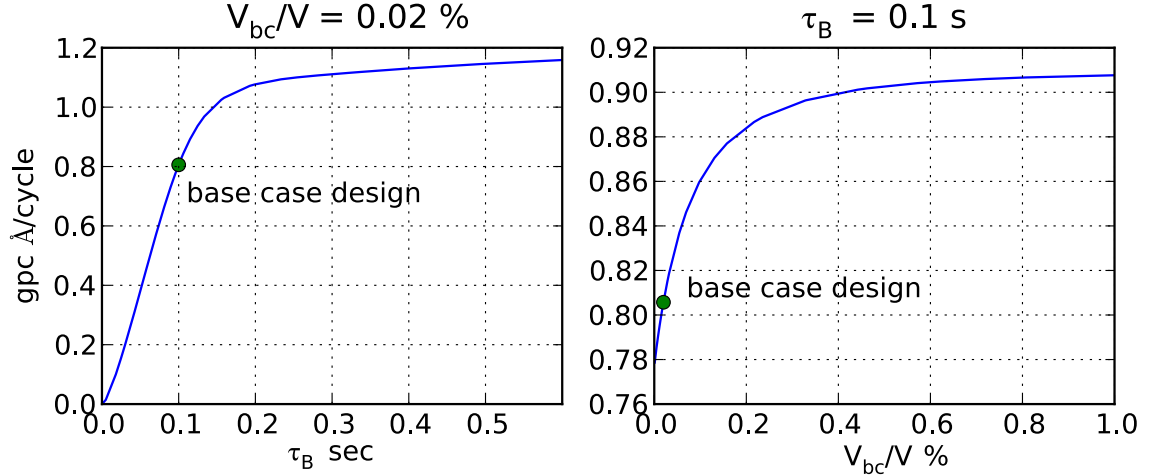


Figure 5.6: *Growth per cycle (gpc) as a function of τ_B (left) and V_{bc}/V (right).*

as $GPC = 1.231 \text{ \AA/cycle}$.

The $gpc = 0.806 \text{ \AA/cycle}$ of the base case design, corresponding to the limit-cycle solution of Fig. 5.5, is much less than the maximum indicated by Eqn. (3.20) for idealized, saturating ALD conditions. Thus, two modes of increasing the dose of each precursor will be examined. During pulse B, the water dose is regulated by the timing of the gas delivery system valves, CV3 and CV4. With a base case design of $\tau_B = 0.1$, observe in Fig. 5.6, left that $gpc \rightarrow 0$ as $\tau_B \rightarrow 0$, while keeping V_{bc} fixed, exactly as expected. Note that $\tau_B = 0$ actually corresponds to a bifurcation point, where the branch containing the limit-cycle solution shown in Fig. 5.5 meets a trivial solution characterized by $\theta_X = \theta_{Me} = 0$ for all points in time. The physical meaning of the multiple solutions will be explored in follow-up work. As τ_B is increased from the nominal operating conditions, the rate of gpc increase lessens; the CVD conditions and the slower surface reactions contribute to the gradual increase in gpc with no self-limiting regime to be found under the selected set of operating conditions of the plot.

The base case ratio of the TMA ballast chamber/reaction chamber volume is 0.02%, and one expects that increasing this ratio will result in an increased TMA dose in the reactor vessel. Keeping the H₂O dose fixed, the overall results are seen in Fig. 5.6, right. As $V_{bc} \rightarrow 0$, $gpc \rightarrow 0.78 \text{ \AA/cycle}$ —not zero—because τ_A is nonzero, and the TMA bleeding through valve CV2 always results in a nonzero TMA dose. Observe that gpc grows with V_{bc} , but again, while the rate of gpc increase declines with ballast chamber volume, a plateau indicating saturating growth is not observed under the operating conditions of the plot.

5.8.1 *The V_{bc} - τ_B Plane*

Because the gpc values of Fig. 5.6 neither reach a limiting value nor the predicted theoretical maximum, $gpc \rightarrow GPC = 1.231 \text{ \AA/cycle}$, the gpc is presented as a contour plot in the V_{bc} - τ_B plane in Fig. 5.7. In this figure, the base case design corresponds to the lower-left corner of the plot.

In Fig. 5.7, $gpc = GPC = 1.231 \text{ \AA/cycle}$ is marked by the white contour line found over this range of τ_B and V_{bc} values. The large region above and to the right of the curve corresponds to large doses of both TMA and water, resulting in growth exceeding what would be possible for a pure, surface reaction-limited ALD process. Examining the limit-cycle solution in this region reveals that because the amount of TMA and water is so large, a significant amount remains after each purge period, resulting in each of the precursors being found in the gas phase at the start of the other pulse period.

During pulse A, excess water in the gas phase reacts with surface Me de-

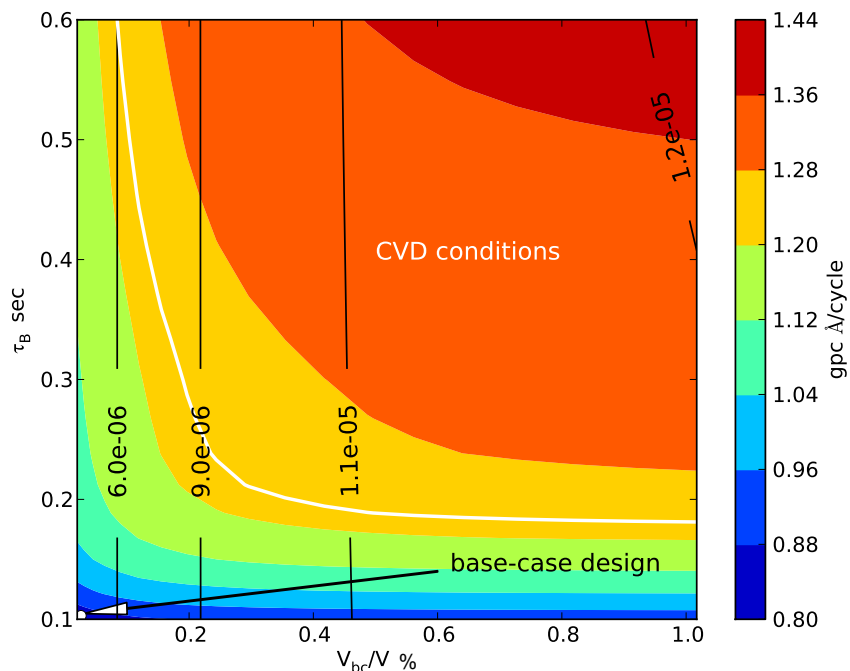


Figure 5.7: Growth per cycle (gpc) as a function of τ_B and V_{bc}/V . The black curves correspond to moles of TMA/cycle supplied to the reactor.

posited by TMA, increasing the ability of TMA to adsorb and react during pulse A. Likewise, excess TMA present at the start of pulse B generates surface Me, which subsequently react with gas-phase H_2O , adding to the overall consumption of that reactant. Likewise, gas-phase reactions occur more readily in this non-ideal region. While the ALD growth model currently does not yet account for film growth as a result of gas-phase reactions, precursor consumption and by-product increase are noted.

These unintentional reactions are characterized as being under CVD conditions instead of true ALD reactions. Because CVD conditions are generally undesirable in ALD processes, due to the poor film quality and reduced conformality produced by the resulting reactions, the curve corresponding to $gpc = GPC$ is marked to indicate an approximate lower limit, where reactions under CVD conditions are significant.

Thus, ALD reactor operation should be limited to the region below and to the left of this curve.

The practical upshot of this computation is immediate: there is little incentive for process designs where $V_{bc}/V > 0.25\%$ and that, generally, $\tau_B > 0.2$ s (given that all other parameters are fixed, of course). The rationale for these limits is further clarified by considering the economics of this ALD process: given the relative value of TMA to water, plus the costs of disposing unused TMA downstream of the reactor, a simple yet reasonable optimization objective would be to minimize TMA use alone. To quantify TMA use, the TMA flow rate through CV1 is integrated using the \dot{m}_{in}^A term of Eqn. (5.25)

$$m_{cycle}^A = \int_0^{\tau_{cycle}} \gamma_1(t) \dot{m}_{CV1}(t) \frac{1 + \alpha_{rxr}}{1 + \alpha_{bc}} dt. \quad (5.40)$$

These curves are shown in black in Fig. 5.7, where the values indicated correspond to moles of TMA/cycle supplied to the reaction chamber. As expected, the contours show a reduction of TMA use as V_{bc} is decreased, but note that for large dose volumes, both τ_B and V_{bc} affect m_{cycle}^A , due to the increased time for regenerating the TMA pressure in the ballast chamber during pulse B.

5.9 Concluding Remarks

In this chapter, a laboratory-scale atomic layer deposition (ALD) reactor system model was developed by integrating components describing the precursor thermophysical properties, precursor delivery system, reactor-scale gas-phase dynamics,

and surface reaction kinetics derived from absolute reaction rate theory. ALD reactor operation was limited to steady cyclic operation with limit-cycle solutions computed using a collocation discretization scheme in time. This study demonstrated that a key advantage to the fixed-point approach was the resulting unambiguous definition of growth per cycle, making possible parametric studies of film growth rates to that expected for ideal ALD.

The utility of the resulting ALD system simulator was demonstrated by the strong interactions found between different reactor, reaction, and process recipe elements, interactions that would be otherwise difficult to predict without such simulators. In particular, this work demonstrated that surface reactions normally associated with one specific precursor exposure can take place during the purge or even during exposures to the other of the two precursors. The ability to model the interaction between pulse and purge periods was critical to uncovering the surface reactions occurring under CVD conditions and identifying processing regimes where these reactions are most likely to take place.

Physically-based models have the capabilities to decouple the effects of precursor pulsing time, reactor temperature and pressure, and the dynamics of each exposure period from the growth per cycle, and can thus distinguish saturating from non-saturating ALD growth conditions. The ability to predict both *gpc* and cyclic precursor feed rates for a real reactor and gas delivery system made it possible to generate simple, but physically meaningful, design rules for adjusting the precursor doses to minimize TMA consumption and undesirable CVD conditions, while maintaining a high value of *gpc* necessary for acceptable reactor throughput. One of the

most important contributions of reactor system-level models for thin-film processes is the ability to use dynamic models to accurately characterize the time-dependent composition of the reactant gases to which the growth surface is exposed. Because direct experimental measurement of gas-phase characteristics local to the growth surface are challenging at best, physically-based reactor models are needed to interpret measured *gpc* levels. The utility of models of this form extend to other ALD process chemistries, other gas delivery systems and more complex (*e.g.*, multi-wafer) reactor systems. The extension of this modeling work to the tubular geometry of the ALD reaction chamber is examined in the chapter to follow.

6

Distributed Reactor Model

In this chapter, the design model presented in Chapter 5 is extended by the development of a distributed transport dynamics model, described by partial differential equations, to take into account the spatial gradients inside the reaction chamber. Although this adds considerable computational complexity to the problem, this work is motivated by a desire to understand film thickness non-uniformity experienced in certain flow-type reactors; recall that non-uniformity is uncharacteristic of self-limiting ALD growth.

In cross-flow ALD reactors, different substrate areas can experience substantially different exposures to by-product gases. If film growth begins only near the leading edge of the substrate, this part is exposed to only a small amount of by-product molecules while the trailing edge will receive a much higher amount [94,140]. Thus, because the trailing edge of the substrate is exposed to a more depleted precursor flow than the leading edge, the observed growth rate across the substrate may be inconsistent [20,52,64]. Spatial non-uniformity was likewise noted in plasma-assisted ALD processes, but reasoned due to a change in growth regime from reaction- to

recombination-limited [85].

The rigorous reactor-scale transport model described in this chapter incorporates the dynamic surface reaction model governing alumina ALD growth outlined in Chapter 3. Through this modeling description, the mass deposited by film growth was conveniently expressed in terms of the spatial and temporal evolution of the surface state for each half-cycle. In this way, the film growth rate per limit cycle and its relative uniformity can be unambiguously defined. Thus, the purpose of this study is to describe a generally-applicable model of ALD precursor reaction and transport that allows a clear identification of the links between growth conditions, precursor properties, and surface coverage profiles.

6.1 Continuous Cross-flow ALD Reactor Model

Reactor geometry and gas-flow conditions are vital elements in film deposition by ALD. Variables such as precursor partial pressure, pulse/purge time, flow rate, reactor dimensions, and reactor layout must be optimized. It is therefore useful to develop models of the complete reaction chamber—flow of gas from the inlet, through the reactor, across the reactive surface, and to the exhaust [36].

In this section, a physically-based model of the continuous cross-flow ALD reactor (see Section 5.2) with temporally separated precursor pulsing is presented. The model component describing the reactor-scale gas-phase dynamics is coupled with the surface reaction and growth dynamics model presented in Chapter 3 and the precursor delivery model presented in Section 5.4 to describe the spatial and

temporal evolution of the ALD growth surface. This model thus encompasses all elements of a complete ALD reactor system model as schematically illustrated in Fig. 1.4.

6.1.1 Formulation of Underlying Model Assumptions

In order to simplify the overall modeling framework and reduce the computational requirements, several assumptions have been made without sacrificing the integrity and applicability of the model. The surface reaction model developed in Chapter 3 has been coupled to the reactor-scale model designed here. Assumptions in relation to the surface reaction mechanism have been previously discussed (see Section 3.1.1). In this multiscale model several additional assumptions have been made in relation to the ALD reactor.

- (i) The reaction chamber is surrounded by a tube furnace which provides a reasonably homogeneous temperature field and precursors are stored in temperature-controlled vessels. Thus, the hot-wall stainless steel reactor tube is assumed to be isothermal [1, 69, 147, 148, 170, 171]. Moreover, because growth rates in ALD are typically only weakly temperature-dependent (within a reasonably small range), temperature uniformity is usually not critical [140]. Of course, the heat equation may be employed in reactors where strong temperature gradients exist.
- (ii) The system is assumed to be thermodynamically ideal, *i.e.* there are no interactions between molecules in the gas phase and the relationship between

pressure and density is defined by the ideal gas law. This assumption is appropriate considering the low operating pressure typical in ALD reactor systems [1, 44, 68–72, 147, 148, 170, 171].

- (iii) Given the high aspect-ratio of the tubular reaction chamber (> 11), flow can be considered to be approximately one-dimensional in the axial direction. Thus the axial velocity of the carrier gas is used as an approximation, understanding that the carrier gas flow is kept constant during all dose and purge periods in the reactor to be modeled despite the pulsed nature of the ALD process. The average axial velocity is found by

$$\langle u_z \rangle = \frac{1}{2} \frac{P^\circ}{P} \frac{T}{T^\circ} \frac{\dot{Q}}{\pi R^2} \quad \text{m/s} \quad (6.1)$$

where \dot{Q} is the volumetric flow rate of the carrier gas at $T^\circ = 273K$ and atmospheric pressure $P^\circ = 1 \text{ atm}$. Reactor temperature T , pressure P , and cross-sectional area πR^2 are used with the ideal gas law to derive the axial velocity which is divided by two in order to obtain the average value [14]. The average axial velocity is a reasonable approximation for continuous flow ALD systems where the carrier gas is kept at a much higher partial pressure than the precursor species [1, 147, 148, 170, 171].

- (iv) Under the nominal reactor operating conditions, the Reynold's number (Re) was determined to be 3.7, well within the laminar region. From this low Re, the entrance region was determined to be less than 2% of the length of the

reaction chamber and thus fully-developed flow is a reasonable approximation. In computing Re , viscosity was determined using the Chapman-Enskog theory for monatomic gases [76] as follows

$$\mu = 2.6693 \times 10^{-6} \frac{\sqrt{m/T}}{\sigma^2 \Omega} \quad \text{Pa s} \quad (6.2)$$

In the equation, m is the atomic weight and σ is the Lennard-Jones molecular diameter as given in [124]. Ω is the diffusion collision integral and is determined from the accurate empirical relation given in [110] which is a function of temperature and the Lennard-Jones well depth, ϵ .

$$\Omega = \frac{A}{T^{*B}} + \frac{C}{\exp(DT^*)} + \frac{E}{\exp(FT^*)} + \frac{G}{\exp(HT^*)} \quad (6.3)$$

where values for A, B, C, D, E, F, G, and H are 1.06036, 0.1561, 0.193, 0.47635, 1.03587, 1.52996, 1.76474, 3.89411, respectively [124] and temperature is related to the Lennard-Jones energy by $T^* = k_B T / \epsilon$.

- (v) Considering the continuous flow ALD reactor where the mass flow rate of the carrier gas is kept constant, vacuum pump speed is kept constant, and the partial pressures of the precursor gases are typically much lower than that of the carrier gas, it is reasonable to assume that no significant spatial gradient in total pressure exists within the reactor, *i.e.* only small pressure variations are encountered in the flow during precursor pulsation. As a simple test of this assumption, the pressure drop across the reactor was computed using the

Hagen-Poiseuille equation [14] as follows.

$$\Delta P = \frac{8\mu L \dot{Q}}{\pi R^4} = \frac{4\mu L u_z}{R^2} \quad (6.4)$$

Substituting the nominal reactor parameters into this equation yields a pressure drop of 6.8×10^{-4} Torr, a value which corresponds to only 0.067% of the base pressure in the reaction chamber. This suggests that the approximation to neglect total pressure gradients (*i.e.* $dP/dz = 0$) is valid for the reactor system in this investigation and thus gaseous species are modeled as incompressible [1, 147, 148, 170, 171].

6.1.2 Model Description

A model is developed which couples chemical species transport equations with a formulation of surface species conservation corresponding to the alumina ALD surface reaction model derived in Chapter 3 to describe the spatial and temporal evolution of the growth surface. As such, all surface reaction modeling equations derived previously should be assumed. Mass transport of chemical species α through the reaction chamber is controlled by the conservative formulation of the convection-diffusion equation in one spatial dimension

$$\frac{\partial P_\alpha}{\partial t} = D_{\alpha I} \frac{\partial^2 P_\alpha}{\partial z^2} - \langle u_z \rangle \frac{\partial P_\alpha}{\partial z} + S_\alpha \quad (6.5)$$

where t and z are time and the spatial coordinate along the length of the reactor, respectively. P_α is the partial pressure of species α , $D_{\alpha I}$ is the binary diffusion coefficient of species α in the inert carrier gas I , and S_α is the source term accounting for the consumption and production rate of α as a result of chemical reactions. Using the ideal gas relationship and applying the product rule,

$$\frac{\partial y_\alpha}{\partial t} = -\frac{y_\alpha}{m} \frac{dm}{dt} + D_{\alpha I} \frac{\partial^2 y_\alpha}{\partial z^2} - \langle u_z \rangle \frac{\partial y_\alpha}{\partial z} + S_\alpha \quad (6.6)$$

where m is the total moles of gas-phase species in the reactor and y_α is the gas-phase mole fraction of chemical species α .

The binary diffusion coefficients were determined from physical properties of the gases using the Chapman-Enskog kinetic theory of dilute gases [67].

$$D_{\alpha I} = 2.6280 \times 10^{-7} \sqrt{T^3 \frac{(M_\alpha + M_I)}{2M_\alpha M_I} \frac{1}{P \sigma_{\alpha I}^2 \Omega_{\alpha I}}} \quad \text{m}^2/\text{s} \quad (6.7)$$

Here, M_α and M_I respectively represent the molecular weights of the α species and carrier gas in atomic mass units, T is absolute temperature, P is the total pressure in atmospheres, and $\sigma_{\alpha I}$ in Ångström units is given by

$$\sigma_{\alpha I} = \frac{1}{2} (\sigma_\alpha + \sigma_I) \quad (6.8)$$

where σ_α and σ_I are the Lennard-Jones molecular diameters of each respective species [124] and $\Omega_{\alpha I}$ is the collision integral determined as previously described.

The self diffusion coefficient for the carrier gas was also determined by the

Chapman-Enskog kinetic theory by the following.

$$D_I = 2.6280 \times 10^{-7} \sqrt{\frac{T^3}{M_I P \sigma_I^2 \Omega_I}} \quad \text{m}^2/\text{s} \quad (6.9)$$

6.1.3 Chemical Species Conservation

Applying the precursor delivery model described in Section 5.4 and defining y_A as the gas-phase mole fraction of TMA, and y_B , y_C , and y_D as the gas-phase water, methane, and DMA-OH mole fractions, the reactor material conservation and transport equations can be written as

$$\frac{dm}{dt} = \dot{m}_{in} - \dot{m}_{out} - (\Gamma^A + \Gamma^B + \Gamma^C + \Gamma^D) \quad (6.10)$$

$$\frac{\partial y_A}{\partial t} = D_{AI} \frac{\partial^2 y_A}{\partial z^2} - \langle u_z \rangle \frac{\partial y_A}{\partial z} - \frac{y_A}{m} \frac{dm}{dt} - \frac{\Gamma^A}{m} \quad (6.11)$$

$$\frac{\partial y_B}{\partial t} = D_{BI} \frac{\partial^2 y_B}{\partial z^2} - \langle u_z \rangle \frac{\partial y_B}{\partial z} - \frac{y_B}{m} \frac{dm}{dt} - \frac{\Gamma^B}{m} \quad (6.12)$$

$$\frac{\partial y_C}{\partial t} = D_{CI} \frac{\partial^2 y_C}{\partial z^2} - \langle u_z \rangle \frac{\partial y_C}{\partial z} - \frac{y_C}{m} \frac{dm}{dt} - \frac{\Gamma^C}{m} \quad (6.13)$$

$$\frac{\partial y_D}{\partial t} = D_{DI} \frac{\partial^2 y_D}{\partial z^2} - \langle u_z \rangle \frac{\partial y_D}{\partial z} - \frac{y_D}{m} \frac{dm}{dt} - \frac{\Gamma^D}{m} \quad (6.14)$$

subject to initial conditions at the start of each pulse and purge period. Initial conditions are determined at the onset of the ALD cycle before the first exposure period, while continuity conditions determine the initial conditions from one period to the next. The initial conditions are prescribed as follows: $m(t = 0) = m_{base}$, $y_A(z, t = 0) = 0$, $y_B(z, t = 0) = 0$, $y_C(z, t = 0) = 0$, $y_D(z, t = 0) = 0$, and $y_I(z, t = 0) = 1$, *i.e.* only the carrier gas flows through the reactor initially.

Continuity conditions defined at the initiation of purge A, pulse B, and purge B are such that the values from the final time step in the previous period are conserved. The inert mole fraction y_I is determined by $y_I = 1 - \sum y_\alpha$ where $\alpha = A, B, C, D$. The set of ordinary differential equations (ODEs) derived in Section 3.2.2 to describe the temporal evolution of the growth surface are also solved with the set of partial differential equations above, subject to initial conditions corresponding to the fully hydroxylated state.

6.1.3.1 Boundary Conditions

The inlet boundary conditions for Eqns. (6.11-6.14) are prescribed according to the molar flow rates of the chemical species. As such, the flux across the inlet boundary for each component is specified as follows.

$$J_\alpha|_{z=0} \pi R^2 = \dot{m}_{in}^\alpha \quad (6.15)$$

$$\left(-D_{\alpha I} \frac{dy_\alpha}{dz} \Big|_{z=0} + \langle u_z \rangle y_\alpha|_{z=0} \right) \frac{P}{R_g T} \pi R^2 = \dot{m}_{in}^\alpha \quad (6.16)$$

where \dot{m}_{in}^α varies according to the control valve pulsing sequence. The Neumann condition is enforced at the reaction chamber outlet. Thus, prescribing a constant flux and assuming the diffusive mass flux to be zero, the final boundary condition is written as

$$\frac{dy_\alpha}{dz} \Big|_{z=L} = 0 \quad (6.17)$$

6.1.4 ALD Film Growth

As in Chapter 5, limit-cycle solutions are computed for the multiscale system, requiring the gas-phase and surface state at the end of purge B return to their respective initial conditions consistent with the beginning of pulse A. The surface state is defined by Eqns. (3.7) and (3.8) and as such the film growth computation follows Section 3.7. Recall the material deposited per cycle is found by

$$N_{Al} = \int_0^\tau v_3 dt \quad (6.18)$$

$$N_O = \int_0^\tau (v_8 + v_{11}) dt \quad (6.19)$$

Note that these reaction rates correspond to the reaction mechanism presented in Chapter 3, not to be confused with the reactions numbered in Chapter 4. The material deposited per cycle is key to determining the growth per cycle *gpc* which is computed according to the following.

$$gpc = 10 \rho_N N_{Al} \quad (6.20)$$

Spatial uniformity is investigated in the context of *gpc* and by specifically monitoring the amount of material deposited [69]. The total mass gain from aluminum and oxygen deposition is found by

$$m_s = (N_{Al} M_{Al} + N_O M_O) \frac{10^5}{N_{Avo}} \quad \text{ng cm}^{-2} \quad (6.21)$$

where M_{Al} and M_O are the molecular weights of aluminum and oxygen, respectively.

The average mass gain of the film is governed by

$$\frac{d \langle m_s \rangle}{dt} = \frac{1}{L} \int_0^L m_s dz \quad (6.22)$$

and film uniformity is described by the following.

$$\lambda = 1 - \frac{\int_0^L |m_s - \langle m_s \rangle| dz}{\int_0^L m_s dz} \quad (6.23)$$

In essence, $\lambda = 1 - \text{standard deviation/mean}$, where $\lambda = 1$ for a perfectly uniform film.

6.2 Discretization Procedure

Due to the nonlinear nature and complexity of the modeling equations, computation of the solutions requires a numerical technique. The set of nonlinear partial differential Eqns. (6.11-6.14) are discretized using a central time and central space (CTCS) finite differences technique with non-uniform intervals resulting in a large set of nonlinear algebraic equations. The finite differences mesh is shown in Fig. 6.1 with discretization intervals initialized according to

$$\frac{\Delta t}{\Delta z^2} D_{\alpha I, max} \leq 0.75 \quad (6.24)$$

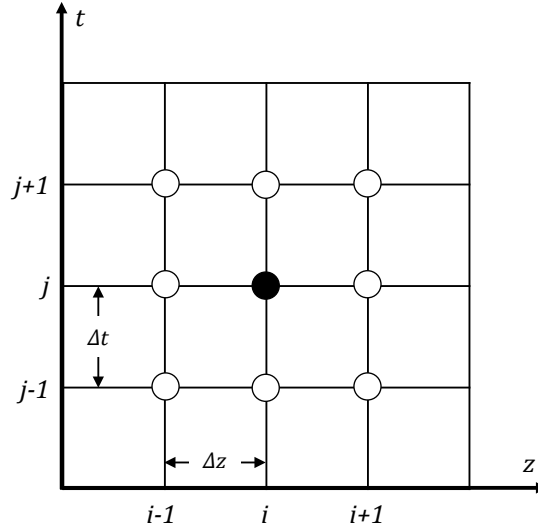


Figure 6.1: *Central time and central space finite differences mesh and solution points.*

where Δt is the nominal time step and $\Delta z = 0.1L$ is the nominal displacement in space set to a tenth of the reactor tube length. The ODEs representative of the material balance on the ballast chamber (Eqn. 5.9) and reaction chamber (Eqn. 6.10) are discretized using the same central temporal discretization steps. All discretized ODEs and PDEs are solved simultaneously in a fashion similar to what has been previously discussed in Chapter 5, employing a Newton-Raphson procedure with an Euler method utilized for the initial guess.

6.3 Representative Limit-Cycle Results

Representative limit-cycle solutions were computed with $\tau_A = 0.5$ sec, $\tau_B = 0.1$ sec, and $\tau_{AP} = \tau_{BP} = 2$ sec. Examination of the precursor pulsing sequence shown in Fig. 6.2 reveals the manner in which the TMA and water precursors propagate through the reaction chamber. From top to bottom, the four plots depict the four steps of the ALD cycle: pulse A, purge A, pulse B, and purge B. At the start of

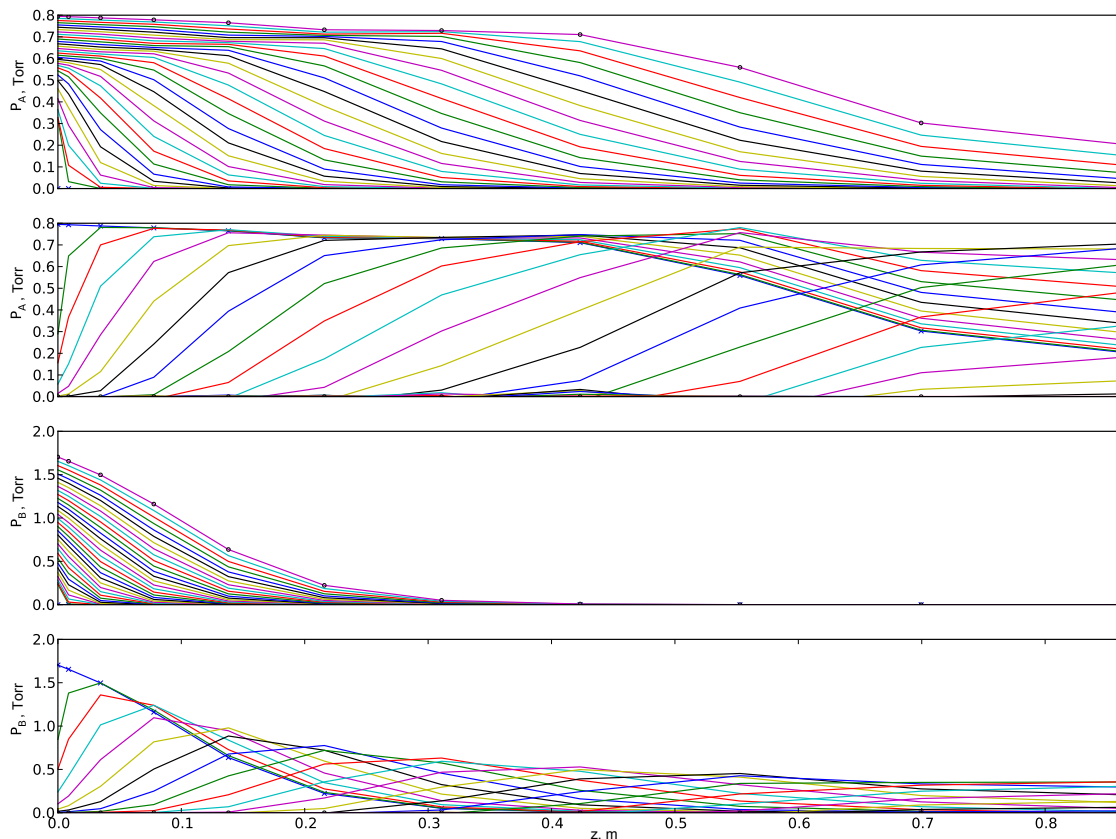


Figure 6.2: *Representative gas-phase dynamics for $T=450K$, and $\tau_A = 0.5$ sec, $\tau_B = 0.1$ sec, and $\tau_{AP} = \tau_{BP} = 2$ sec. Curves show spatial reactor position, with inlet marked by $-x-$ and outlet by $-o-$. In order from top to bottom, the ALD cycle step for each plot is as follows: pulse A, purge A, pulse B, purge B.*

pulse A, no TMA exists in the reaction chamber. As TMA is introduced, a gradual increase in partial pressure is observed along the reaction channel. During purge A, a TMA partial pressure drop is experienced more suddenly near the reactor inlet and then the partial pressure gradually decreases throughout the reactor as residual gases are removed. Following this, a quick and relatively large pulse is experienced during the water exposure. Gaseous species are subsequently swept from the reactor during the next purge period.

While the water pulse time is shorter than the TMA pulse, water precursor de-

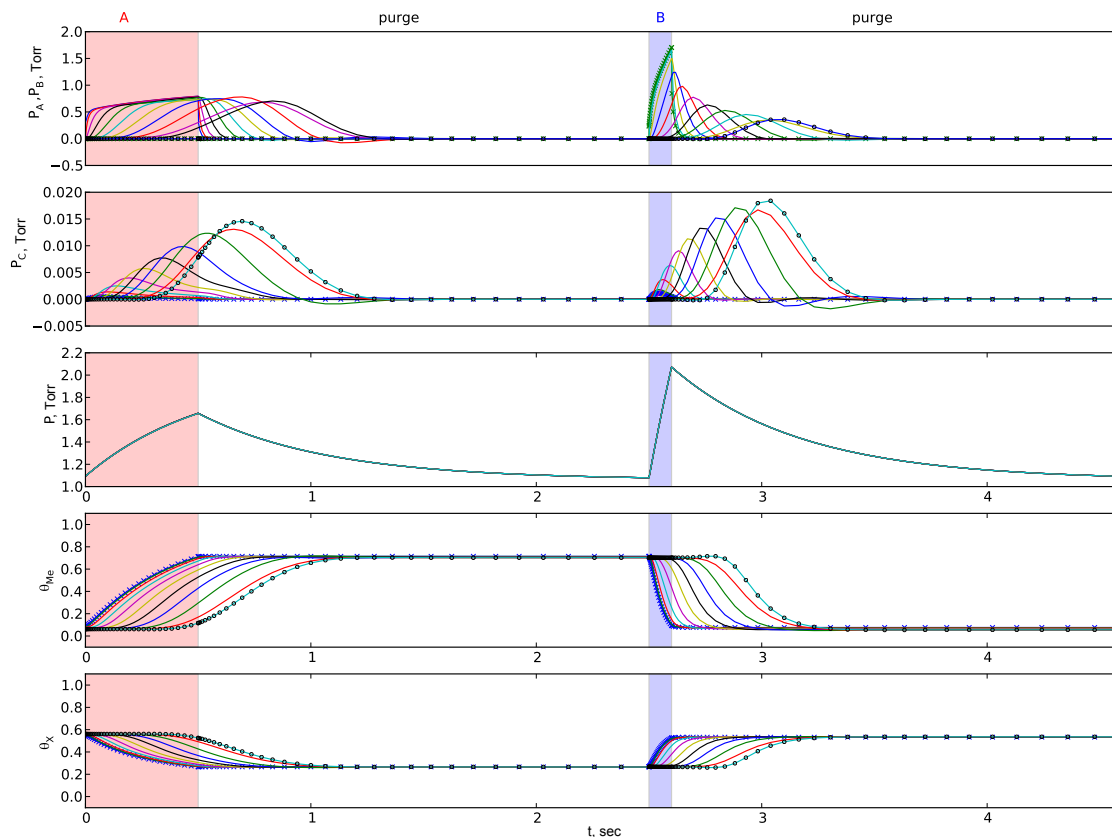


Figure 6.3: *Representative gas-phase and surface dynamics for $T=450K$, and $\tau_A = 0.5$ sec, $\tau_B = 0.1$ sec, and $\tau_{AP} = \tau_{BP} = 2$ sec. Curves show spatial reactor position, with inlet marked by -x- and outlet by -o-.*

livery is actually more efficient than that of TMA due to differences in the precursor vapor pressures. The vapor pressure of water in its source container is significantly higher than that of TMA; and thus the pressure differential across the pulsing valve drives more water into the reaction chamber. Yet both precursor gases are effectively swept from the reactor in the same purge time spans, indicating the important role of the downstream vacuum pump in facilitating precursor propagation through the reaction chamber. This is not surprising considering that convection is significantly more important than diffusion in this system, with relatively large Peclet numbers: $Pe \approx 100$ for TMA and $Pe \approx 40$ for water.

Model predictions of the gas-phase and surface dynamics are shown in Fig. 6.3 with the TMA and water pulse periods shaded red and blue, respectively. In the top plot, the precursor gas dynamics are given as a function of spatial position in the reaction chamber. During each exposure, surface reactions produce methane by-products according to the spatial dynamics shown in the second plot; although, compared to the magnitude of TMA and water partial pressures, the partial pressure of methane gas in the reactor is negligibly small. The next plot in this series is similar to the pressure dynamics shown in the lumped parameter model of Chapter 5. The reactor pressure is normally around 1 Torr, increasing during precursor pulse periods and relaxing back to the nominal pressure during reactor purge periods.

An examination of the growth surface in the last two plots of Fig. 6.3 reveals what appears to be self-limiting growth in both precursor exposure periods, but this is not the case. Neither Me nor OH groups reach maximum values, but growth halts. The methyl group density does not reach the close-packing limit during the TMA exposure, suggesting perhaps a transport-limited situation. However, self-limiting growth is achieved in the water exposure due to methyl group depletion. During the TMA exposure, the growth surface reaches only around 70% saturation, but all methyl groups are removed during the water exposure. This indicates that the current water partial pressure and pulse time are sufficient to chemically react, removing all surface methyl groups; but self-limiting growth for the ALD cycle is not achieved due to insufficient saturation during the TMA exposure. The TMA partial pressure and/or pulse time should therefore be increased to allow for more TMA adsorption and sufficient surface saturation by methyl groups until self-termination.

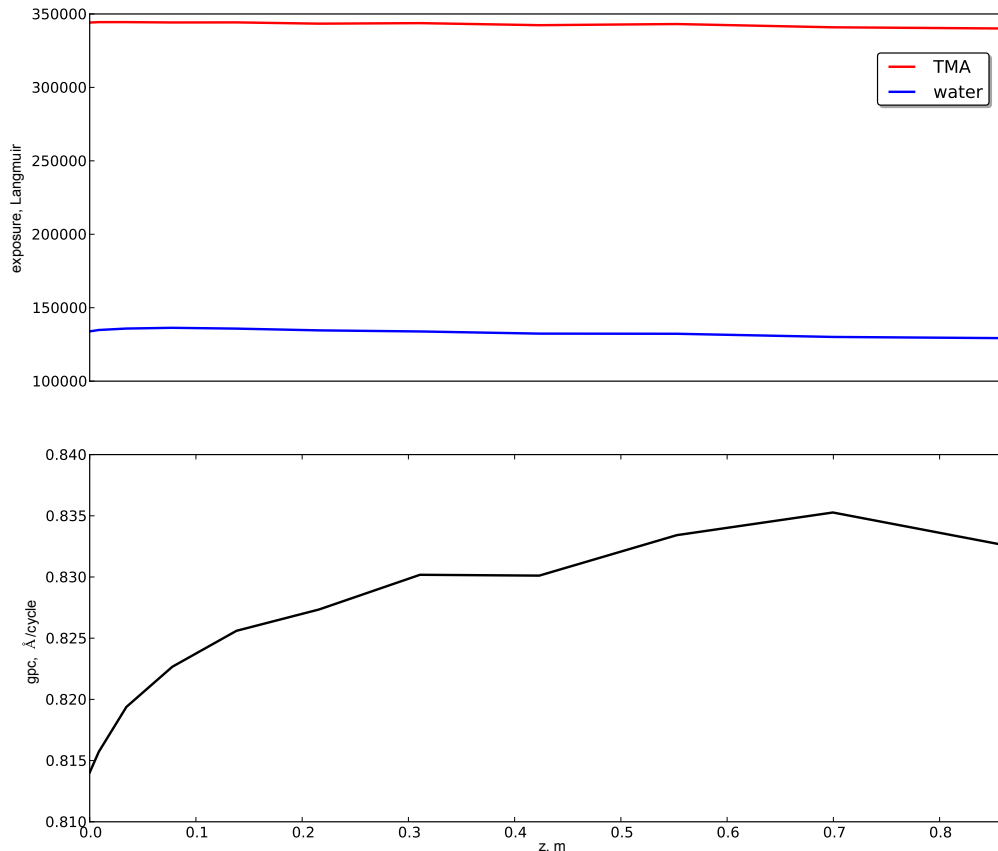


Figure 6.4: *Exposure and growth per cycle predictions as a function of spatial position in the ALD reactor.*

It is interesting to note that a majority of surface reactions occur during the pulse periods. This is interesting because these periods are typically considered only in the context of removing by-products and unreacted chemical species. Thus, the purge dynamics are many times omitted from ALD simulations. These model results show the significance of modeling the complete ALD cycle, including purge period dynamics, as this yields key insight into surface reaction dynamics which could potentially guide more-informed optimization decisions.

Lastly, the spatially distributed growth per cycle and related film uniformity were investigated according to Eqns. (6.20) and (6.23), respectively. The spatially-

distributed exposure and gpc are shown in Fig. 6.4, indicating a higher TMA exposure than water due to the longer TMA pulsing interval. Both exposures, however, were found to be relatively uniform throughout the reaction chamber. One would then expect a relatively uniform growth rate. While the gpc appears to be non-uniform, note that gpc variability is actually very small, hundredths of an Ångström, with $gpc = 0.815 - 0.835$ Å. Moreover, film uniformity was computed for this simulation and $\lambda = 0.99$. Thus, despite under-saturating growth conditions, the ALD film is predicted to be essentially uniform across the length of the reaction channel. This finding highlights a key advantage of ALD growth processes.

6.4 Concluding Remarks

In this chapter, a first principles-derived surface reaction model was coupled to a spatially and temporally distributed reactor system model to describe ALD film growth. Results suggest that reactor transport effects can significantly impact surface coverage dynamics, potentially hindering self-limiting growth. The importance of surface saturation during the TMA exposure was shown by the undersaturating growth rates predicted with insufficient TMA pulsing. Limit-cycle solutions predict a relatively uniform growth rate with $gpc = 0.815 - 0.835$ Å, which falls short of the self-saturating growth regime. Examination of the precursor pulsing dynamics yields more efficient water precursor delivery due to the higher vapor pressure of water. In order to achieve better TMA pulsing, the exposure time length would need to be increased or a more efficient TMA delivery system should be investigated (*e.g.*

use of a bubbler).

The implication of this distributed model is significant due to the level of modeling detail contained in each model component—from precursor source dynamics, to precursor delivery through the control valves, to transport through the reaction chamber, and then to reaction and film growth at the substrate surface. Carefully coupling all of these model components reveal significant growth rate dependencies on the various reactor and operation parameters. Models such as the one presented in this chapter serve as very useful reactor design and optimization tools for existing and potentially novel ALD reactor systems. Further model refinement and optimization will be the subject of follow-up work.

7

Concluding Remarks

The work presented in this thesis was motivated by the need for model-based ALD process optimization and greater understanding of ALD reaction dynamics. This led to the development of a physically-based ALD reaction kinetics and film growth model which is used to examine growth surface dynamics in the period leading to self-saturation during each half-cycle. In coupling this model with reactor-scale transport phenomena, additional insight is given into multiscale process interactions.

Recall the modeling objectives described in the introductory chapter:

- (i) *First principles understanding of reaction mechanisms and growth kinetics*

In Chapters 3 and 4, a physically-based ALD surface reaction kinetics model was presented based on combined reaction energetics from quantum-chemical computational studies and kinetic parameters determined using statistical thermodynamics and absolute reaction rate theory. Several reaction paths were investigated and a kinetic reaction mechanism was suggested based on dynamic film growth rate analysis. Model predictions were in good agree-

ment qualitatively and quantitatively with the experimentally observed ALD mechanism. A key contribution of this work is that the level of modeling detail allows for keen insight into molecular-level surface species interactions and thus provides means to study the ALD saturation and growth mechanism in relation to competing reactions. This analysis also allowed for comparison of suggested thermodynamically favored mechanisms and H transfer paths, details which lead to better understanding of the dynamic ALD growth mechanism. [158]

(ii) *Identification of operating limits for self-saturating growth*

The surface kinetics and limit-cycle growth model described in Chapter 2 was motivated by the predictive capabilities of physically-based models to decouple the effects of reactor input parameters (namely temperature and exposure times) on the measured film growth rate. A key contribution of this model is the demonstration of the transition state applicability to ALD processes, which even for a simplified reaction mechanism, yields growth rate, exposure, and temperature predictions consistent with experimentally-observed reaction phenomena. This demonstrated the applicability of the first principles kinetics modeling approach. Another major contribution of this work is the introduction of the limit-cycle growth model, describing the continuous cyclic operation of the deposition reaction system. Limit-cycle solutions developed were able to distinguish saturating *GPC* from non-saturating *gpc* conditions. The transition between the two regimes was then able to be studied in the context of temperature and exposure, yielding self-limiting growth boundary

predictions. [156]

(iii) *Explanation and prediction of multiscale reaction phenomena*

In Chapters 5 and 6, a laboratory-scale reactor system model was developed by integrating components describing the precursor thermophysical properties, precursor delivery system, reactor-scale gas-phase dynamics, and surface reaction kinetics derived from absolute reaction rate theory. A key finding is that unintended chemical vapor deposition conditions can mask regions of operation that would otherwise correspond to ideal saturating ALD operation. The ability to model the interaction between pulse and purge periods was critical to uncovering the surface reactions occurring under CVD conditions and identifying processing regimes where these reactions are most likely to take place. Extension to the distributed reactor model allowed for discussion of transport effects and reactor parameters associated in film non-uniformity [157,159].

7.1 Suggestions for Future Work

ALD modeling is a specialized niche represented by around 150 papers published mostly over the last decade [38] and only a handful of those papers have implemented physically-based growth models to unelucidate the kinetic reaction mechanism [37]. The modeling work presented in this thesis was thus meant to provide a relatively straightforward framework from which additional models can be derived. Several paths are suggested for continuing this work.

7.1.1 Surface Reaction Mechanism and Kinetics

The ALD modeling efforts described herein reveal an increasingly complex picture of the surface processes taking place even in those systems once thought to represent “ideal ALD,” such as alumina ALD using trimethylaluminum and water as precursors. The scheme of 27 elementary reactions presented in Chapter 4 gives a glimpse into how large these systems of reactions can grow. Therefore, a rational framework must be developed for the analysis and simulation of the increasingly complex ALD surface process models, perhaps using a model dynamic reduction framework which can accommodate the growing number of chemical reactions and species necessary to accurately model ALD growth.

7.1.2 Reactor-scale Model Optimization

Considering the progression of model development in this thesis, it naturally follows to apply an optimization procedure aimed at two immediate objectives: increasing reactor throughput and improving film uniformity. It would be interesting to see the interplay between these two variables since non-uniformity is often attributed to pressure gradients or precursor depletion. So, an increase in precursor dose would be the natural solution. But this also causes an increase in either the pulse period or the purge necessary to remove unreacted species. This is a nice problem for ALD optimization with very practical consequences. A preliminary throughput analysis is presented in Appendix A.

7.1.3 Reactor Model

The distributed model presented in this work assumed a negligible pressure drop across the reactor and thus gases were assumed incompressible. While the pressure drop was computed to be negligibly small, it is not completely clear if this assumption maintains validity with varying precursor pulsing conditions. Considering that exposure level is critical in ALD processes, future work should consider employing the Navier-Stokes equations to more rigorously account for these variables.

7.1.4 Extension to Additional ALD Chemistries

Finally, this modeling work should be applied to additional ALD processes. Preliminary investigation of the BN ALD system has shown much similarity in the thermodynamic mechanism and initial results have appeared to be promising. At this point, the multiscale modeling approach presented in this thesis has only been applied to the alumina process in entirety. Considering that the surface reaction model is developed from first principles, it is assumed to be widely applicable. Thus, it would be a good study to assess the relative applicability of the model by extending study to additional ALD systems of interest.

A

Throughput Optimization

Reactor throughput, or effective growth rate, is directly related to the growth per cycle by

$$\phi_{eff} = \frac{gpc}{\tau_A + \tau_B + \tau_{AP} + \tau_{BP}}, \quad \text{\AA/s}$$

where ϕ_{eff} is the effective growth rate and gpc is film growth per limit cycle. A similar formula is used in [97]. The growth per cycle is known to be affected by a number of factors, namely reactor temperature, precursor partial pressure, and reactant exposure times.

Until the saturating growth per cycle is reached, an increase in exposure time for either precursor causes an observed increase in the growth per cycle. On the other hand, exposure time has an inverse relationship with respect to throughput. Purge times are modulated by the reactor volume and speed of the vacuum pump which ultimately determine the time it takes to sufficiently remove unreacted precursor gas during purge periods. Although the effective growth rate is likely to increase with a decrease in the purge time interval, doing so could cause non-ideal gas-phase

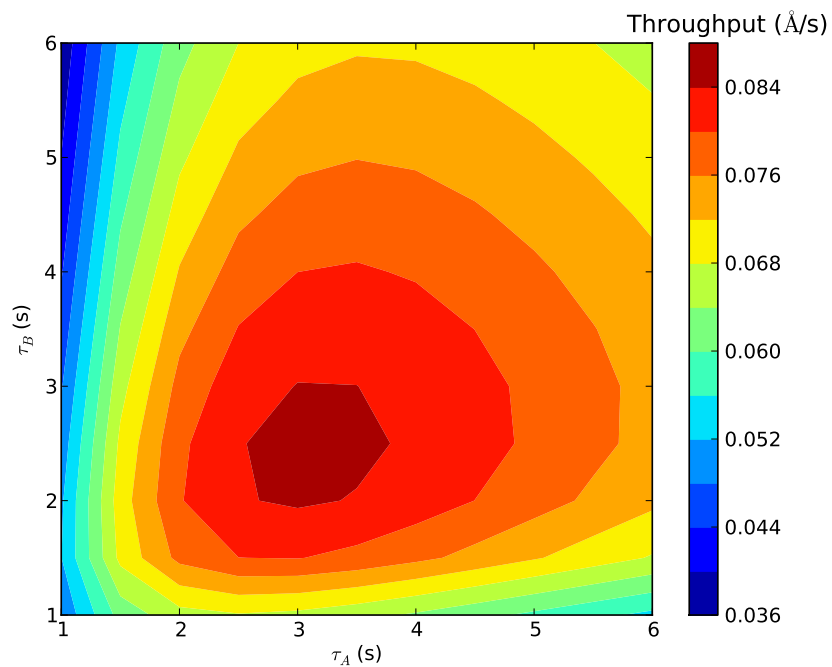


Figure A.1: Preliminary results for alumina ALD throughput as a function of precursor exposure times.

reactions. Preliminary throughput optimization results are shown in Fig A.1.

BIBLIOGRAPHY

- [1] Aarik, J. and H. Siimon, Characterization of adsorption in flow type atomic layer epitaxy reactor, *Appl. Surf. Sci.* **81**, 281–287 (1994).
- [2] Adomaitis, R. A., Development of a multiscale model for an atomic layer deposition process, *J. Cryst. Growth.* **312** 1449–1452 (2010).
- [3] Adomaitis, R. A., A ballistic transport and surface reaction model for simulating atomic layer deposition processes in high aspect-ratio nanopores, *Chem. Vap. Dep.* **17**, 353–365 (2011).
- [4] Alam, M. A. and M. L. Green, Mathematical description of atomic layer deposition and its application to the nucleation and growth of HfO₂ gate dielectric layers, *J. Appl. Phys.* **94**, 3403–3413 (2003).
- [5] *AVS 11th International Conference on Atomic Layer Deposition*, Cambridge, MA, USA, June 26–29 (2011).
- [6] *AVS 12th International Conference on Atomic Layer Deposition*, Dresden, Germany, June 17–20 (2012).
- [7] Allendorf, M.D., C. F. Melius and T. H. Osterheld, A model of the gas-phase chemistry of boron nitride CVD from BCl₃ and NH₃, *Sandia Report SAND96-8450* (1995).
- [8] Allendorf, M.D. and C. F. Melius, Thermochemistry of molecules in the B-N-Cl-H system: ab initio predictions using the BAC-MP4 method, *J. Phys. Chem. A*, **101**, 2670–2680 (1997).
- [9] ANSI/ISA-75.01.01 (IEC 60534-2-1 Mod)-2007, *Flow Equations for Sizing Control Valves*, American National Standards Institute/International Society of Automation (2007).
- [10] Anwander R., C. Palm, O. Groeger and G. Engelhardt, Formation of Lewis acidic support materials via chemisorption of trimethylaluminum on mesoporous silicate MCM-41, *Organometallics* **17**, 2027–2036 (1998).

- [11] Aricó, A. S., P. Bruce, B. Scrosati, J. Tarascon and W. van Schalkwijk, Nanostructured materials for advanced energy conversion and storage devices, *Nature Mater.* **4** 366–377 (2005).
- [12] Banerjee, P., I. Perez, L. Henn-Lecordier, S. Lee and G. Rubloff, Nanotubular metal/insulator/metal capacitor arrays for energy storage, *Nature Nanotech.* **4** 292–296 (2009).
- [13] Bartram M. E., T. A. Michalske and J. W. Rogers, A reexamination of the chemisorption of trimethylaluminum on silica, *J. Phys. Chem.* **95**, 4453–4463 (1991).
- [14] Bird, R. B., W. E. Stewart and E. N. Lightfoot, *Transport Phenomena*, 2nd ed., John Wiley & Sons, Inc.: New York (2002).
- [15] Bohr, M. T., R. S. Chan, T. Ghani and K. Mistry, The high-k Solution, *IEEE Spectrum* **44**, 29–35 (2007).
- [16] Bursh, J. F. and C. B. Schuder, The development of a universal gas sizing equation for control valves, *ISA T.* **3**, 322-328 (1964).
- [17] Cale, T. S., M. O. Bloomfield and M. K. Gobbert, Two deterministic approaches to topography evolution, *Surf. Coat. Tech.* **201**, 8873–8877 (2007).
- [18] Chen, J. and R. A. Adomaitis, An object-oriented framework for modular chemical process simulation with semiconductor processing applications, *Comput. Chem. Eng.* **30**, 1354–1380 (2006).
- [19] Chen, P., T. Mitsui, D. B. Farmer, J. Golovchenko, R. G. Gordon and D. Branton, Atomic layer deposition to fine-tune the surface properties and diameters of fabricated nanopores, *Nano Lett.* **4** 1333–1337 (2004).
- [20] Cleveland, E. R., L. Henn-Lecordier and G. W. Rubloff, Role of surface intermediates in enhanced, uniform growth rates of TiO₂ atomic layer deposition thin films using titanium tetraisopropoxide and ozone, *J Vac. Sci. Technol. A* **30** 01A150-1–01A150-6 (2012).
- [21] de Blank, R. G. J. Snijders, S. Beulens, L. Vandezande, R. Wilhelm and A. Hasper, Batch atomic layer deposition for MIM capacitors, *Electrochem. Soc. Proc.* **14** 225–230 (2003).
- [22] Delabie, A., G. Pourtois, S. Sioncke, S. Van Elshocht and K. Pierloot, Reaction mechanisms in Al₂O₃ atomic layer deposition studies by density functional theory, *Proc. ALD 2012*, Dresden, Germany, June 17–20 (2012).

- [23] Delabie, A., S. Sioncke, J. Rip, S. Van Elshocht, G. Pourtois, M. Mueller, B. Beckhoff and K. Pierloot, Reaction mechanisms for atomic layer deposition of aluminum oxide on semiconductor substrates, *J. Vac. Technol. A* **30**, 01A127-1–01A127-10 (2012).
- [24] Deminsky, M., A. Knizhnik, I. Belov, S. Umanskii, E. Rykova, A. Bagatur'yants, B. Potapkin, M. Stoker and A. Korokin, Mechanism and kinetics of thin zirconium and hafnium oxide film growth in an ALD reactor, *Surf. Sci.* **549**, 67–86 (2004).
- [25] Dendoven, J., D. Deduytsche, J. Musschoot, R. L. Vanmeirhaeghe and C. Detavernier, Modeling the conformality of atomic layer deposition: The effect of sticking probability, *J. Electrochem. Soc.* **156**, P63–P67 (2009).
- [26] Dillon, A. C., A. W. Ott, J. D. Way and S. M. George, Surface chemistry of Al₂O₃ deposition using Al(CH₃)₃ and H₂O in a binary reaction sequence, *Surf. Sci.* **322** 230–242 (1995).
- [27] Dkhissi, A., A. Estève, C. Mastail, S. Olivier, G. Mazaleyrat, L. Jeloica and M. D. Rouhani, Multiscale modeling of the atomic layer deposition of HfO₂ thin film grown on silicon: How to deal with a kinetic Monte Carlo procedure, *J. Chem. Theory Comput.* **4**, 1915–1927 (2008).
- [28] Dkhissi, A., G. Mazaleyrat, L. Jeloica and M. D. Rouhani, Nucleation and growth of atomic layer deposition of HfO₂ gate dielectric layers on silicon oxide: A multiscale modelling investigation, *Phys. Chem. Chem. Phys.* **11**, 3701–3709 (2009).
- [29] Dwivedi, V. and R. A. Adomaitis, Multiscale simulation and optimization of an atomic layer deposition process in a nanoporous material, *ECS Transactions* **25** 115-122 (2009).
- [30] Dwivedi, V., R. A. Adomaitis, R.A. and C. D. Travis, Passively controlled thermal material deposited by atomic layer deposition, in *Proc. Paper 755c, AIChE Annual Meeting*, Pittsburgh, PA, USA, October 28 – November 2 (2012).
- [31] Elam, J. W., M. D. Groner and S. M. George, Viscous flow reactor with quartz crystal microbalance for thin film growth by atomic layer deposition, *Rev. Sci. Instrum.* **73**, 2981–2987 (2002).
- [32] Elam, J. W., D. Routkevitch, P. P. Mardilovich and S. M. George, Conformal coating on ultrahigh-aspect-ratio nanopores of anodic alumina by atomic layer deposition, *Chem. Mater.* **15**, 3507–3517 (2003).

- [33] Elam, J. W., G. Xiong, C. Y. Han, H. H. Wang, J. P. Birrell, U. Welp, J. N. Hryn, M. J. Pellin, T. F. Baumann, J. F. Poco and J. H. Satcher Jr., Atomic layer deposition for the conformal coating of nanoporous materials, *J. Nanomater.* Article ID 263852 (2006).
- [34] Elam, J. W., J. A. Libera, M. J. Pellin and P. C. Stair, Spatially controlled atomic layer deposition in porous materials, *Appl. Phys. Lett.* **91** 243105–243105-3 (2007).
- [35] Elliott, S. D., Predictive process design: a theoretical model of atomic layer deposition, *Comp. Mater. Sci.* **33**, 20–25 (2005).
- [36] Elliott, S. D., in *Rare Earth Oxide Thin Films*, Eds. M. Fanciulli, G. Scarel, *Top. Appl. Phys.* **106**, 73–86 (2007).
- [37] Elliott, S. D., Atomic-scale simulation of ALD chemistry, *Semicond. Sci. Tech.* **27**, 1–10 (2012).
- [38] Elliott, S. D., in *Atomic Layer Deposition for Semiconductors* Ed. C. S. Hwang, Springer: New York, 47–69 (2014).
- [39] Elliott, S. D. and H. P. Pinto, Modelling the deposition of high-k dielectric films by first principles, *J. Electroceram.* **13**, 117–120 (2004).
- [40] Elliott, S. D. and J. C. Greer, Simulating the atomic layer deposition of alumina from first principles, *J. Mater. Chem.* **14**, 3246–3250 (2004).
- [41] Eyring, H., The activated complex and the absolute rate of chemical reactions, *Chem. Rev.* **17**, 65–77 (1935).
- [42] Ferguson, J. D., A. W. Weimer and S. M. George, Atomic layer deposition of boron nitride using sequential exposures of BCl_3 and NH_3 , *Thin Solid Films* **413**, 16–25 (2002).
- [43] Frank M. M., Y. J. Chabal and G. D. Wilk, Nucleation and interface formation mechanisms in atomic layer deposition of gate oxides, *Appl. Phys. Lett.* **82**, 4758–4760 (2003).
- [44] George, S. M., Atomic layer deposition: An overview, *Chem. Rev.* **110**, 111–131 (2010).
- [45] Glasstone, S. K., J. Laidler and H. Eyring, *The Theory of Rate Processes*, 1st ed., McGraw-Hill Book Company: New York (1941).

- [46] Gobbert, M. K., S. G. Webster and T. S. Cale, Transient adsorption and desorption in micrometer scale features, *J. Electrochem. Soc.* **149**, G461–G473 (2002).
- [47] Gobbert, M. K., V. Prasad and T. S. Cale, Modeling and simulation of atomic layer deposition at the feature scale, *Thin Solid Films* **410**, 129–141 (2002).
- [48] Gobbert, M. K., V. Prasad and T. S. Cale, Predictive modeling of atomic layer deposition on the feature scale, *J. Vac. Sci. Technol. B* **20**, 1031–1043 (2002).
- [49] Google Scholar search. Key words used in title: “atomic layer deposition” “atomic layer epitaxy,” Retrieved July 2 (2013).
- [50] Gordon, R. G., in *Atomic Layer Deposition for Semiconductors*, Ed. C. S. Hwang, Springer: New York (2014).
- [51] Gordon, R. G., D. Hausmann, E. Kim and J. Shepard, A kinetic model for step coverage by ALD in narrow holes or trenches, *Chem. Vap. Dep.* **9**, 73–78 (2003).
- [52] Granneman, E., P. Fischer, D. Pierreux, H. Terhorst and P. Zagwijn, Batch ALD: Characteristics, comparison with single wafer ALD, and examples, *Surf. Coat. Tech.* **201**, 8899–8907 (2007).
- [53] Gutierrez, G. and B. Johansson, Molecular dynamics study of structural properties of amorphous Al_2O_3 , *Phys. Rev. B* **65**, 104202-1–104202-9 (2002).
- [54] Halls, M. D., K. Raghavachari, M. M. Frank and Y. J. Chabal, Atomic layer deposition of Al_2O_3 on H-passivated Si: $\text{Al}(\text{CH}_3)_2\text{OH}$ surface reactions with H/Si(100)-2x1, *Phys. Rev. B* **68**, 161302-1–161302-4 (2003).
- [55] Halls, M. D. and K. Raghavachari, Atomic layer deposition growth reactions of Al_2O_3 on Si(100)-2x1, *J. Phys. Chem. B* **108**, 4058–4062 (2004).
- [56] Halls, M. D. and K. Raghavachari, Atomic layer deposition of Al_2O_3 on H-passivated Si. I. Initial surface reaction pathways with H/Si(100)-2x1, *J. Chem. Phys.* **118**, 10221–10226 (2003).
- [57] Halls, M. D. and K. Raghavachari, Importance of steric effects in cluster models of silicon surface chemistry: ONIOM studies of the atomic layer deposition (ALD) of Al_2O_3 on H/Si(111), *J. Phys. Chem. A* **108**, 2982–2987 (2004).

- [58] Hangos, K. and I. Cameron, *Process Modeling and Model Analysis: Vol. 4. Process Systems Engineering*, Eds. G. Stephanopoulos, J. Perkins, Academic Press: London (2001).
- [59] Han, J. H., G. Gao, Y. Widjaja, E. Garfunkel and C. B. Musgrave, A quantum chemical study of ZrO₂ atomic layer deposition growth reactions on the SiO₂ surface, *Surf. Sci.* **550**, 199–212 (2004).
- [60] Hass, K. C., W. F. Schneider, A. Curioni and W. Andreoni, The chemistry of water on alumina surfaces: Reaction dynamics from first principles, *Science* **282**, 265–268 (1998).
- [61] Hass, K. C., W. F. Schneider, A. Curioni and W. Andreoni, First-principles molecular dynamics simulations of H₂O on α -Al₂O₃ (0001), *J. Phys. Chem. B* **104**, 5527–5540 (2000).
- [62] Haukka, S., ALD technology - present and future challenges progress in ALD equipment and processing, *ECS Trans.* **4**, 15–26 (2007).
- [63] Hausmann, D. M., E. Kim, J. Becker and R.G. Gordon, Atomic layer deposition of hafnium and zirconium oxides Using metal amide precursors, *Chem. Mater.* **14**, 4350–4358 (2002).
- [64] Henn-Lecordier, L., M. Anderle, E. Robertson and G. W. Rubloff, Impact of parasitic reactions on wafer-scale uniformity in water-based and ozone-based atomic layer deposition, *J. Vac. Sci. Technol. A* **29** 051509-1–051509-8. (2011).
- [65] Heyman, A. and C. B. Musgrave, A quantum chemical study of the atomic layer deposition of Al₂O₃ using AlCl₃ and H₂O as precursors, *J. Phys. Chem. B* **108**, 5718–5725 (2004).
- [66] Hill, T. L., *An Introduction to Statistical Thermodynamics*, Dover Publications, Inc., New York (1986).
- [67] Hirschfelder, J. O., C. F. Curtiss and R. B. Bird, *Molecular Theory of Gases and Liquids*, 2nd ed., John Wiley & Sons, Inc.: New York, (1964).
- [68] Holmqvist, A., F. Magnusson and S. Stenström, Scale-up analysis of continuous cross-flow atomic layer deposition reactor designs with temporal precursor pulsing, submitted *Comput. Chem. Eng.* (2013).
- [69] Holmqvist, A., T. Törndahl and S. Stenström, A model-based methodology for the analysis and design of atomic layer deposition processes—Part I: Mechanistic modelling of continuous flow reactors, *Chem. Eng. Sci.* **81**, 260–272 (2012).

- [70] Holmqvist, A., T. Törndahl and S. Stenström, A model-based methodology for the analysis and design of atomic layer deposition processes—Part II: Experimental validation and mechanistic analysis, *Chem. Eng. Sci.* **94**, 316–329 (2013).
- [71] Holmqvist, A., T. Törndahl and S. Stenström, A model-based methodology for the analysis and design of atomic layer deposition processes—Part III: Constrained multi-objective optimization, *Chem. Eng. Sci.* **96**, 71–86 (2013).
- [72] Holmqvist, A., T. Törndahl, U. Zimmermann, F. Magnusson and S. Stenström, Dynamic parameter optimization of atomic layer deposition kinetics applied to in situ quartz crystal microbalance diagnostics, submitted *Chem. Eng. Sci.* (2013).
- [73] Hwang, C. S. and C. Y. Yoo, in *Atomic Layer Deposition for Semiconductors* Ed. C. S. Hwang, Springer: New York, 3–12 (2014).
- [74] Jeloica, L., A. Estéve, M. D. Rouhani and D. Estéve, Density functional theory study of HfCl_4 , ZrCl_4 , and $\text{Al}(\text{CH}_3)_3$ decomposition on hydroxylated SiO_2 : Initial stage of high-k atomic layer deposition. *Appl. Phys. Lett.* **83**, 542–544 (2003).
- [75] Juppo, M., A. Rahtu, M. Ritala and M. Leskelä, *In situ* mass spectrometry study on surface reactions in atomic layer deposition of Al_2O_3 thin films from trimethylaluminum and water, *Langmuir* **16**, 4034–4039 (2000).
- [76] Kestin, J., S. T. Ro and W. A. Wakeham, Viscosity of noble gases in the temperature range 25–700°C, *J. Chem. Phys.*, **56**, 4119–4124 (1972).
- [77] Kuhn, K. J., Moore’s law past 32nm: Future challenges in device scaling, in *Proc. Computational Electronics, 2009. IWCE '09.*, Beijing, China, May 27–29 (2009).
- [78] Kim, H., Atomic layer deposition of metal and nitride thin films: Current research efforts and applications for semiconductor device processing, *J. Vac. Sci. Technol. B* **21**, 2231–2261 (2003).
- [79] Kim, D.-H., D.-H. Kim, Y.-C. Jeong, H.-I. Seo and Y.-C. Kim, Reaction of tri-methylaluminum on Si (001) surface for initial aluminum oxide thin-film growth, *Bull. Kor. Chem. Soc.* **31**, 3579–3582 (2010).
- [80] Kim, D.-H., S.-B. Baek, H.-I. Seo and Y.-C. Kim, Interactions between tri-methylaluminum molecules and their effect on the reaction of tri-

- methylaluminum with an OH-terminated Si (001) surface, *Appl. Surf. Sci.* **257**, 6326–6331 (2011).
- [81] Kim, H., H. Lee and W. J. Maeng, Applications of atomic layer deposition to nanofabrication and emerging nanodevices, *Thin Solid Films* **517**, 2563–2580 (2009).
- [82] Kimes, W. A. and J. E. Maslar, *In situ* water measurements as a diagnostic of flow dynamics in ALD reactors, in *Proc. ALD 2011*, Cambridge, MA, USA, June 26–29 (2011).
- [83] Klejna, S. and S. D. Elliott, First-principles modeling of the “clean-Up” of native oxides during atomic layer deposition onto III-V substrates, *J. Phys. Chem. C* **116**, 643–654 (2012).
- [84] Knoops, H. C. M., E. Langereis, M. C. M. van de Sanden and W. M. M. Kessels, Conformality of plasma-assisted ALD: physical processes and modeling, *J. Electrochem. Soc.* **157**, G241–G249 (2010).
- [85] Knoops, H. C. M., J. W. Elam, J. A. Libera and W. M. M. Kessels, Surface loss in ozone-based atomic layer deposition processes, *Chem. Mater.* **23**, 2381–2387 (2011).
- [86] Lankhorst, A. M., B.D. Paarhuis, H. J. C. M. Terhorst, P. J. P. M. Simons and C. R. Kleijn, Transient ALD simulations for a multi-wafer reactor with trenched wafers, *Surf. Coat. Tech.* **201**, 8842–8848 (2007).
- [87] Laidler, K.J., *Chemical Kinetics*, 3rd ed., Harper and Row: New York (1978).
- [88] Laidler, K. J., S. Glasstone and H. Eyring, Application of the theory of absolute reaction rates to heterogeneous processes: I. The adsorption and desorption of gases, *J. Chem. Phys.* **8**, 659–667 (1940).
- [89] Laidler, K. J., S. Glasstone and H. Eyring, Application of the theory of absolute reaction rates to heterogeneous processes: II. Chemical reactions on surfaces, *J. Chem. Phys.* **8**, 667–676 (1940).
- [90] Lakomaa, E.-L., A. Root and T. Suntola, Surface reactions in Al₂O₃ growth from trimethylaluminium and water by atomic layer epitaxy, *Appl. Surf. Sci.* **107**, 107–115 (1996).
- [91] Lamagna, L., C. Wiemer, M. Perego, S. Spiga, J. Rodríguez, D. S. Coll, M. E. Grillo, S. Klejna and S. D. Elliott, Mechanisms for substrate-enhanced growth

- during the early stages of atomic layer deposition of alumina onto silicon nitride surfaces, *Chem. Mater.* **24**, 1080–1090 (2012).
- [92] Laubengayer, A.W. and W. F. Gilliam, The alkyls of the third group elements. I. Vapor phase studies of the alkyls of aluminum, gallium and indium, *J. Am. Chem. Soc.* **63**, 477–479 (1941).
- [93] Lee, H., C. J. An, S. J. Piao, D. Y. Ahn, M. Kim and Y. Min, Shrinking core model for Knudsen diffusion-limited atomic layer deposition on a nanoporous monolith with an ultrahigh aspect ratio, *J. Phys. Chem. C* **114** 18601–18606 (2010).
- [94] Leskelä, M. and M. Ritala, Atomic layer deposition (ALD): from precursors to thin film structures, *Thin Solid Films* **409**, 138–146 (2002).
- [95] Lewis, B. and J. C. Anderson, *Nucleation and Growth of Thin Films*, Academic Press: New York (1978).
- [96] Lim, J., H. Park and S. Wang, Analysis of a transient region during the initial stage of atomic layer deposition, *J. Appl. Phys.* **88**, 6327–6331 (2000).
- [97] Lim, J., H. Park and S. Wang, Kinetic modeling of film growth rate in atomic layer deposition, *J. Electrochem. Soc.* **148**, C403–C408 (2001).
- [98] Lim, J., J. Park and S. Wang, Kinetic modeling of film growth rates of TiN films in atomic layer deposition, *J. Appl. Phys.* **87**, 4632–4634 (2000).
- [99] Lu, H.-L., W. Chen, S.-J. Ding, M. Xu, D. W. Zhang and L.-K. Wang, Initial surface reactions in atomic layer deposition of Al₂O₃ on the hydroxylated GaAs(001)-4 x 2 surface, *J. Phys.-Condens. Mat.* **17**, 7517–7522 (2005).
- [100] Mäkinen V., K. Honkala and H. Häkkinen, Atomic layer deposition of aluminum oxide on TiO₂ and its impact on N₃ dye adsorption from first principles, *J. Phys. Chem. C* **115**, 9250–9259 (2011).
- [101] Marichy, C., M. Bechelany and N. Pinna, Atomic layer deposition of nanostructured materials for energy and environmental applications, *Adv. Mater.* **24**, 1017–1032 (2012).
- [102] Matero, R., A. Rahtu, M. Ritala, M. Leskelä and T. Sajavaara, Effect of water dose on the atomic layer deposition rate of oxide thin films, *Thin Solid Films* **368**, 1–7 (2000).

- [103] Matthäus, C. and R. A. Wheeler, Fragment mode analysis and its application to the vibrational normal modes of boron trichloride-ammonia and boron trichloride-pyridine complexes, *Spectrochimica Acta Part A* **57**, 521–534 (2001).
- [104] Mazaleyrat, G., A. Esteve, L. Jeloica and M. Djafari-Rouhani, A methodology for the kinetic Monte Carlo simulation of alumina atomic layer deposition onto silicon, *Comp. Mat. Sci.* **33**, 74–82 (2005).
- [105] McDaniel, A. H. and M. D. Allendorf, Flow-tube investigation of the high-temperature reaction between BCl_3 and NH_3 , *J. Phys. Chem. A* **102**, 7804–7812 (1998).
- [106] Meng, X., X. Yang and X. Sun, Emerging applications of atomic layer deposition for lithium-ion battery studies, *Adv. Mater.* **24**, 3589–3615 (2013).
- [107] Mukhopadhyay, A. B. and C. B. Musgrave, Non-growth ligand exchange reactions in atomic layer deposition of HfO_2 *Chem. Phys. Lett.* **421**, 215–220 (2006).
- [108] Mukhopadhyay, A. B., C. B. Musgrave and, F. F. Sanz, Atomic layer deposition of hafnium oxide from hafnium chloride and water *J. Am. Chem. Soc.* **130**, 11996–12006 (2008).
- [109] Mui, C. and C. B. Musgrave, Atomic layer deposition of HfO_2 using alkoxides as precursors, *J. Phys. Chem. B* **108**, 15150–15164 (2004).
- [110] Neufeld, P. D., A. R. Janzen and R. A. Aziz, Empirical equations to calculate 16 of the transport collision integrals $\Omega^{(l,s)*}$ for the Lennard-Jones (126) potential, *J. Chem. Phys.*, **57**, 1100–1102 (1972).
- [111] Nguyen, H. M. T., H.-Y. Tang, W.-F. Huang and M. C. Lin, Mechanisms for reactions of trimethylaluminum with molecular oxygen and water, *Comp. Theor. Chem.* **1035**, 39–43 (2014).
- [112] Nilsen, O., C. E. Mohn, A. Kjekshus and H. Fjellvåg, Analytical model for island growth in atomic layer deposition using geometrical principles, *J. Appl. Phys.* **102**, 024906-1–024906-13 (2007).
- [113] Nyns, L., A. Delabie, G. Pourtois, S. Van Elshocht, C. Vinckier and S. De Gendt, Study of the surface reactions in ALD hafnium aluminates, *J. Electrochem. Soc.* **157**, G7–G12 (2010).
- [114] Linstrom, P. J. and E.W. G. Mallard, Eds. NIST Chemistry WebBook, NIST Standard Reference Database Number 69, National Institute of Standards

and Technology, Gaithersburg MD, USA, <http://webbook.nist.gov>, Retrieved February 7 (2013).

- [115] Okuyama, Y., C. Barelli, C. Tousseau, S. Park and Y. Senzaki, Batch process for atomic layer deposition of hafnium silicate thin films on 300-mm-diameter silicon substrates, *J. Vac. Sci. Technol. A* **23**, L1–L3 (2005).
- [116] Olivier, S., J.-M. Duc  r  , C. Mastail, G. Landa, A. Est  ve and M. D. Rouhani, Insights into crystalline preorganization of gas-phase Precursors: Densification mechanisms, *Chem. Mater.* **20**, 1555–1560 (2008).
- [117] Ott, A. W., K. C. McCarthy, J. W. Klaus, J. D. Way and S. M. George, Atomic layered controlled deposition of Al₂O₃ films using a binary reaction sequence chemistry, *Appl. Surf. Sci.* **107**, 128–136 (1996).
- [118] Ott, A. W., J. W. Klaus, J. M. Johnson and S. M. George, Al₂O₃ thin film growth on Si(100) using binary reaction sequence chemistry, *Thin Solid Films* **292**, 135–144 (1997).
- [119] P  iv  saari, J. Niinist  , P. Myllym  ki, C. Dezelah IV, C. H. Winter, M. Putkonen, M. Nieminen and L. Niinist  , in *Rare Earth Oxide Thin Films*, Eds. M. Fanciulli, G. Scarel, *Top. Appl. Phys.* **106**, 15–32 (2007).
- [120] Paranjpe A., S. Gopinati, T. Omstead and R. Bubber, Atomic layer deposition of AlO_x for thin film head gap applications, *J. Electrochem. Soc.* **148**, G465–G471 (2001).
- [121] Park, H.-S., J.-S. Min, J.-W. Lim and S.-W. Kang, Theoretical evaluation of film growth rate during atomic layer epitaxy, *Appl. Surf. Sci.* **158**, 81–91 (2000).
- [122] Patibandla, N. and K. L. Luthra, Chemical Vapor Deposition of Boron Nitride, *J. Electrochem. Soc.* **139**, 3558–3565 (1992).
- [123] Pellin, M. J., P. C. Stair, G. Xionga, J. W. Elam, J. Birrell, L. Curtiss, S. M. George, C. Y. Han, L. Iton, H. Kung, M. Kung and H. H. Wang, Mesoporous catalytic membranes: Synthetic control of pore size and wall composition, *Catal. Lett.* **102**, 127–130 (2005).
- [124] Poling, B. E., J. M. Prausnitz and J. P. O’Connell, *The Properties of Gases and Liquids*, 5th ed., McGraw-Hill: New York (2001).
- [125] Prechtel, G., A. Kersch, G. Schulze Icking-Konert, W. Jacobs, T. Hecht, H. Boubekeur and U. Schroder, A model for Al₂O₃ ALD conformity and deposi-

- tion rate from oxygen precursor reactivity, *Proc. Int. Electron Devices Meeting*, Washington, DC, USA, December 8–10 (2003).
- [126] Private email communication between R. A. Adomaitis and W. T. Tysoe, February 10 (2012).
- [127] Puurunen R. L., Preparation by atomic layer deposition and characterisation of catalyst supports surfaced with aluminium nitride, Doctoral dissertation, Industrial chemistry publication series / Helsinki University of Technology, <http://urn.fi/urn:nbn:fi:tkk-001952> (2002)
- [128] Puurunen, R. L., Growth per cycle in atomic layer deposition: A theoretical model, *Chem. Vap. Dep.* **9**, 249–257 (2003).
- [129] Puurunen, R. L., Growth per cycle in atomic layer deposition: Real application examples of a theoretical model, *Chem. Vap. Dep.* **9**, 327–332 (2003).
- [130] Puurunen, R. L., Correlation between the growth-per-cycle and the surface hydroxyl group concentration in the atomic layer deposition of alumina oxide from trimethylaluminum and water, *Appl. Surf. Sci.* **245** 6–10 (2005).
- [131] Puurunen, R. L., Surface chemistry of atomic later deposition: A case study of the trimethylaluminum/water system, *Appl. Phys. Rev.* **97**, 121301-1–121301-52 (2005).
- [132] Puurunen R. L., A. Root, P. Sarv, M. M. Viitanen, H. H. Brongersma, M. Lindblad and A. O. I. Krause, Growth of aluminum nitride on porous alumina and silica through separate saturated gas-solid reactions of trimethylaluminum and ammonia, *Chem. Mater.* **14**, 720–729 (2002).
- [133] Puurunen R. L., A. Root, P. Sarv, S. Haukka, E. I. Iiskola, M. Lindblad and A. O. I. Krause, Growth of aluminium nitride on porous silica by atomic layer chemical vapour deposition, *Appl. Surf. Sci.* **165**, 193–202 (2000).
- [134] Puurunen R. L., A. Root, S. Haukka, E. I. Iiskola, M. Lindblad and A. O. I. Krause, IR and NMR study of the chemisorption of ammonia on trimethylaluminum-modified silica, *J. Phys. Chem. B* **104**, 6599–6609 (2000).
- [135] Puurunen R. L., M. Lindblad, A. Root and A. O. I. Krause, Successive reactions of gaseous trimethylaluminium and ammonia on porous alumina, *Phys. Chem. Chem. Phys.* **3**, 1093–1102 (2001).
- [136] Puurunen, R.L., W. Vandervorst, W. F. A. Besling, O. Richard, H. Bender, T. Conard, C. Zhao, A. Delabie, M. Caymax and S. de Gendt, *et al.*, Island

- growth in the atomic layer deposition of zirconium oxide and aluminum oxide on hydrogen-terminated silicon: Growth mode modeling and transmission electron microscopy, *J. Appl. Phys.* **96**, 4878–4889 (2004).
- [137] Puurunen, R.L. and W. Vandervorst, Island growth as a growth mode in atomic layer deposition: A phenomenological model, *J. Appl. Phys.* **96**, 7686–7695 (2004).
- [138] Rahtu, A., T. Alaranta and M. Ritala, *In situ* quartz crystal microbalance and quadrupole mass spectrometry studies of atomic layer deposition of aluminum oxide from trimethylaluminum and water, *Langmuir* **17**, 6506–6509 (2001).
- [139] Ren, J., G. Zhou, Y. Hua, H. Jiang, D. W. Zhang, Surface reactions in atomic layer deposition of HfO₂, ZrO₂ and Al₂O₃ on hydroxylated and sulfur-passivated GaAs(1 0 0) surfaces: A comparative study by density functional theory, *Appl. Surf. Sci.* **254**, 7115–7121 (2008).
- [140] Ritala, M. and J. Niinistö, in *Chemical Vapour Deposition: Precursors, Processes and Applications*, Eds. A. C. Jones, M. L. Hitchman, Royal Society of Chemistry, 158–206 (2009).
- [141] Ritala, M. and M. Leskelä, in *Handbook of Thin Film Materials*, Ed. H. S. Nalwa, Academic Press: New York, 103–159 (2002).
- [142] Rose, M. and J. W. Bartha, Method to determine the sticking coefficient of precursor molecules in atomic layer deposition, *Appl. Surf. Sci.* **255**, 6620–6623 (2009).
- [143] Sandler, S. I., *An Introduction to Applied Statistical Thermodynamics*, John Wiley & Sons, Inc.: New York (2011).
- [144] *Savannah 100 Atomic Layer Deposition System, Customer Product Manual* Cambridge NanoTech, Inc. (2004).
- [145] Schumacher, M., P. K. Baumann and T. Seidel, AVD and ALD as two complementary technology solutions for next generation dielectric and conductive thin-film processing, *Chem. Vap. Dep.* **12**, 99-108 (2006).
- [146] Shankar, S., H. Simka and M. Haverty, Density functional theory and beyond opportunities for quantum methods in materials modeling semiconductor technology, *J. Phys. Condens. Matter* **20**, 1–9 (2008).
- [147] Siimon, H. and J. Aarik, Modelling of precursor flow and deposition in atomic layer deposition reactor, *J. Phys. IV* **5**, C5:245–C5:252 (1995).

- [148] Siimon, H. and J. Aarik, Thickness profiles of thin films caused by secondary reactions in flow-type atomic layer deposition reactors, *J. Phys. D* **30**, 1725–1728 (1997).
- [149] Skoog, S. A., J. W. Elam and R. J. Narayan, Atomic layer deposition: Medical and biological applications, *Int. Mater. Rev.* **58**, 113–129 (2013).
- [150] Soto, C. and W. T. Tysoe, The reaction pathway for the growth of alumina on high-surface area alumina and in ultrahigh vacuum by a reaction between trimethylaluminum and water, *J. Vac. Sci. Technol. A* **9**, 2686–2695 (1991).
- [151] Suntola, T. and J. Anston, U. S. Patent No. 4,058,430 November 15 (1977).
- [152] Suntola, T., Atomic layer epitaxy, *Mater. Sci. Rep.* **4**, 262–312 (1989).
- [153] Swagelok, *Valve Sizing Technical Bulletin MS-06-84-E*, Swagelok Company (2007).
- [154] Swagelok, *Diaphragm Valves for Atomic Layer Deposition MS-02-301*, Swagelok Company (2008).
- [155] Terranova, U. and D. R. Bowler, Effect of hydration of the TiO₂ anatase (101) substrate on the atomic layer deposition of alumina films, *J. Mater. Chem.* **21**, 4197–4203 (2011).
- [156] Travis, C. D. and R. A. Adomaitis, Modeling ALD surface reaction and process dynamics using absolute reaction rate theory, *Chem. Vapor Depos.* **19**, 4–14 (2013).
- [157] Travis, C. D. and R. A. Adomaitis, Dynamic modeling for the design and cyclic operation of an atomic layer deposition (ALD) reactor, *Processes* **1**, 128–152 (2013).
- [158] Travis, C. D. and R. A. Adomaitis, Modeling alumina atomic layer deposition reaction kinetics during the trimethylaluminum exposure, **Theor. Chem. Acc.** *133*, 1414 (2014).
- [159] Travis, C. D. and R. A. Adomaitis, Model-based analysis of atomic layer deposition growth kinetics and multiscale process dynamics, *in preparation*, (2014).

- [160] Van Delft, J. A., D. Garcia-Alonso and W. M. M. Kessels, Atomic layer deposition for photovoltaics: Applications and prospects for solar cell manufacturing, *Semicond. Sci. Tech.* **27**, 074002 (2012).
- [161] Uusitalo A., T. T. Pakkanen, M. Kröger-Laukkanen, L. Niinistö, K. Hakala, S. Paavola and B. Löfgren, Heterogenization of racemic ethylenebis(1-indenyl)zirconium dichloride on trimethylaluminum vapor modified silica surface, *J. Mol. Catal. A-Chem.* **160**, 343–356 (2000).
- [162] Widjaja, Y. and C. B. Musgrave, Quantum chemical study of the mechanism of aluminum oxide atomic layer deposition. *Appl. Phys. Lett.* **80**, 3304–3306 (2002).
- [163] Widjaja, Y. and C. B. Musgrave, Quantum chemical study of the elementary reactions in zirconium oxide atomic layer deposition, *Appl. Phys. Lett.* **81**, 304–306 (2002).
- [164] Widjaja, Y. and C. B. Musgrave, Atomic layer deposition of hafnium oxide: A detailed reaction mechanism from first principles, *J. Chem. Phys.* **117**, 1931–1934 (2002).
- [165] Widjaja, Y., J. H. Han and C. B. Musgrave, Quantum chemical study of zirconium oxide deposition on the Si(100)-(21) surface, *J. Phys. Chem. B* **107**, 9319–9324 (2003).
- [166] Wind, R.A. and S. M. George, Quartz crystal microbalance studies of Al₂O₃ atomic layer deposition using trimethylaluminum and water at 125°C, *J. Phys. Chem. A* **114**, 1281–1289 (2010).
- [167] Xu, Y. and C. B. Musgrave, A DFT study of the Al₂O₃ atomic layer deposition on SAMS: effect of SAM termination, *Chem. Mater.* **16**, 646–653 (2004).
- [168] Xu, K. and P D. Ye , Theoretical study of atomic layer deposition reaction mechanism and kinetics for aluminum oxide formation at graphene nanoribbon open edges, *J. Phys. Chem. C* **114** 10505–10511 (2010).
- [169] Yanguas-Gil, A. and J. W. Elam, Diffusion-reaction model of ALD in nanostructured substrates: Analytic approximations to dose times as a function of the surface reaction probability, *ECS Transactions* **41**, 169–174 (2011).
- [170] Yanguas-Gil, A. and J. W. Elam, Simple model for atomic layer deposition precursor reaction and transport in a viscous-flow tubular reactor, *J. Vac. Sci. Technol. A* **30**, 01A159-1–01A159-7 (2012).

- [171] Ylilammi, M., Mass transport in atomic layer deposition carrier gas reactors, *J. Electrochem. Soc.* **142**, 2474–2479 (1995).
- [172] Yim, S., D. Lee, K. Kim, S. Kim, T. Yoon and K. Kim, Nucleation kinetics of Ru on silicon oxide and silicon nitride surfaces deposited by atomic layer deposition, *J. Appl. Phys.* **103**, 113509-1–113509-9 (2008).
- [173] Yu, S., S. Qing-Qing, D. Lin, L. Han, D. Shi-Jin and Z. Wei, Atomic layer deposition of Al₂O₃ on H-passivated GeSi: Initial surface reaction pathways with H/GeSi(100)-2x1, *Chin. Phys. Lett.* **26** 053101-1–053101-3 (2009).
- [174] Yun, S. J., K.-H. Lee, J. Skarp, H.-R. Kim and K.-S. Nam, Dependence of atomic layer-deposited Al₂O₃ films characteristics on growth temperature and Al precursors of Al(CH₃)₃ and AlCl₃, *J. Vac. Sci. Technol. A* **15**, 2993–2997 (1997).

PUBLICATIONS & PRESENTATIONS

Refereed Journal Publications

Travis, C. D. and R. A. Adomaitis, Modeling alumina atomic layer deposition reaction kinetics during the trimethylaluminum exposure, *Theor. Chem. Acc.* **133**, 1414 (2014).

Travis, C. D. and R. A. Adomaitis, Dynamic modeling for the design and cyclic operation of an atomic layer deposition (ALD) reactor, *Processes* **1**, 128–152 (2013).

Travis, C. D. and R. A. Adomaitis, Modeling ALD surface reaction and process dynamics using absolute reaction rate theory, *Chem. Vap. Dep.* **19**, 4–14 (2013).

Publications to be Submitted

Travis, C. D. and R. A. Adomaitis, Model-based analysis of atomic layer deposition growth kinetics and multiscale process dynamics, (tentative submission May 2014).

Conference Presentations

Adomaitis*, R. A. and C. D. Travis, Current modeling and simulation challenges in thin-film deposition processes, Paper 105b, *AIChE Annual Meeting*, San Francisco, CA, November 3–8, (2013).

Travis*, C. D. and R. A. Adomaitis, First principles modeling of atomic layer deposition surface reaction and process dynamics using absolute reaction rate theory. Paper 362d, *AIChE Annual Meeting*, Pittsburgh, PA, October 28 – November 2, (2012).

Travis*, C. D. and R. A. Adomaitis, The computational challenges of simulating atomic layer deposition process dynamics, Paper 595a, *AIChE Annual Meeting*, Pittsburgh, PA, October 28 – November 2, (2012).

Dwivedi, V., R. A. Adomaitis* and C. D. Travis, Passively controlled thermal material deposited by atomic layer deposition, Paper 755c, *AIChE Annual Meeting*, Pittsburgh, PA, October 28 – November 2, (2012).

Travis*, C. D. and R. A. Adomaitis, Modeling ALD surface reaction and process dynamics using absolute reaction rate theory, *UMD Graduate Research Interaction Day (GRID)*, College Park, MD, April 11, (2012).

Travis*, C. D. and R. A. Adomaitis, Modeling ALD surface reaction and process dynamics using absolute reaction rate theory, *UMD Research Fest*, College Park, MD, March 30, (2012).

Travis, C. D. and R. A. Adomaitis*, Coupling ballistic transport and surface reaction models for simulation of atomic layer deposition processes, Paper 317b, *AIChE Annual Meeting*, Minneapolis, MN, October 16–21, (2011).

Travis*, C. D. and R. A. Adomaitis, Surface reaction modeling for atomic layer deposition processes, *UMD Research Fest*, College Park, MD, March 8, (2011).

*Presenter